

# ATOMISTIC AND MACHINE LEARNING SIMULATIONS FOR NANOSCALE THERMAL TRANSPORT

by

Prabudhya Roy Chowdhury

A Dissertation

*Submitted to the Faculty of Purdue University*

*In Partial Fulfillment of the Requirements for the degree of*

Doctor of Philosophy



School of Mechanical Engineering

West Lafayette, Indiana

August 2021

**THE PURDUE UNIVERSITY GRADUATE SCHOOL  
STATEMENT OF COMMITTEE APPROVAL**

**Dr. Xiulin Ruan, Chair**

School of Mechanical Engineering

**Dr. Xianfan Xu**

School of Mechanical Engineering

**Dr. Amy Marconnet**

School of Mechanical Engineering

**Dr. Mark Lundstrom**

School of Electrical and Computer Engineering

**Approved by:**

Dr. Nicole Key

## ACKNOWLEDGMENTS

As I sit down (at last) to write this section of my dissertation, I wonder if it would be better served to write a separate chapter, or even a book, altogether, to acknowledge the people who have guided and helped me during my Ph.D. journey. For when I first started my Ph.D. program in a new country, far away from the familiar faces and places I have known for 23 years, I was much like my thesis was at that same moment in time - full of blank pages ready to be painted with new words and pictures. Sure enough, as I have managed over the last few years to fill these pages with my humble scientific endeavors, I can now appreciate how the people I met during this journey have influenced me to grow into a (hopefully) better and more mature person than the one who walked through the beautiful Purdue campus five years ago. Although it is impossible to do justice to everyone among them, I shall try my best to convey my gratefulness in these following paragraphs.

At the very beginning, I would like to express my immense gratitude for my academic advisor, Prof. Xiulin Ruan, for helping me navigate the complex Ph.D. journey and providing inspiration and encouragement at every step along the way. Prof. Ruan's discipline and enthusiasm towards research, his patience and kindness towards his students and his great knowledge and insights in his research area are a few aspects among many that I greatly admire and have tried to imbibe in my work and my life at Purdue. Prof. Ruan has always encouraged me to hone my critical thinking capability and develop as an independent researcher, as well as pushed me to be more confident in my research work and form a coherent and enjoyable story that can get everyone interested in my research. I also must acknowledge the opportunities Prof. Ruan provided me to present my work in conferences at cool and exotic locations (such as Hawaii)! I am extremely grateful for the opportunity to be a part of his research group alongside so many talented researchers, and I hope to continue our academic and personal connection many years into my future. I could not have asked for a better academic advisor to undertake this journey through graduate life with.

I am also very grateful to the members of my doctoral committee - Prof. Xianfan Xu, Prof. Amy Marconnet and Prof. Mark Lundstrom. Throughout my stay at Purdue, I have been fortunate to interact with them in different capacities involving teaching and research,

and have undoubtedly benefitted from their guidance. Moreover, their insightful comments and feedback have helped me to construct a better dissertation. I am also very grateful to my collaborators in and out of Purdue: Prof. Jesse Maassen at Dalhousie University; Dr. Shashishekhar Adiga and Colleen Reynolds; Dr. Xufeng Wang at Purdue University; Prof. Yue Wu, Dr. Xiao Yang and Zhe Li at Iowa State University; Prof. Hua Bao and Wei Han at Shanghai Jiao Tong University; Prof. David Warsinger and Yuhang Fang, and Prof. Peide Ye and Jinhyun Noh at Purdue University. Working on the various research projects with them have provided me a strong breadth outside of my own research field. I would like to express my sincere gratitude to everyone in the graduate, business and main offices at the School of Mechanical Engineering at Purdue.

I would like to thank the members of the Nanoscale Energy Transport and Conversion Laboratory at Purdue, all of whom have been a great source of inspiration and encouragement to me during my stay here. I have been fortunate to learn from Dr. Zuyuan Wang, Dr. Tianli Feng, Dr. Jingjing Shi, Dr. Zexi Lu and Dr. Xiangyu Li, who were the senior members of the group when I joined and made me feel welcome right from the start. In particular, I am very grateful to Tianli, who, aside from being a prolific researcher, also served as a great mentor to me during my first two years; he is the first person I reach out to for research advice even today. I greatly enjoyed my time here with my other lab members: Joe, Victoria, Dedeepya, Xiaolong, Zhen, Zherui, Andrea, Luis, Jake, Adam, Zixin and Ioanna. I will always remember the great times we had at Prof. Ruan's parties with good food, basement games, and of course, karaoke!

Purdue has been my home for the last five years, and along with it came a family who have been the reason I now wish these years did not pass so quickly. Throughout these years, I have been fortunate to meet a group of people with whom I have been able to share all my good and bad experiences. Sayantan, Arindam, Sreya, Indrani, Aritra, Somrita, Srishti, Ashesh, Sayan, Esha, Krishnakali, Satarupa, Amartya and Arnob - I will cherish the memories made, dinners made and eaten, movies watched, concerts performed and laughters shared with all of you.

No amount of gratitude can be enough for highlighting the constant love and unwavering support of my parents during these five years. They have encouraged me when I was down,

cheered me on towards my successes and never let me lose sight of my goal in life. It has been especially hard for us to not be able to see each other for almost a year and a half during the pandemic. It is due to their sacrifices in life that I am able to stand where I am in my life today. I would also like to express my love and gratefulness towards my grandfather, and dearly wish he was here to see his aspirations for me be fulfilled.

Finally, I would like to express my deepest gratitude for the most special person in my life: my partner, Sanchari. Thank you for being a constant pillar of love and support in my life for as long as I have known you. From taking me on my first supermarket shopping trip in the US, to getting the COVID vaccine and being able to finally step outside after a year, you have been there to hold my hand every step of the way. Everyday you continue to show me the path to becoming a better researcher and a better person, and I hope that we can share many more firsts of our lives together.

# TABLE OF CONTENTS

LIST OF TABLES . . . . .	10
LIST OF FIGURES . . . . .	11
ABSTRACT . . . . .	16
1 INTRODUCTION . . . . .	19
1.1 Motivation for thermal transport research . . . . .	21
1.1.1 Thermoelectric energy systems . . . . .	21
1.1.2 Thermal management of electronics . . . . .	23
1.1.3 Thermal barrier coatings . . . . .	24
1.2 Overview of thermal transport in nanostructures . . . . .	25
1.2.1 The concept of phonons . . . . .	26
1.2.2 Phonon transport in nanostructures . . . . .	27
1.3 Theoretical methods for predicting phonon transport properties . . . . .	29
1.3.1 Lattice dynamics calculations . . . . .	29
1.3.2 First principles calculations . . . . .	31
1.3.3 Molecular dynamics simulations . . . . .	32
1.3.4 Spectral phonon properties . . . . .	36
1.4 Machine learning methods in thermal transport . . . . .	38
1.4.1 Importance of machine learning in thermal transport research . . . . .	38
1.4.2 Machine learning based interatomic potentials . . . . .	40
1.4.3 Neural network prediction of thermal transport properties . . . . .	43
1.4.4 Metaheuristic methods for nanostructure design optimization . . . . .	44
1.5 Objectives and organization of this thesis . . . . .	46
2 DEVELOPMENT OF INTERATOMIC POTENTIALS AND PREDICTION OF THERMAL TRANSPORT IN BULK $\text{Sb}_2\text{Te}_3$ . . . . .	49
2.1 Electronic structure and phonon dispersion . . . . .	51
2.2 Classical interatomic potential parameters . . . . .	57

2.3	Molecular dynamics simulations of lattice thermal conductivity . . . . .	61
2.4	Phonon modal relaxation time and thermal conductivity accumulation . . . .	64
2.5	Conclusions . . . . .	68
3	THERMAL CONDUCTIVITY AND INTERFACIAL THERMAL RESISTANCE IN $\text{Bi}_2\text{Te}_3\text{-Sb}_2\text{Te}_3$ MULTILAYER STRUCTURES FROM MOLECULAR DYNAM- ICS . . . . .	69
3.1	Methodology . . . . .	70
3.1.1	Simulation materials . . . . .	70
3.1.2	Molecular dynamics simulations . . . . .	71
3.1.3	Modified Landauer transport calculation . . . . .	74
3.2	Results and discussions . . . . .	77
3.2.1	Interfacial thermal conductance . . . . .	77
3.2.2	Thermal conductivity of superlattices . . . . .	79
3.3	Conclusions . . . . .	81
4	MACHINE LEARNING MAXIMIZED ANDERSON LOCALIZATION OF PHONONS IN APERIODIC SUPERLATTICES . . . . .	82
4.1	Introduction . . . . .	82
4.2	Simulation methods . . . . .	84
4.2.1	Designing RML structures . . . . .	84
4.2.2	Non-equilibrium molecular dynamics simulations . . . . .	85
4.2.3	Genetic Algorithm based optimization method . . . . .	86
4.3	Results and discussions . . . . .	88
4.3.1	Manual intuition-based search for the minimum RML thermal con- ductivity . . . . .	88
4.3.2	Genetic Algorithm-based search for the minimum RML thermal con- ductivity . . . . .	91
4.3.3	Influence of average RML period on the minimum thermal conductivity	92
4.3.4	Degree of randomness . . . . .	93
4.4	Conclusions . . . . .	96

5	AN ITERATIVE MACHINE LEARNING APPROACH FOR DISCOVERING UN-EXPECTED THERMAL CONDUCTIVITY ENHANCEMENT IN APERIODIC SUPERLATTICES . . . . .	97
5.1	Introduction . . . . .	97
5.2	Simulation methods . . . . .	100
5.2.1	Non-equilibrium molecular dynamics simulations . . . . .	100
5.2.2	Convolutional neural network-based prediction of thermal conductivity . . . . .	101
5.3	Results and discussions . . . . .	105
5.3.1	Manual random search for higher thermal conductivity RMLs . . . . .	105
5.3.2	Machine learning accelerated search for higher thermal conductivity RMLs . . . . .	107
5.3.3	Contribution of interfacial resistance towards $\kappa_l$ enhancement . . . . .	111
5.4	Conclusions . . . . .	112
6	MACHINE LEARNING OPTIMIZED APERIODIC SUPERLATTICES WITH HIGH REFLECTIVITY FOR THERMAL BARRIER COATINGS . . . . .	114
6.1	Introduction . . . . .	114
6.2	Simulation methods . . . . .	117
6.2.1	Materials and multilayer structures . . . . .	117
6.2.2	Transfer matrix method . . . . .	118
6.2.3	Genetic Algorithm optimization of multilayer structure . . . . .	120
6.3	Results and discussions . . . . .	123
6.3.1	Reflectivity of multilayer structures and effect of randomness . . . . .	123
6.3.2	Genetic Algorithm based optimization of multilayer structure for high reflectivity . . . . .	127
6.4	Conclusions . . . . .	131
7	SUMMARY AND FUTURE DIRECTIONS . . . . .	133
7.1	Summary . . . . .	133
7.1.1	Atomistic simulations of thermal transport in $\text{Sb}_2\text{Te}_3$ and $\text{Bi}_2\text{Te}_3$ nanostructures . . . . .	133



7.1.2	Machine learning accelerated discovery of non-intuitive phonon transport in nanostructures . . . . .	134
7.1.3	Machine learning accelerated discovery of multilayered photonic structures for thermal barrier coatings . . . . .	135
7.2	Future directions . . . . .	136
7.2.1	Thermal transport in heirarchically disordered systems . . . . .	137
7.2.2	Machine learning accelerated prediction of four phonon scattering rates in solids . . . . .	138
REFERENCES . . . . .		140
VITA . . . . .		166

## LIST OF TABLES

2.1	Fitted short-range Morse potential parameters for $\text{Sb}_2\text{Te}_3$ . $D_e$ is the depth of the potential well, $a$ is a measure of bond stiffness, $r$ is the pairwise atomic distance and $r_c$ is the cutoff distance . . . . .	58
2.2	Computation of elastic constants and bulk modulus using fitted potential parameters and comparison with <i>ab initio</i> calculations. All quantities are in Gigapascals.	59

# LIST OF FIGURES

1.1	Contribution of various renewable and non-renewable energy sources to net global energy consumption for the years 2009 and 2018, plotted using the data obtained from Ref. [1] . . . . .	20
1.2	Energy flow chart showing the estimated energy consumption in the United States in 2019. Reproduced from Ref. [13] . . . . .	21
1.3	Thermal conductivity of various materials calculated using atomistic simulation techniques (DFT and Pierls-Boltzmann Transport equation). Reproduced from Ref. [70] with data sources compiled in the same Ref. . . . .	39
1.4	Phonon dispersion along high symmetry directions predicted using different inter-atomic potentials as well as a machine learning method (Gaussian approximation potential). Reproduced from Ref. [77] . . . . .	41
1.5	Schematic of a fully-connected neural network showing one input layer, two hidden layers and an output layer . . . . .	44
2.1	Quintuple-layered crystal structure of $\text{Sb}_2\text{Te}_3$ showing rhombohedral (right) and hexagonal (left) unit cells . . . . .	52
2.2	Electronic band structure of $\text{Sb}_2\text{Te}_3$ along some high symmetry directions computed using DFT . . . . .	53
2.3	Phonon density of states of $\text{Sb}_2\text{Te}_3$ computed from fitted interatomic potential parameters (solid line), <i>ab initio</i> calculations (dashed line) and experimental values from [122] (circles) . . . . .	54
2.4	Schematic showing the generation of the <i>ab initio</i> energy surface. The circles represent different configurations used in the energy surface such as the equilibrium configuration (a), displacements of atom(s) at fixed lattice constant (b,c and d), variation of lattice constant with atoms fixed at equilibrium positions (e) and displacement of atom(s) at varied lattice constant (f) . The dashed line represents the classical interatomic potential fitted to the energy surface . . . . .	55
2.5	Phonon dispersion of $\text{Sb}_2\text{Te}_3$ along some high-symmetry directions computed from <i>ab-initio</i> calculations (broken line), fitted interatomic potential parameters (solid line) and experimental values from Ref. [123] (circles) . . . . .	60
2.6	MD predicted thermal conductivity in in-plane and cross-plane directions and $1/T$ fitting compared with experimental data (Ref. [20], [130]), calculations using a modified Calloway model (Ref. [131], [132]) and BTE + 3 phonon calculations (Ref [133]) . . . . .	63

2.7	(a) Anharmonic phonon dispersion at 300K from NMA (triangles and broken lines), quasi-harmonic phonon dispersion (300K) from LD (dashed lines) and harmonic phonon dispersion (0K) from LD (solid lines) along the $\Gamma - Z$ direction (b) Relaxation times of phonons along the $\Gamma - Z$ direction (c) Relaxation times of low-frequency accoustic phonons along $\Gamma - Z$ , along with $f^{-2}$ fitting . . . . .	66
2.8	Accumulated thermal conductivity (%) with respect to phonon mean free path .	67
3.1	(a) Crystal structure of $\text{Bi}_2\text{Te}_3$ showing two quintuple layers, (b) Schematic of $\text{Bi}_2\text{Te}_3\text{-Sb}_2\text{Te}_3$ single interface and (c) superlattice with period $d_{SL}$ . (d) NEMD simulation domain, showing the fixed layers of atoms at each end, the hot and cold baths and the direction of heat flux through the system in between. (d) Representative temperature profile for the single interface structure, showing the temperature drop $\Delta T_i$ at the interface. . . . .	71
3.2	(a) Phonon dispersion along the high symmetry $\Gamma - Z$ (cross-plane) direction in bulk $\text{Bi}_2\text{Te}_3$ (left) and bulk $\text{Sb}_2\text{Te}_3$ (right). (b) Phonon density of states in bulk $\text{Bi}_2\text{Te}_3$ (blue) and bulk $\text{Sb}_2\text{Te}_3$ (red) . . . . .	76
3.3	(a) Variation of thermal conductance of $\text{Bi}_2\text{Te}_3\text{-Sb}_2\text{Te}_3$ interface with temeprature, calculated using NEMD simulations (solid boxes) and the modified Landauer approach with DMM transmission coefficients (dashed line) (b) Phonon transmission coefficients from $\text{Bi}_2\text{Te}_3$ to bulk $\text{Sb}_2\text{Te}_3$ calculated using DMM . .	78
3.4	(a) Variation of $1/\kappa$ with $1/L$ for the $1 - 1$ and $4 - 4$ $\text{Bi}_2\text{Te}_3\text{-Sb}_2\text{Te}_3$ SLs, and the bulk thermal conductivity calculated by extrapolating the linear fit to infinite length (b) Variation of the $N - N$ $\text{Bi}_2\text{Te}_3\text{-Sb}_2\text{Te}_3$ SL $\kappa$ with SL period calculated using NEMD simulations (blue squares). Experimental data by Venkatasubramanian[16] are plotted for comparison (orange circles) . . . . .	80
4.1	Representative structures showing (a) superlattice of period 4.4 nm and (b) random multilayer with the same average period. Inset shows encoding of the RML structure in the GA as an $N$ -bit array, where each bit is assigned 1 or 2 if the unit cell is Si or Ge respectively. (c) Schematic of the NEMD simulation setup showing the RML sandwiched between two heat baths which are thermostatted to impose a heat flux through the system. . . . .	84
4.2	Schematic of the genetic algorithm based optimzation method showing the different steps involved. The GA population is initialized randomly with a chosen number of members and the fitness of each member is based on its thermal conductivity evaluated using NEMD simulations. The stopping criteria is checked and if it is not achieved, selection, crossover and mutation operations are carried out on the best individuals to obtain the next generation. . . . .	86

4.3	(a) Variation of thermal conductivity with average period length for N-N superlattices (red squares), RML structures obtained using manual intuition-based optimization (diamonds) and RML structures obtained using machine-learning based optimization (filled circles). The minimum RML thermal conductivity obtained from our optimization algorithm occurs at a smaller average period than that at which the minimum superlattice thermal conductivity is observed. The dashed purple line marks the random alloy limit. (b) RML structure with minimum thermal conductivity obtained from a manual optimization, (c) RML structure with minimum thermal conductivity obtained from a machine-learning based optimization, and (d) RML structure with average period below $\bar{d}_{min, RML}$ .	89
4.4	Variation of (a) thermal conductivity and (b) average RML period of the population with each iteration of the genetic algorithm based search process. The blue circles mark the best individual (lowest $\kappa$ ) of each generation . . . . .	90
4.5	(a) Dependence of thermal conductivity of RML structures on the degree of randomness (DOR) as defined in the text. The orange circles and dashed lines represent the lower bound of thermal conductivity obtained using our machine-learning based search process. For the four structures marked in the plot, the calculated thermal boundary resistances of all interfaces in each of the structures, superimposed on the visualization of the RML structures themselves, are shown in figures (b)-(e). . . . .	94
5.1	Schematic of the NEMD simulation setup showing the multilayer nanostructure (SL or RML) sandwiched between two thermal baths. A layer of atoms is fixed at each end to impose fixed boundary conditions. The corresponding temperature profile is also shown. . . . .	100
5.2	Schematic of the convolutional neural network architecture. The SL or RML structure is encoded as a binary array and used as the input layer. This is followed by a series of 1-D convolutional layers consisting of multiple feature kernels. A max-pooling layer is added to reduce the feature sizes. A flatten layer after the 1-D convolutional layers passes the features to a fully connected layer. The output layer consisting of a single node provides the predicted thermal conductivity. . . . .	102
5.3	(a) Schematic of the Si/Ge periodic SL (left) and aperiodic SL or RML (right). (b) Variation of $\kappa_l$ with average period at 300 K for RML structures generated during the manual random search (triangles) and the machine learning accelerated search (circles). The thermal conductivities of the reference $N - N$ superlattices are indicated by the diamonds. (b) Probability distributions of thermal conductivities (W/mK) of the RML structures generated by a manual search (blue bars) and the ML search (yellow bars). The region spanned by the thermal conductivities of the $N - N$ SLs is shaded in red. . . . .	105
5.4	Schematic of the iterative search algorithm used to discover unexpected thermal conductivity ( $\kappa_l$ ) enhancement in aperiodic superlattice systems. . . . .	107

5.5	(a) Variation of testing MAPE (black squares, left axis) and RMSE (red squares, right axis) with each iteration of the iterative search process for the 20 UC RML system. The top axis indicates the size of the dataset on which the CNN is trained in that iteration of the search (b) Comparison of CNN predicted $\kappa_l$ and NEMD calculated $\kappa_l$ (true value) for the dataset of RML structures. The shaded area represents a $\pm 0.1$ W/mK bound from $y = x$ . (c) Thermal conductivities of 20 UC RMLs sampled by the random search (squares) and the CNN accelerated search (circles) with total computational time spent. The dashed line represents the $\kappa_l$ of the 5-5 SL structure with error bounds. (d) The 20 UC and 40 UC RML structures with higher thermal conductivities than the corresponding SLs which were identified by the CNN accelerated search. . . . .	109
5.6	Calculated thermal resistances at all interfaces (yellow triangles) in three different 40 UC RML structures: (a) RML with high $\kappa$ identified by the ML enabled search (b) 5-5 SL (c) RML with low $\kappa$ identified by manual random search. The RML structures are underlaid for ease of visualization. (d) Comparison of the total interfacial thermal resistance (black squares) and total thermal resistance (red squares) for the three RML structures (a-c). . . . .	111
6.1	(a) Schematic of the multilayer system with total length $L$ , composed of $N$ layers with thicknesses $d_1, d_2 \dots d_N$ . The field amplitudes within each layer are shown, along with the incident and final transmitted fields. (b) A representative plot of spectral reflectivity vs. wavelength for a multilayer system. The shaded plot in the background represents the shape of the blackbody radiation spectrum at $T = 1500\text{K}$ . . . . .	118
6.2	(a) Schematic of the Genetic Algorithm (GA) based optimization process, showing the implementation of the selection, crossover and mutation steps. . . . .	121
6.3	(a) Variation of total reflectivity with average layer thickness for $\text{CeO}_2\text{-MgO}$ periodic superlattice (SL) structures for total thicknesses of $1 - 50\mu\text{m}$ . The spectral reflectivity vs. wavelength is shown for three different structures with total thickness of $5\mu\text{m}$ and average layer thickness of (b) $d_{avg} = 100\text{nm}$ , (c) $d_{avg} = 278\text{nm}$ which gives the highest reflectivity among SLs with total thickness of $5\mu\text{m}$ , and (d) $d_{avg} = 625\text{nm}$ . The shaded plot in the background represents the shape of the blackbody thermal radiation spectrum at $T = 1500\text{K}$ . . . . .	124
6.4	Total reflectivity vs. average layer thickness, showing the effect of randomizing the superlattice layer thicknesses by $\delta = 10, 20, 40$ and $60\%$ , for two total thicknesses of (a) $L = 5\mu\text{m}$ and (b) $L = 50\mu\text{m}$ . The spectral reflectivity vs. wavelength is plotted for comparison between two $5\mu\text{m}$ structures with (c) $\delta = 0\%$ (perfectly periodic) and (d) $\delta = 40\%$ ; and for two $50\mu\text{m}$ structures with (e) $\delta = 0\%$ (perfectly periodic) and (d) $\delta = 40\%$ . The shaded plot in the background represents the shape of the blackbody thermal radiation spectrum at $T = 1500\text{K}$ . (Inset multilayer structures are for visual aid only and do not represent the actual structures) . . . . .	126

6.5	(a) Evolution of maximum reflectivity identified by the genetic algorithm (GA) optimizer vs. generation of optimization, for four different total thicknesses of 5, 10, 20 and $30\mu\text{m}$ (b) The average layer thicknesses of all individuals in the population (red crosses) at each generation of the GA optimization run for a total thickness of $10\mu\text{m}$ . The solid line shows the average layer thickness of the RML with highest reflectivity at each generation of the optimization process. (c) Design of the GA-optimized RML structures with high reflectivity for three total thicknesses of 5, 10 and $20\mu\text{m}$ . . . . .	128
6.6	Spectral reflectivity vs. wavelength for three multilayer structures with total thickness of $10\mu\text{m}$ : (a) GA-optimized RML with high reflectivity, (b) periodic SL with same average layer thickness, and (c) an unoptimized RML structure with same average layer thickness. The field intensity distribution vs. position along the multilayer structure is shown for the same structures for a wavelength of $1.84\mu\text{m}$ : (d) GA-optimized RML with high reflectivity, showing significant field enhancement, (e) periodic SL with same average layer thickness, and (f) an unoptimized RML structure with same average layer thickness. The $x$ -direction denotes the stacking direction of the multilayer structures. . . . .	130
7.1	Generation of heirarchically disordered superlattice systems with perturbations in layer thicknesses, interface mixing and defects (left) and the interface with machine learning algorithms for prediction and optimization (right) . . . . .	137

# ABSTRACT

The recent decades have witnessed increased efforts to push the efficiency of energy systems beyond existing limits in order to keep pace with the rising global energy demands. Such efforts involve finding bulk materials and nanostructures with desired thermal properties such as thermal conductivity ( $\kappa$ ). For example, identifying high  $\kappa$  materials is crucial in thermal management of vertically integrated circuits (ICs) and flexible nanoelectronics, which will power the next generation personal computing devices. On the opposite end of the spectrum, designing ultra-low  $\kappa$  materials is essential for improving thermal barrier coatings in turbines and creating high performance thermoelectric (TE) devices for waste heat harvesting. In this dissertation, we identify nanostructures with such extreme thermal transport properties and explore the underlying phonon and photon transport mechanisms. Our approach follows two main avenues for evaluating potential candidates: (a) high fidelity atomistic simulations and (b) rapid machine learning-based property prediction and design optimization. The insight gained into the governing physics enables us to theoretically predict new materials for specific applications requiring high or low  $\kappa$ , propose accelerated design optimization pathways which can significantly reduce design time, and advance the general understanding of energy transport in semiconductors and dielectric materials.

$\text{Bi}_2\text{Te}_3$ ,  $\text{Sb}_2\text{Te}_3$  and nanostructures have long been the best TE materials due to their low  $\kappa$  at room temperatures. Despite this, computational studies such as molecular dynamics (MD) simulations on these important systems have been few, due to the lack of a suitable interatomic potential for  $\text{Sb}_2\text{Te}_3$ . We first develop interatomic potential parameters to predict thermal transport properties of bulk  $\text{Sb}_2\text{Te}_3$ . The parameters are fitted to a potential energy surface comprised of density functional theory (DFT) calculated lattice energies, and validated by comparing against experimental and DFT calculated lattice constants and phonon properties. We use the developed parameters in equilibrium MD simulations to calculate the thermal conductivity of bulk  $\text{Sb}_2\text{Te}_3$  at different temperatures. A spectral analysis of the phonon transport is also performed, which reveals that 80% of the total cross-plane  $\kappa$  is contributed by phonons with mean free paths (MFPs) between 3-100 nm.



We then use MD simulations to calculate phonon transport properties such as thermal conductance across  $\text{Bi}_2\text{Te}_3$  and  $\text{Sb}_2\text{Te}_3$  interface, which may account for the major part of the total thermal resistance in nanostructures. By comparing our MD results to an elastic scattering model, we find that inelastic phonon-phonon scattering processes at higher temperatures increases interfacial conductance by providing additional channels for energy transport. Finally, we calculate the thermal conductivities of  $\text{Bi}_2\text{Te}_3/\text{Sb}_2\text{Te}_3$  superlattices (SLs) of varying period. The results show the characteristic minimum thermal conductivity, which is attributed to the competition between incoherent and coherent phonon transport regimes. Our MD simulations are the first fully predictive studies on this important TE system and pave the way for further exploration of nanostructures such as SLs with interface diffusion and random multilayers (RMLs).

The MD simulations described in the previous section provide high-fidelity data at a high computational cost. As such, manual intuition-based search methods using these simulations are not feasible for searching for low-probability-of-occurrence systems with extreme thermal conductivity. In view of this, we use machine learning (ML) techniques to accelerate and efficiently perform nanostructure design optimization within such large design spaces. First, we use a Genetic Algorithm (GA) based optimization method to efficiently search the design space of fixed length Si/Ge random multilayers (RMLs) for the structure with lowest  $\kappa$ , which is found to be lower than the SL  $\kappa$  by 33%. By comparing thermal conductivity and interface resistances between optimal and sub-optimal structures, we identify non-intuitive trends in design parameters such as average period and degree of randomness of layer thicknesses.

While machine learning (ML) has shown increasing effectiveness in optimizing materials properties under known physics, its application in discovering new physics remains challenging due to its interpolative nature. We demonstrate a general-purpose adaptive ML-accelerated search process that can discover unexpected lattice thermal conductivity enhancement in aperiodic superlattices (SLs) as compared to periodic superlattices, with implications for thermal management of multilayer-based electronic devices. We use molecular dynamics simulations for high-fidelity calculations of  $\kappa$ , along with a convolutional neural network (CNN) which can rapidly predict  $\kappa$  for a large number of structures. To ensure accurate prediction for the target unknown SLs, we iteratively identify aperiodic SLs

with structural features leading to locally enhanced thermal transport and include them as additional training data for the CNN. The identified structures exhibit increased coherent phonon transport owing to the presence of closely spaced interfaces.

We also demonstrate the application of ML in optimization of photonic multilayered structures with enhanced reflectivity to radiation heat flux, which is required for applications such as high temperature thermal barrier coatings (TBCs). We first perform a systematic variation of design parameters such as total thickness and average layer thickness of CeO<sub>2</sub>-MgO multilayers, and quantify their influence on the spectral and total reflectivity. The effect of randomization of layer thicknesses is also studied, which is found to increase the reflectivity due to localization of photons in certain spatial regions of the multilayer structure. Next, we employ a GA search method which can efficiently identify RML structures with reflectivity enhancements of  $\sim 22\%$ ,  $20\%$ ,  $20\%$  and  $10\%$  over that obtained in randomly generated RML structures for total thicknesses of 5, 10, 20 and  $30\mu\text{m}$  respectively. We also calculate the spectral reflectivity and the field intensity distribution within the optimal and sub-optimal RML structures. We find that the electric field intensity can be significantly enhanced within certain spatial regions within the GA-optimized RMLs in comparison to non-optimized and periodic structures, which implies the high degree of randomness-induced photon localization leading to enhanced reflectivity in the GA-optimized structures.

In summary, our work advances the design or search for materials and nanostructures with targeted thermal transport properties such as low and high thermal conductivity and high reflectivity. The new insights provided into the underlying physics will guide the design of promising nanostructures for high efficiency energy systems.

# 1. INTRODUCTION

It is not an exaggeration to say that energy is the true currency of modern society. The last few decades have witnessed an unprecedented rise in the ubiquitousness of different energy systems in all facets of life, from transportation to manufacturing, and from electronic appliances to household conveniences. With the constant improvement of these technologies everyday, the world is moving towards an ever-growing demand for energy production. Yet, the fact that most of our energy generation systems still depend on non-renewable fossil fuel sources poses a major crisis to meeting this demand in a sustainable and efficient manner. Figure 1.1 shows the contribution of various renewable and non-renewable energy sources to the total global energy consumption at the extremes of a ten year period[1], where the majority ( 87% and 85% for 2009 and 2018 respectively) is contributed by fossil fuel based sources. Naturally, the need for a constant and renewable source of energy has driven large scale research efforts for developing alternative sustainable energy sources for several decades. Although the results of such efforts have lead to a visible increase in the utilization of renewable energy sources as seen in the inset of Fig. 1.1, the majority of these systems are still limited by their high cost and low performance relative to conventional coal-, oil- and natural gas-based systems. This has led to concentrated efforts in improving the efficiencies of renewable energy systems in order to transition to a sustainable energy economy.

One of the major challenges encountered in development of highly efficient energy systems is managing thermal transport. Heat transfer through solids has a wide and rich range of characteristics which can be efficiently harnessed in various applications such as thermal energy storage systems[2], thermal barrier coatings[3], thermoelectric energy generators[4]–[6], photovoltaic energy generators[7], thermal switches[8], [9], thermal management in electronics[10], thermal interface materials[11] and phase change materials[12]. The different thermal profiles arising in these systems creates the need to understand and manipulate thermal transport in materials with thermal properties spanning a wide range. This is most commonly translated to finding systems with various ranges of thermal conductivities ( $\kappa$ ), which is a measure of how easily heat is transported from one region of the material to another. For example, while thermoelectric devices require materials with low thermal

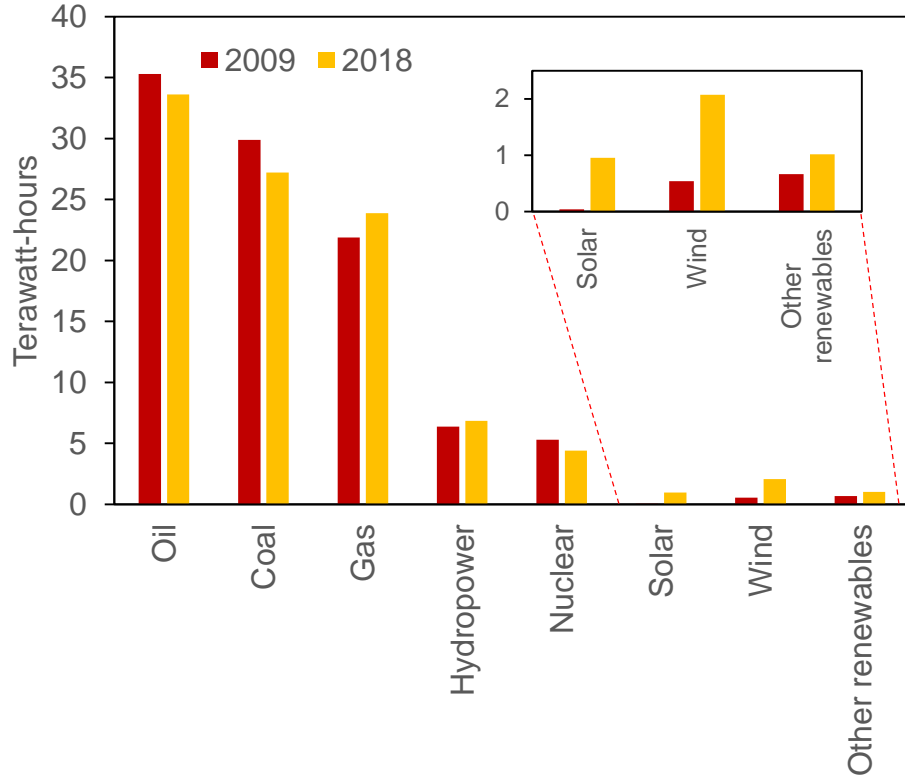


**Figure 1.1.** Contribution of various renewable and non-renewable energy sources to net global energy consumption for the years 2009 and 2018, plotted using the data obtained from Ref. [1]

conductivity, the opposite is needed for efficient heat dissipation in electronic packages. Moreover, the reduction of dimensions of the point-of-application of these energy systems to micro- and nano-scales can lead to significantly different thermal transport physics from those at the macro-scale. A notable instance of this is the commonly known breakdown of Fourier’s law in systems with small length scales, which leads to length-dependent thermal transport in systems such as superlattices and nanowires. The focus of thermal transport research has, therefore, been on studying bulk materials as well as understanding and designing nanomaterial systems with targetted thermal transport properties. In the following section, we describe the motivation and previous efforts on study of thermal transport in materials with low and high thermal conductivities, namely, thermoelectric devices and thermal management in electronic packages.

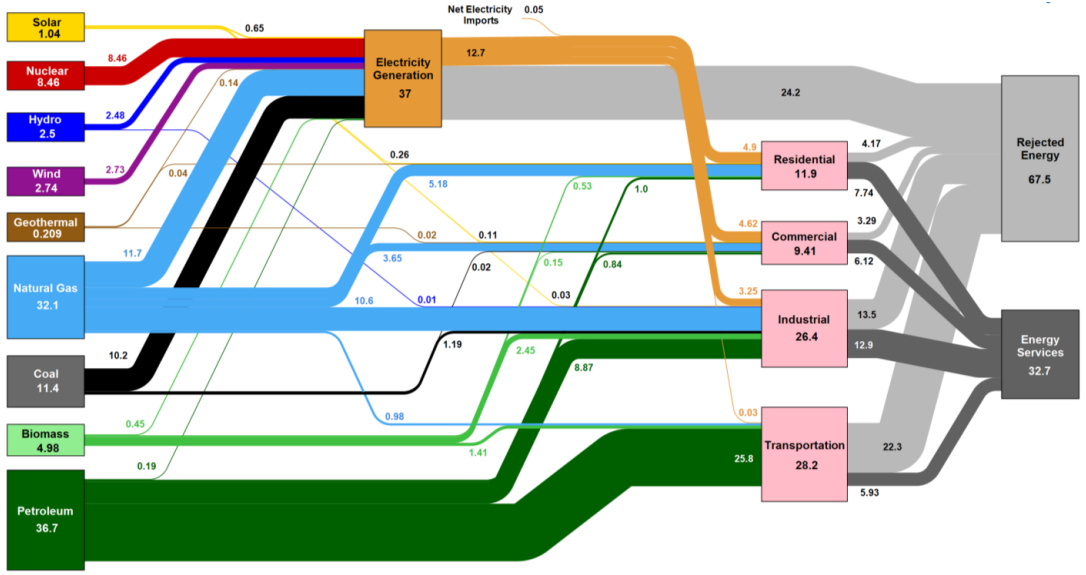


**Figure 1.2.** Energy flow chart showing the estimated energy consumption in the United States in 2019. Reproduced from Ref. [13]

## 1.1 Motivation for thermal transport research

### 1.1.1 Thermoelectric energy systems

In the past few decades, an increasing number of efforts have been devoted towards the development of high-performance thermoelectric (TE) materials for various applications such as thermoelectric energy harvesting and thermoelectric refrigeration. Thermoelectric energy generators (TEGs) provide a very attractive solution for converting thermal energy into electrical energy without any moving parts. It has been found that more than half of the total energy produced in the United States is dissipated as waste heat due to various inefficiencies[13], as shown in Fig. 1.2. Such large amounts of waste heat can be effectively utilized by TEGs to increase the overall efficiency of the combined system. On the other hand, thermoelectric cooling technologies can offer promising alternatives to traditional vapor compression systems in applications such as small scale refrigerators and systems deployed in remote and rural areas. Moreover, thermoelectric systems are only theoretically limited by the Carnot efficiency due to the absence of moving parts.

The performance of a thermoelectric material can be characterized by its figure of merit ( $ZT$ ), given by the expression

$$ZT = \frac{S^2 \sigma T}{\kappa_e + \kappa_l} \quad (1.1)$$

where  $S$  is the Seebeck coefficient,  $\sigma$  is the electrical conductivity and  $\kappa_e$  and  $\kappa_l$  are the electronic and lattice contributions to the thermal conductivity respectively. As is evident from the above expression, thermoelectric power generation devices benefit from materials with low thermal conductivity to maintain a temperature gradient across the device, as well as a high electrical power factor ( $S^2 \sigma$ ) to promote greater current flow. However, the coupled nature of electrical and thermal energy carriers, namely, electrons and phonons, in the crystalline or amorphous solids used in this systems makes this a non-trivial task.

For a long time, tellurides such as  $\text{Bi}_2\text{Te}_3$ ,  $\text{PbTe}$  and various alloys were found to be the best bulk thermoelectric materials at room temperature, displaying  $ZT$ s near 1. The breakthrough in achieving  $ZT$  values above 1 was achieved by the ability to create nanostructured materials or composite systems with ultra-low lattice thermal conductivities ( $\kappa_l$ ), while being able to retain high electrical transport properties. This has led to an exponential rise in laboratory demonstrations of high  $ZT$  proof-of-concept systems involving nanostructures and alloys of conventional TE materials such as  $\text{Bi}_2\text{Te}_3$  [14], as well as new materials such as perovskites and chalcogenides. However, the commercialization of such laboratory demonstrations into practical power generation systems has still remained in its infancy, largely due to the low efficiency of these proof-of-concept systems (the demonstrated  $ZT$ s are still far from the target  $ZT$  value of around 3 – 4 which would allow them to compete with traditional energy generation cycles). As a result, most commercial realizations of TE systems have been limited to specific applications only. For example, radioisotope thermoelectric generators (RTGs) have long been used for energy generation in space missions, involving  $\text{SiGe}$  and  $\text{PbTe}$  based materials. TE devices have also found significant use for power generation and cooling/refrigeration in remote areas, where access to conventional electric sources is limited, and small and portable modules can be efficiently deployed. Despite the success

of commercial TE devices in these niche domains, the widespread adoption of TE technology for mainstream power generation through waste heat recovery in industries and automobiles has not seen much success. Consequently, there is a pressing need to identify low-cost, easily available thermoelectric materials with ultra-low thermal conductivity and uncover the underlying heat transport physics leading to their attractive transport properties.

### **1.1.2 Thermal management of electronics**

Thermal management of consumer electronic devices, power electronics components, fuel cells and batteries is a major issue that can severely limit the performance or even lead to failure of such systems. In particular, the requirement of high-performance computers, laptops, cellular phones and data centers to perform an increasing number of operations in even shorter time scales has led to requirements for electronic packages with higher clock speeds and smaller dimensions. The evolution of integrated circuit research has closely followed the famous Moore’s law over a long time, with the number of transistors packed into an IC doubling roughly every two years. In recent years, however, the semiconductor industry has faced several hurdles in continuing along this path, including the problem of dissipating extremely large heat fluxes generated due to high levels of Joule heating within very small areas. The development of electronic components with even higher computing power, therefore, requires novel chip-cooling solutions enabled by high thermal conductivity materials.

Traditionally, single-phase and phase-change fluid cooling systems have been used as the most effective solutions for thermal management. These are usually employed in the form of heat pipes and microchannels with internal flow of water, or heat sinks with an external air flow driven by fans. However, with the rapid shrinkage of feature sizes of integrated circuits, it has become increasingly difficult to accommodate a cooling system with multiple components into a single electronic package. Moreover, the effectiveness of heat removal by these systems also depends on the thermal transport at the interface between the heat source and heat sink. As electronic devices go down to the nanoscale and thermal transport shifts from diffusive to ballistic regimes, this interfacial resistance may become the

bottleneck in the heat dissipation mechanism. This has led to extensive research on thermal interface materials (TIMs) which can reduce the thermal contact resistance between two surfaces and transport heat effectively to the heat sink. High thermal conductivity materials such as carbon nanotubes and graphene have been employed in TIMs to provide superior performance with respect to thermal greases. Despite their success, the roadmap towards even greater transistor densities in novel electronic packaging technologies, such as vertically stacked ICs, with higher heat generation rates, creates the requirement for better TIMs and heat sinking capabilities.

### **1.1.3 Thermal barrier coatings**

Another important challenge which drives thermal transport research is the efficient thermal isolation of energy system components subject to extreme operating conditions. For example, the efficiency of traditional gas turbines can be improved by increasing the turbine gas inlet temperature; however, in practice, this is severely limited by the thermal degradation of the turbine blades and rotors that can occur when temperatures reach close to the melting point. Thermal protection is also required in space applications, such as the need to protect the body of a spacecraft during re-entry through the earth's atmosphere, where air resistance can cause temperatures higher than 1500°C. In such cases, thermal barrier coatings (TBCs) are employed to insulate such components from extreme heat loads and prevent thermal degradation. An efficient TBC system sustains a significant temperature difference across itself, thus allowing for higher operating temperatures and increasing system lifetime. Traditionally, TBCs are designed to limit heat transport by conduction, which is generally the dominant thermal transport mechanism in the abovementioned applications. As a result, TBC materials are required to have low lattice thermal conductivity, high melting point and thermal stability, and matched coefficient of thermal expansion with the underlying substrate material to prevent cracking under thermal stresses. However, it has been found that at higher temperatures which are being targetted in modern energy systems, heat transport by radiation can play a large role in increasing substrate temperatures significantly[15] due to radiation heat transfer being proportional to the fourth power of temperature. Consequently,



TBCs designed for high temperature applications need to be able to prevent radiation heat transfer by having high reflectivity and low transmittance to the incoming radiation heat flux.

Due to the considerations for low lattice thermal conductivity and high melting point, ceramic materials have long been used for TBC applications. Yttria-stabilized zirconia (YSZ) is the most widely used material at standard temperatures of TBC application, and significant research has been conducted on its thermal properties, phase stability, mechanical properties and coating technology. However, the requirement of more efficient TBC systems and the push towards higher temperatures at which YSZ loses its phase stability has created the need to identify and employ other materials with lower phonon thermal conductivity. The influence of microstructures, defects and interfaces in such systems also needs to be systematically investigated from the atomic scale in order to effectively engineer TBC systems and nanostructures with hierarchical strategies of mitigating conductive thermal transport. As mentioned above, photon scattering mechanisms are also required for high temperature operations. A small number of studies have shown the benefit of using multilayered and functionally graded TBC systems, where transmission of incident photons is reduced due to photonic bandgaps and randomness-induced spatial photon localization. Given the benefits demonstrated by these systems, such strategies need to be systematically explored to identify optimal materials and composite systems that can provide excellent insulation against both conduction and radiation heat transfer.

## **1.2 Overview of thermal transport in nanostructures**

Thermal transport is the transfer of heat energy, either from one medium to another or between different parts of the same medium, due to differences in temperature. The three main mechanisms by which thermal energy is transported are conduction, convection and radiation. Among these, conduction is the main mode of heat transfer by direct material contact in solid objects, whereas convection is mainly responsible for transporting heat through bulk fluid motion. Radiation occurs for all bodies with a finite temperature, and takes place through propagation of electromagnetic waves without the need for a material medium. The

study of thermal transport invokes the definition of some fundamental energy carriers associated with these mechanism, namely photons, phonons, electrons and fluid molecules. The nature of propagation of energy via each of these fundamental carriers, along with the interactions among them, leads to varying thermal transport characteristics in different bulk materials and nanostructures. Study of these heat carriers is crucial to the identification of materials with extreme transport properties and designing nanostructures of different length scales.

### 1.2.1 The concept of phonons

Many of the applications mentioned above, such as thermoelectrics and thermal management systems, benefit greatly from being converted to entirely solid state devices. Consequently, a background on thermal transport in solids through conduction is provided to discuss the research advances and open challenges in this field. Thermal transport in crystalline solids with a defined lattice structure occurs through electrons as well as vibrational motions of the atoms. Although electrons can have the most significant contribution to thermal transport in metals, the transport in dielectrics such as semiconductors is governed by lattice vibrations. In this respect, the concept of *phonons* is extremely important to uncover the underlying transport physics. Phonons are the quantization of collective excitations of atoms in a lattice, also known as a normal mode. Thus, a phonon is a quantum mechanical description of the lattice waves occurring in a solid by which heat is transported across the medium. Each phonon mode in a material is defined by its wavevector  $\mathbf{k}$ , polarization  $j$  and frequency  $\omega(\mathbf{k}, j)$ .

Phonons are quasiparticles which can have both particle- and wave-like characteristics. As particles, phonons can scatter through collisions with other phonons, electrons, as well as other lattice perturbations such as defects, isotopes, boundaries and interfaces. The collisions preserve the total energy of the phonons, but the total crystal momentum can be conserved only upto a difference in the reciprocal lattice vector  $\mathbf{G}$  or its multiples:

$$\sum_i E_i^{(i)} = \sum_i E_i^{(f)} \quad (1.2)$$

$$\sum_i \mathbf{k}_i^{(i)} = \sum_i \mathbf{k}_i^{(i)} + n\mathbf{G} \quad (1.3)$$

The phonon scattering processes are defined as Normal process or Umklapp processes accordingly as  $n = 0$  and  $n \neq 0$  respectively. Normal (N) processes do not alter the direction of propagation of phonons and do not provide resistance to thermal transport directly. On the other hand, Umklapp (U) processes are responsible for providing resistance to the propagation of heat carrying phonons, which leads to a finite value of lattice thermal conductivity ( $k_l$ ). The thermal transport characteristics can, therefore, be tuned by controlling the rates of occurrence of these different scattering processes, or, equivalently, the time between scattering events which is the phonon relaxation time ( $\tau$ ).

The wave nature of a phonon is also important to explain phenomenon such as phonon confinement and phonon tunnelling in thin films and superlattice structures[16], [17]. This is specially important in structures such as superlattices, where phonons can undergo phase-preserved repeated reflections at multiple closely-spaced interfaces. The superposition of the incident phonon and its reflections can lead to destructive interference, which causes phonon confinement and inhibits phonon transport. Such effects have been acknowledged to be important in designing ultra-low thermal conductivity structures for thermoelectric devices and quantum cascade lasers.

### 1.2.2 Phonon transport in nanostructures

The thermal conductivity of a solid is contributed by different phonon modes with a range of wavelengths, frequencies, group velocities and scattering rates. Although the first three properties are generally governed by the lattice structure and the atomic basis, the final property, *i.e.* scattering rate, can be controlled by nanostructuring to tune the thermal

conductivity. For example, if scattering events between phonons and interfaces, defects, isotopes or grain boundaries is increased, the overall scattering rate can may be governed by these processes instead of the usual anharmonic phonon-phonon scattering. Since these leads to more changes in phonon momentum (Eq. 1.3) by U processes, the thermal conductivity can be appropriately modulated in these engineered structures.

Naturally, several approaches are commonly used to reduce thermal conductivity of materials for use in thermoelectric devices. For example, alloying has been a traditioanal approach to reducing the thermal conductivity of bulk materials. Alloys of bismuth telluride, antimony telluride and lead telluride had been found to be the best bulk materials at room temperature for a long period of time before the advent of nanostructuring. The discontinuity in lattice structure due to difference in masses of atoms creates scattering centers for phonons which can increase scattering rates. Such approaches have been demonstrated by studies on systems such as  $\text{Si}_x\text{Ge}_{1-x}$ [18], [19],  $\text{Bi}_x\text{Sb}_{2-x}\text{Te}_3$ [20], [21],  $\text{PbTe}_x\text{Se}_{1-x}$ [22], [23] and half-Heusler compounds[24]. More recently, the ability to create nanostrcutured bulk materials has led to even lower thermal conductivity in systems such as nanostructured bismuth antimony telluride bulk alloys [25]–[27].

Controlling phonon-boundary scattering in low dimensional nanostructures is another paradigm shift in the search for low thermal conductivity materials. Since most heat carrying long wavelength phonons are the effects of long range atomic periodicity, such phonon modes can be suppressed or scattered by reducing the lattice periodicity in a specific dimension. As a result, 2-D nanostructures such as thin films[28]–[30], van der Waal’s heterostructures[31]–[33] and superlattices have been extensively investigated for their unique thermal transport properties. In particular, the discovery graphene and other nanostructures of carbon such as nanotubes have been one of the most exciting phases for thermal transport research, due the the ultra-high thermal conductivity of these materials which make them excellent candidates for thermal management applications[34]–[38]. However, the initially high measurement of graphene thermal conductivity has been the result of much scrutiny, with recent measurements citing a reduced value. Alongside this, a significant discrepancy has been found to exist between the experimentally measured value and that obtained from standard atomistic simulation techniques such as first principle calculations[39]–[41], which has been attempted

to be explained newly discovered yet fundamentally critical concepts such as four phonon scattering[42].

Finally, we discuss phonon-interface scattering as an equally important method of modulating lattice thermal conductivity in composite materials. The importance of interfacial phonon modes to the contribution of thermal conductivity and thermal contact resistance has been extensively investigated[43], [44] and the existence of significant non-equilibrium between the phonon modes at the interface has been uncovered by atomistic simulation methods[45]. An important aspect of phonon transport across interfaces in nanostructured solids such as one-dimensional superlattices is the coupling of interfaces which gives rise to coherent phonon modes. The mechanism of formation and contribution to thermal conductivity of these coherent phonon modes has been explored in significant detail[16], [46]–[54]. The characteristics of thermal transport in these nanostructures are governed by the competing regimes of incoherent and coherent phonon dominated transport regimes. Wave interference effects become increasingly important at small periods, and the phase breaking of phonons does not take place before the phonons scatter at the interfaces. The repeated reflections at periodic interfaces give rise to a modified phonon spectra including coherent phonon modes. Although these phonon modes are not scattered at the periodically spaced interfaces, several methods have been investigated for suppressing coherent phonon contribution including introduction of interface roughness[55]–[57] and randomizing layer thicknesses leading to Anderson localization[55], [58]–[62].

### **1.3 Theoretical methods for predicting phonon transport properties**

#### **1.3.1 Lattice dynamics calculations**

Lattice dynamics is the calculation of atomic vibrations generally within an ordered crystalline lattice structure. Since phonons are quantized collective lattice vibrations, lattice dynamics calculations may be treated as the starting point when insight into phonon transport is required about a material or nanostructure. In these calculations, atoms in a lattice are treated as point masses coupled through harmonic or anharmonic springs. The force constants of the springs may be obtained by fitting to experimentally determined crystal

properties or by using appropriate interatomic potential parameters, which are explained in a subsequent section. The equations of motion of each atom in 3 coordinate directions are then written to form a system of  $3N$  equations, which can be further reduced to  $3n_b$  equations, where  $n_b$  is the number of atoms in a primitive cell, using translational symmetries. This system can be compactly represented by the form

$$[\mathbf{D}(\mathbf{k}) - \omega^2(\mathbf{k}, \nu)\mathbf{I}]\mathbf{e}(\mathbf{k}, \nu) = 0. \quad (1.4)$$

Equation 1.4 represents an eigenvalue problem where the eigenvector  $\mathbf{e}(\mathbf{k}, \nu)$  represents the wave-like solution of a phonon mode with wavevector  $\mathbf{k}$  and polarization  $\nu$  and the eigenvalue  $\omega(\mathbf{k}, \nu)$  is the phonon frequency.  $\mathbf{D}(\mathbf{k})$  is the dynamical matrix evaluated for the wavevector  $\mathbf{k}$  and  $\mathbf{I}$  is the identity matrix.

Each element in the dynamical matrix can be evaluated using the relation

$$D_{\alpha i}^{\beta j} = \frac{1}{\sqrt{M_\alpha M_\beta}} \Phi_{m\alpha i}^{n\beta j} \exp(i\mathbf{k} \cdot (\mathbf{r}_m - \mathbf{r}_n)). \quad (1.5)$$

Here, the calculation is performed between atoms in the  $\alpha$  basis position in the  $m^{th}$  unit cell and the  $\beta$  basis position in the  $n^{th}$  unit cell, and  $i, j$  denote the cartesian directions. The dynamical matrix entry consists of the corresponding force constant matrix element

$$\Phi_{m\alpha i}^{n\beta j} = \frac{\partial^2 \varphi}{\partial r_{m\alpha i} \partial r_{n\beta j}} \quad (1.6)$$

By calculating the force constant matrix in Eq. 1.6 and solving Eq. 1.4 for the set of eigenvalues and eigenvectors, we can obtain the phonon frequency dispersion over the Brillouin zone and the phonon density of states for a given material. Finally, the velocity of propagation of the phonon modes can be obtained by computing the group velocity as  $\mathbf{v}_g = \partial\omega/\partial\mathbf{k}$ .

### 1.3.2 First principles calculations

First principles calculations or *ab initio* methods is one of the most accurate methods used to calculate thermal transport properties of new materials using quantum mechanical calculations. The advantage of first principles methods is that the calculations do not depend on any experimentally fitted parameter, and so can be used for novel materials for which experimental data is not available. The most commonly used first principle methods are density functional theory (DFT) and tight binding (TB) calculations. In DFT calculations, the ground state electron density of a many-body system can be solved for using the variational principle and the Hohenberg-Kohn theorems, which states that the energy functional of the system is minimized by the ground state electron density. Moreover, this ground state density uniquely determines the properties of the system. In addition to electronic properties, phonon properties of the system such as phonon dispersion spectrum and density of phonon states can also be determined using the method of finite-differences, or in the framework of the density functional perturbation theory (DFPT). By calculating the differential change in the forces on atoms when one or more of them are given displacements from their equilibrium positions, the force constant matrix of the system can be determined.

One of the major drawbacks associated with first principles calculations is the high computational expense associated with performing quantum mechanical calculations. As a result, first principles cannot handle systems with more than a few hundred atoms, or over significantly longer time scales. Moreover, additional components such as spin polarized calculations or spin-orbital coupling, which is required to describe heavier elements, can add to the computational load. This problem becomes specially significant when nanostructures with a high surface-to-volume ratio needs to be simulated and the crystal symmetry is lost due to surface reconstruction. Additionally, ground state first principles calculations can predict properties at 0 K temperature only, where atoms are located at their equilibrium positions. This is not suitable for thermal transport calculations, where the anharmonicity of the lattice far from the equilibrium position plays a pivotal role. A commonly adopted solution to this problem is the use of a temperature dependent effective potential (TDEP), the details of which can be found elsewhere[63].

### 1.3.3 Molecular dynamics simulations

Molecular dynamics (MD) simulations are a classical approach to solving the trajectories of motion of the atoms or molecules in a system. Since phonon transport is an outcome of atomic vibrations in a lattice, MD simulations are able to reproduce phononic transport within lattices. In an MD simulation, the simulation domain which can consist of various types of atoms is run under different ensemble settings such as constant temperature, pressure, volume or total energy. For example, the velocities of the atoms are generally scaled after a fixed number of timesteps of the simulation to ensure that the kinetic energy remains constant in a constant temperature setting. In addition, one or more constraints can be added to the system to restrict certain degrees of freedom and allow phonon modes to propagate in a particular direction only. By appropriate use of periodic and fixed boundary conditions, MD simulations can simulate uniform bulk materials, nanocomposites as well as nanostructures with heterogeneous features such as an array of nanowires or different configurations of nanotubes. This makes MD simulations a suitable tool for predicting the transport properties of bulk materials and subsequently evaluate their performance as nanoscale systems used in different devices.

The advantage of MD simulations over first principles methods is the significantly smaller computational cost of MD simulations, which make them able to handle both large systems (containing millions of atoms) and much longer time scales (upto several nanoseconds). This gain in computational cost is because the classical MD simulation algorithm does not calculate the interaction forces between atoms at each timestep by solving complicated quantum mechanical equations like DFT or TB calculations. Instead, forces in MD are calculated quickly using a parameterized form for the potential energy of atoms in different environments, called the classical interatomic potential. The total energy of an atom may depend on contributions from one-body ( $V_1$ ), two-body ( $V_2$ ), three-body ( $V_3$ ) and further many-body terms as shown below:

$$V = \sum_i V_1(\mathbf{r}_i) + \sum_{i,j} V_2(\mathbf{r}_i, \mathbf{r}_j) + \sum_{i,j,k} V_3(\mathbf{r}_i, \mathbf{r}_j, \mathbf{r}_k) + \dots \quad (1.7)$$



Several forms of parameterization are possible for each of the above terms for a particular material, and the choice of an appropriate potential form is necessary to accurately reproduce the thermal transport properties of a material. For example, simple potential parametrizations considering two-body terms only are easily implemented in the MD simulation framework and are less expensive than higher order potentials, but are not suitable for accurately capturing optical phonon modes in charge polarized compounds. On the other hand, potentials involving three-body terms can reproduce optical phonon properties with greater accuracy, but are difficult to parametrize and use in MD simulations.

Another advantage of phonon transport calculations using MD simulations is that it can inherently capture all order of scattering mechanisms such as anharmonic phonon scattering, phonon-boundary scattering, interface scattering, and isotope or defect scattering. As a result, no empirically determined correlation or fitting parameter is required to include these terms, other than using an appropriate classical potential form. However, there are some limitations and caveats to using MD simulations as well. First of all, MD simulations are classical in their calculations, and as such cannot perform a quantum treatment of phonons which are Bosons following the Bose-Einstein distribution. Although certain quantum corrections to classical MD results have been proposed, they are not generally accepted to be accurate for all systems[64]. Consequently, MD simulations can provide reasonably accurate results in agreement with experiment for materials with low Debye temperatures such as  $\text{Bi}_2\text{Te}_3$  ( $\theta_D = 155K$ ), but show deviation from experimental results for materials with higher Debye temperatures such as graphene ( $\theta_D \sim 1800K$ ). Another limitation of MD simulations is the availability and accuracy of classical interatomic potentials for many complex materials. Parametrization of potential forms is a complex and high-risk process involving generation of a fitting dataset which must be tailored to suit the application of the potential. For example, if the potential is intended to be used to predict thermal transport properties, the potential parameters need to be fitted to lattice energies, atom forces and other experimental properties far from the equilibrium point to accurately sample the lattice anharmonicity. Moreover, potential parameters once fitted to a particular environment may not be transferable, i.e. suitable for application for the same type of atom in a different environment. This makes it difficult to predict properties such as phase change tempera-

tures, breaking and creation of bonds and surface reconstruction in nanostructures, by using a single potential form. More complicated bond-order potentials are used in such situations, but are more difficult to implement and can significantly slow down the computation time.

The calculation of phonon thermal transport properties using MD simulations can be done using two main ways: equilibrium molecular dynamics (EMD) and non-equilibrium molecular dynamics (NEMD). The following sections briefly describe the calculation of thermal conductivity using each of these methods.

### Equilibrium molecular dynamics simulations

We first discuss the calculation of thermal conductivity under the EMD framework. In this method, calculation of the thermal conductivity is done using the Green-Kubo linear-response formulation, which relates the statistical fluctuations in the heat current to the thermal conductivity tensor using the fluctuation-dissipation theorem. The heat current can be obtained from the MD velocities and forces as:

$$\mathbf{S} = \frac{d}{dt} \sum_i \mathbf{r}_i E_i, \quad (1.8)$$

where  $\mathbf{r}_i$  is the position vector of atom  $i$  and  $E_i$  is its energy. By calculating instantaneous heat current, the lattice thermal conductivity along any direction  $\alpha$  can be calculated using the Green-Kubo formula

$$\kappa_{l,\alpha} = \frac{1}{k_B V T^2} \int_0^\infty \langle S_\alpha(0) \cdot S_\alpha(t) \rangle dt, \alpha = x, y, z \quad (1.9)$$

Here,  $V$  is the volume of the simulation cell,  $T$  is the absolute temperature in Kelvin, and  $\langle S_\alpha(0) \cdot S_\alpha(t) \rangle$  represents the heat current autocorrelation function. (HCACF).

The advantage of using the EMD method is that the effect of the MD domain size on the thermal conductivity is small due to use of periodic boundary conditions, although a convergence study needs to be performed separately for each unique system. In addition, the calculation can be performed at a single temperature for the entire system without imposing

any temperature gradients which may change the transport properties locally. However, results of thermal conductivity from EMD simulations can display significant statistical fluctuations. In this case, ensemble averaging over a sufficient number of runs needs to be performed in order to arrive at converged value of thermal conductivity.

### **Non-equilibrium molecular dynamics simulations**

Under the framework of NEMD, the thermal conductivity of the system is calculated using the Fourier’s law. In this method, the atoms in two regions at either end of the system are chosen to serve as the heat source and heat sink. By thermostating the atoms to a higher and lower temperature for the heat source and heat sink respectively, one can then establish a constant temperature gradient and a corresponding heat current with the system under investigation. Conversely, the kinetic energies of the atoms in each region can be controlled by adding a constant energy rate to the atoms in the heat source and removing the same energy rate from the cold region, which sets up a constant heat flux through the system. This, in turn, leads to a temperature gradient at steady state. In either of these two ways, the thermal conductivity of the system can then be calculated from the steady state heat flux  $q$  and temperature gradient  $dT/dr$  as

$$\kappa_{l,\alpha} = \frac{q}{dT/dr_{\alpha}} \quad (1.10)$$

NEMD simulations are not affected by statistical fluctuations, and less number of runs are needed to get stable values for thermal conductivity. Since a temperature gradient of several Kelvins is usually imposed across nanometer length scales, this usually leads to an unphysically high heat fluxes as compared to experimental values. Nevertheless, a linear portion of the temperature gradient curve is generally obtained for most systems, from which thermal conductivity values can be extracted with good agreement with experiments. The main disadvantage of NEMD simulations is the significant effect of system size used in the simulations. This is primarily due to the use of non-periodic boundary conditions, which limits the wavelengths and mean free paths of phonons which can exist within the simulation domain. A common way to deal with this is to perform a linear fit to a plot of the inverse of

thermal conductivity with the inverse of the system length. By extrapolating the fitted line to infinite length, the bulk thermal conductivity can be obtained.

#### 1.3.4 Spectral phonon properties

The *ab-initio* and MD methods described above are suitable for providing estimates of the overall thermal transport properties such as thermal conductivity and interfacial conductance. However, phonon transport in solids occur a broad spectrum of phonon length scales ranging from the interatomic separation distances to even a few hundred nanometers. It is therefore crucial to understand the characteristics of propagation and the contribution to the overall thermal transport of each of these phonon modes. This is important to guide design of nanoscale devices, where, for example, low frequency acoustic phonon modes with long mean free paths can be preferentially scattered by defects and interfaces to achieve ultra-low thermal conductivity structures. Although classical MD simulations cannot provide insight into the frequency-dependent phonon transport properties by themselves, some post processing methods may be applied using the MD predicted trajectories, velocities and forces to calculate the spectral phonon properties.

#### Phonon normal mode analysis

The contribution of different phonon modes to the total lattice thermal conductivity can be calculated as the sum of the mode-wise thermal conductivities  $k_j$  of all phonon modes

$$\kappa_l = \sum_j \kappa_j = \sum_j (\mathbf{v}_\lambda \cdot \hat{n})^2 c_\lambda \tau_\lambda \quad (1.11)$$

Here  $\hat{n}$  is the chosen direction of thermal transport,  $\lambda$  represents the phonon mode  $(\mathbf{k}, \nu)$  with  $\mathbf{k}$  being the wave vector and  $\nu$  the polarization branch,  $c_\lambda$  is the phonon mode specific heat,  $\tau_\lambda$  is the relaxation time,  $\mathbf{v}_\lambda$  is the group velocity. The specific heat per phonon mode is given by  $c_\lambda = \hbar \omega_\lambda \partial n_\lambda^0 / \partial T = k_B x^2 e^x / (e^x - 1)^2$ , where  $x = \hbar \omega / k_B T$ , and the phonon occupation number  $n_\lambda^0 = 1 / (e^x - 1)$  according to the Bose-Einstein distribution. The phonon group velocity is given by the gradient of the phonon dispersion,  $v = d\omega / dk$ , where  $\omega$  is the phonon angular frequency.

In Equation 1.11, the phonon properties such as  $\omega$ ,  $c_\lambda$  and  $\mathbf{v}_\lambda$  can be readily obtained from lattice dynamics calculations as described above. The more challenging task is the determination of the spectral phonon relaxation time  $\tau_\lambda$  and, consequently, the mean free path  $\Lambda$  which is the average distance travelled by a phonon particles between two successive collisions. This can be obtained using the framework of *frequency domain normal mode analysis* (FD-NMA), which was initially developed by Wang *et al.*[65] and later extended by Shiomi and Maruyama,[66] De Koker,[67] Thomas *et al.*[68] and Feng *et al.*[69] According to lattice dynamics, the vibrations of atoms in real space can be mapped to the time-dependent normal mode coordinates,

$$q_\lambda(t) = \sum_{\alpha}^3 \sum_b^n \sum_l^{N_c} \sqrt{\frac{m_b}{N_c}} u_{\alpha}^{l,b}(t) e_{b,\alpha}^{\lambda*} \exp [\mathbf{i}\mathbf{k} \cdot \mathbf{r}_0^l]. \quad (1.12)$$

Here,  $u_{\alpha}^{l,b}(t)$  is the  $\alpha$  component of displacement of the  $b$ th basis atom with mass  $m_b$  in the  $l$ th unit cell from equilibrium position,  $e_{b,\alpha}^{\lambda*}$  is the complex conjugate of the eigenvector component of the phonon mode  $\lambda$ ,  $n$  is the total number of basis atoms in a unit cell, and  $N_c$  is the total number of unit cells. The total spectral energy density (SED) can be calculated for each  $\mathbf{k}$ -point from the sum of the SEDs of all phonon branches,

$$\Phi(\mathbf{k}, \omega) = \sum_{\nu}^{3n} \Phi_{\nu}(\mathbf{k}, \omega) = \sum_{\nu}^{3n} |\dot{q}_{\mathbf{k},\nu}(\omega)|^2 \quad (1.13)$$

where

$$\begin{aligned} \Phi_{\nu}(\mathbf{k}, \omega) &= |\dot{q}_{\mathbf{k},\nu}(\omega)|^2 = \left| \int_0^{\infty} \dot{q}_{\mathbf{k},\nu}(t) e^{-i\omega t} dt \right|^2 \\ &= \frac{C_{\mathbf{k},\nu}}{(\omega - \omega_{\mathbf{k},\nu}^A)^2 + \Gamma_{\mathbf{k},\nu}^2}. \end{aligned} \quad (1.14)$$

Here,  $\Phi_{\nu}(\mathbf{k}, \omega)$  is the Fourier transform of the time derivative of  $q_{\mathbf{k},\nu}(t)$  and  $C_{\mathbf{k},\nu}$  is a constant of fitting related to the normal mode vibrational amplitude  $q_{\mathbf{k},\nu,0}$ . By fitting each

of the above SED functions  $\Phi_\nu(\mathbf{k}, \omega)$  to a Lorentzian form, the mode dependent phonon relaxation time can be obtained from the full width at half maximum  $\tau_\lambda = 1/2\Gamma_{\mathbf{k},\nu}$ .

## 1.4 Machine learning methods in thermal transport

### 1.4.1 Importance of machine learning in thermal transport research

The atomistic simulations described in the previous sections provide high-fidelity calculations of thermal transport properties in bulk materials and nanostructures. These methods have proven to be extremely valuable, compared to experimental trial-and-error approaches, for guiding advanced nanomaterials development for target applications. The reasons for this are: (i) Experimental studies over the entire set of candidates can be expensive and time consuming when the design space is large. In comparison, atomistic simulations can sweep over the candidates in an inexpensive fashion and can further be validated by experimental results for the best candidates. (ii) Experiments are often not possible for certain environments, such as when the solution needs to be designed for extreme working conditions or a wide range of operating conditions, which would require a variety of sophisticated testing equipment. In such cases, simulation methods such as MD simulations can be adopted to easily handle conditions such as extremely low or high temperatures. (iii) It is challenging to obtain spectral phonon properties from experimental results, whereas the same can be easily obtained from atomistic simulations and post processing techniques. As a result, there has been a prolific use of these simulations methods in the past few decades for bypassing the experimental cost and complexity associated with screening several materials for targetted transport properties and for designing structures with extreme thermal conductivity (high or low).

With the rapid advancement of technology pushing the efficiencies of energy systems higher and higher, the design space for material science research has expanded to cover a vast array of complex materials and compounds. This has also created the requirement for predicting thermal transport properties for these materials covering a wide range of thermal conductivities (0.1 – 1000 W/mK). Figure 1.3 shows the thermal conductivities calculated for a large number of materials, using atomistic simulation techniques such as DFT and Pierls-

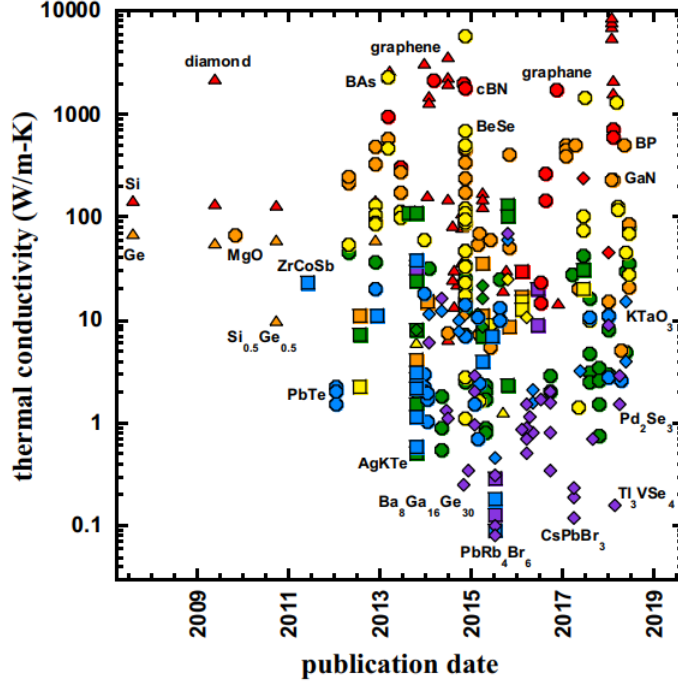


**Figure 1.3.** Thermal conductivity of various materials calculated using atomistic simulation techniques (DFT and Pierls-Boltzmann Transport equation). Reproduced from Ref. [70] with data sources compiled in the same Ref.

Boltzmann Transport equation (PBTE). However, with the need to identify newer materials and nanostructures for applications such as organic semiconductors, wearable flexible electronics and wearable thermoelectric power systems, it is becoming increasingly difficult for the thermal transport research community to keep pace with the characterization of these systems in the usual intuition-guided method. Although the challenge of experimental expense and uncertainty is avoided by using accurate simulation methods, we incur a high computational cost instead. This makes it impractical to use such methods by themselves in tasks such as high-throughput screening of a large dataset or optimization of nanostructures with several design variables.

Another failure of the traditional method of design and discovery of materials with target thermal transport properties is the inherent human bias present in the search process. Generally, exploration of the search space is guided by the previously understood knowledge of research experts in the domain. This can preclude the discovery of novel materials or structures which may display counter-intuitive thermal transport characteristics, since no

intuition is available to guide the search for these candidates. Moreover, the fact that these novel solutions are often extremely few in number within large design spaces implies that exhaustive or random searches cannot be used to efficiently identify them. As the currently known solutions are exhaustively searched, it is necessary to find these non-intuitive solutions and uncover new phonon physics governing their thermal transport.

These above considerations, along with the availability of large amounts of data of previously computed materials and structures, have led to the emergence of materials informatics and machine learning methods as a powerful method for advanced materials science research. *Materials informatics* involve applying the principles of information science to solve design problems using data, in particular by computing response surfaces, property correlations, principal component analysis etc. *Machine learning* methods use algorithms such as neural networks and Bayesian optimization that can learn feature maps between input and output data points, by learning from a training data set. In the recent decade, the availability of multi-core computer architectures capable of massively parallel computations and the commercialization of once-abstract machine learning tools have greatly accelerated the use of these methods in applications ranging from image processing and speech recognition, autonomous vehicles (or *self-driving cars*) and healthcare diagnostics. In addition, their large-scale success in these areas have led to the rise of a “machine learning” and “data-driven” paradigm in other science and engineering fields including materials research[71], [72], quantum chemistry[73], biomolecules and drug design[74], and, more recently, thermal transport research[75], [76]. In the following sections, the general framework of calculations for a few of these methods is described, along with a discussion of their application to thermal transport problems.

#### 1.4.2 Machine learning based interatomic potentials

The development of classical interatomic potentials for use in MD simulations to predict material properties including thermal transport is a complicated and time consuming task. The process usually involves representing a complex multi-dimensional potential energy surface (PES) by a simple, easy to implement analytical or tabular form. This approach,



in itself, is a major setback towards a high accuracy of the developed potential. As a result, classical interatomic potentials for materials that are often used in MD calculations of thermal transport can fail to accurately reproduce all aspects of phonon properties, even after many years of development and refinement. For example, silicon is one of the most studied materials using MD simulations, and several interatomic potential forms have been fitted to represent it, including many body potentials such as the Tersoff potential and the Stillinger-Weber potential. However, none of the developed potentials are able to accurately describe the phonon dispersion for both acoustic and optical phonon branches in the different high symmetry directions, as shown in Fig. 1.4.

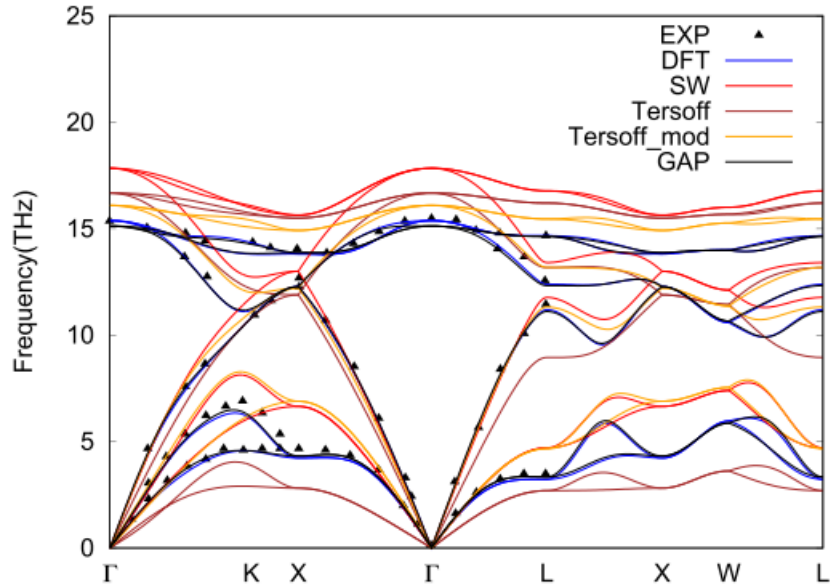


**Figure 1.4.** Phonon dispersion along high symmetry directions predicted using different interatomic potentials as well as a machine learning method (Gaussian approximation potential). Reproduced from Ref. [77]

Even if representation of the PES by an analytical form is possible with a relatively high degree of accuracy, the process is usually extremely time consuming with the most expensive part being the formation of a representative PES. This implies that in order for the potential parameters to be able to predict thermal transport properties, the PES must sample the lattice anharmonicity comprehensively by capturing configurations far from the equilibrium structure. This is not a trivial task and only by a lengthy iterative approach

can one arrive at a set of parameters which are able to represent the phonon properties with acceptable accuracy.

The above challenges can be mitigated with the use of machine learning interatomic potentials (MLIPs). The advantage of MLIPs is that a high-dimensional PES can be represented without employing simple parametric functional forms. Instead, a matrix of weights is used to form a map from input configurations to their output energies, and these weights are trained using the data points in the PES. A variety of approaches can be employed to form this map, with the Gaussian approximation potential (GAP) approach being the most commonly used[78], [79]. Another benefit of using these non-parameteric models is that atomic environments can now be represented by a vector of descriptors rather than a list of all pairwise distances, angles and dihedrals. This allows a set of  $3N$  dimensional coordinates, where  $N$  is the number of atoms in the system, to be represented by a smaller set of description vectors using the translational and rotational symmetries available. Since the description of physics is not limited by the choice of analytical form, these potentials can often provide better description of derived properties such as phonon dispersion, as shown in Fig. 1.4 for a GAP potential fitted to Si [77]. Such types of machine learning potentials have been investigated for representing specific properties of materials in a single phase[77], [80], as well as building a general purpose potential for simulating multiple properties over different phases of the material[81], [82]. Moreover, fitting of interatomic potentials has been performed using neural networks[80], [81] with the benefit of being able to describe the high-dimensional PES using the inherent non-linearity in the neural network architecture. Although the improvement in predicting properties such as phonon dispersion and phase changes has been shown over conventional analytical potential forms, these are still difficult to implement in current atomistic simulation frameworks such as MD. A review of the progress in machine learning based interatomic potential development and the degree of success achieved by applying these potentials in complex environments can be found in Ref. [79].

### 1.4.3 Neural network prediction of thermal transport properties

Neural networks (NNs) are one of the most popular class of machine learning methods used today, even surpassing human performance in a range of tasks such as image classification, healthcare diagnostics and more famously, strategy board games such as chess and Go [83]. One of the advantages of neural network based learning approaches is the freedom of NNs to generate their own feature mappings, without the need for encoding rules or enforcing restrictions on variables. Rather, the accuracy of a neural network to predict the output for a given input depends on the quality of the dataset provided to it for learning and the subsequent fitting accuracy achieved. This allows NNs to learn and reproduce non-linear complex relationships from the input data, which can be expected to be immensely helpful in the case of predicting transport phenomena. Neural networks are also able to generalize after learning, which means that they can infer unknown relationships between input and output data, which are often invisible to human observation. As a result, the feature maps created after the fitting process can be closely inspected using available post-processing *interpretability tools* to uncover property relations and governing physics that were previously unknown.

Neural networks are composed of individual compute units called neurons, which are inspired from the biological neurons in the human brain. Each neuron in an NN is connected to other neurons through a matrix of weights. The network consists of an input layer into which the input descriptors are fed in, generally one or more hidden layers of computing neurons, and an output layer. The architecture of a simple neural network is shown in Fig. 1.5. The input values pass are multiplied by the weights of the connections as they pass through the hidden layers, until the final output layer is reached. Since this represents a simple linear transformation, non-linearity is generally added at each neuron through the use of an activation function which may be sigmoidal or a rectified linear unit (ReLU).

Neural networks have been used in several applications in the thermal transport community. For example, simple neural network architectures have been employed to learn and predict the thermal boundary conductance between 2-dimensional materials such as graphene and hexagonal boron nitride, with accuracies exceeding other machine learning methods such

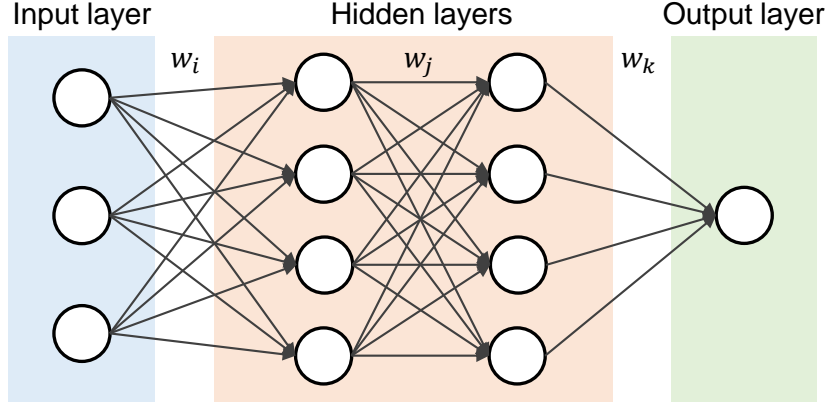


**Figure 1.5.** Schematic of a fully-connected neural network showing one input layer, two hidden layers and an output layer

as random forest search and polynomial regression [84]. A class of neural networks called convolutional neural networks (CNNs) which are suited for image processing tasks have also been used to predict the thermal conductivity of composite materials and porous media from input images of the cross sections[85]. The success of applying NNs in these tasks pave the way forward for large-scale integration of such machine learning techniques in the search for novel materials for thermal transport applications.

#### 1.4.4 Metaheuristic methods for nanostructure design optimization

In addition to predicting properties of bulk materials using simulations and machine learning methods, metaheuristics and machine learning methods have been successfully used in design optimization problems to obtain nanostructures with extreme thermal properties. *Metaheuristics* are a class of higher-level algorithms that can guide the search process of a large design space without the need for exhaustively searching the entire domain, and often incorporate a form of informed stochastic sampling. When coupled with a suitable simulation methodology such as MD simulations or Monte Carlo calculations, they can converge towards the optimal solution within a far fewer number of simulation runs than in an exhaustive or random search. More interestingly, such methods have shown to successfully guide a search towards solutions with properties contrary to the accepted knowledge[86].

A *genetic algorithm* (GA) is an evolutionary algorithm which mimics the principle of natural selection to search from the optimal candidate. With an initially random population sampled from the design space, the GA performs an iterative search process with each iteration first comprising a calculation step. In this step, the fitness values of all the candidates is evaluated with respect to the objective function defined for the problem, using an appropriate calculation framework such as MD simulations. Based on this fitness value, the population to be tested in the next generation is formed by selecting only the best candidates, thus forming the natural selection step. Finally, to sample new candidates in the design space, these selected solutions are passed through genetic operators, namely crossover and mutation, which can partially alter the characteristics of the candidates to provide potentially better solutions. The new population is again iterated upon and tested for convergence according to the design criteria. In addition to genetic algorithms, other metaheuristics that perform informed searches using similar iterative methods are simulated annealing and particle swarm optimization.

An important challenge in the realm of applying machine learning methods to some material science problems is that of insufficient training data. This is particularly true for design optimization problems where a large number of simulation results for the unique system is required, which is not available elsewhere. Even with the capability of parallel computing platforms to perform tens or hundreds of simulation runs, the size of the training dataset is generally not large by data science standards. In such cases, machine learning methods such as *Bayesian optimization* (BO) are suitable to work with. A BO creates a surrogate of the objective function and quantifies the uncertainty in that surrogate with respect to the evaluated data points using Gaussian process regression. This surrogate can then be queried using an acquisition function to find the next set of samples to evaluate in order to further minimize the prediction error, and the process can be iterated until the solution with target property can be predicted with an acceptable level of accuracy. Such techniques have been recently applied to design nanostructures with optimized phonon transport properties such as thermal conductivity and interface conductance [87]–[89].

## 1.5 Objectives and organization of this thesis

The objective of this thesis is to develop and expand the understanding of phonon and photon transport physics in nanostructured solids, using high-fidelity atomistic simulations for predicting thermal transport properties and machine learning-based methods. Along with developing general frameworks for accelerated optimization of nanostructure design using datasets generated from atomistic simulations, the optimal and suboptimal structures are closely studied to uncover the non-intuitive physical origins of the extreme thermal properties. This thesis is organized as follows.

Chapters 2 and 3 describe thermal transport calculations performed using MD simulations for a very important pair of thermoelectric materials, the binary compounds  $\text{Bi}_2\text{Te}_3$  and  $\text{Sb}_2\text{Te}_3$ . In Chapter 2, we develop two-body classical interatomic potential parameters in the Morse analytical form for bulk  $\text{Sb}_2\text{Te}_3$  tuned to predict thermal conductivity[90]. The parameters are fitted to an *ab-initio* generated potential energy surface along with lattice constants, elastic properties, phonon dispersion and density of states. The PES is built using density functional theory calculations to calculate the total lattice energies of various lattice configurations with the atoms incrementally displaced from their equilibrium positions. Once the potential parameters are developed and validated, they are used in EMD simulations to calculate the bulk thermal conductivity of  $\text{Sb}_2\text{Te}_3$  at various temperatures. The spectral accumulation of thermal conductivity is also obtained from a spectral energy density analysis to obtain the mean free path distribution of thermal conductivity.

In Chapter 3, the previously developed potentials for  $\text{Sb}_2\text{Te}_3$  along with similar a potential form for  $\text{Bi}_2\text{Te}_3$  are used in NEMD simulations to calculate thermal transport across a  $\text{Bi}_2\text{Te}_3$ - $\text{Sb}_2\text{Te}_3$  interface[91]. In addition, the spectral phonon transmission coefficients are calculated using the diffuse mismatch model and used in the Landauer transport formalism to calculate the interfacial resistance. A comparison between the resistances calculated from the Landauer formalism and those using NEMD simulations provides insight into the contribution of inelastic scattering processes in the efficient transfer of heat across the highly matched interface. Subsequently, the thermal conductivities of 1-D  $\text{Bi}_2\text{Te}_3$ - $\text{Sb}_2\text{Te}_3$  binary superlattice (SL) structures of varying superlattice period are calculated using NEMD simu-

lations. The results show a characteristic minimum thermal conductivity as the SL period is varied, in good agreement with experimental results. This is attributed to the competition between transport regimes dominated by incoherent and coherent phonon scattering at large periods and short periods respectively. Our results provide the first quantitative validation of such systems and pave the way for further optimization of thermal properties for use in thermoelectric devices.

In Chapters 4 and 5, we develop general purpose machine learning based approaches for accelerated prediction of nanostructure transport properties and efficient identification of nanostructures with target properties. In Chapter 4, a machine learning driven solution approach is proposed for the task of identifying Si-Ge random multilayer (RML) nanostructures with ultra-low thermal conductivity[62]. NEMD simulations of thermal transport are used as the predictor to evaluate candidate structures with respect to the objective function. Given the failure of an intuition-driven search due to a prohibitively large design space, we employ a genetic algorithm (GA) search process, which uses the operations of selection, crossover and mutation to efficiently predict potentially optimal solutions. Our results show that the GA is able to identify ultra-low thermal conductivity RML structures by exploring a fraction of the design space. Moreover, by comparing characteristics of the optimal and sub-optimal structures, we uncover the non-intuitive trends of thermal conductivity with respect to structural features such as average period and degree of randomness. This shows the importance of machine learning methods in the discovery of novel phonon transport physics, which can then be used to guide an informed design of nanostructures for target applications.

In Chapter 5, we further explore the accepted theory of randomness in SL period thicknesses leading to a reduction in thermal conductivity due to Anderson localization of coherent phonon modes[92]. In particular, we ask the question: does any manner of randomization of the layer thicknesses lead to a thermal conductivity reduction, or can a reverse effect, i.e. enhancement of thermal conductivity take place as well? Such a question has never been explored or answered because sufficient evidence has never been found in manual intuition-driven search results. To uncover the answer to this, we use a convolutional neural network (CNN) based prediction method for RML thermal conductivity in order to rapidly screen the

design space of all RMLs with the same mass ration and average interface density as a SL. Using an iterative methodology to ensure that the generated training set contains features characteristic of thermal transport, we are able to show the success of our CNN in predicting the thermal conductivity of RMLs with a high level of accuracy. Due to the extremely short computation time required by the CNN, we demonstrate the successfully identification of extremely low-probability-of-occurrence RMLs with higher thermal conductivity than the corresponding SL.

In Chapter 6, we demonstrate the use of a similar machine learning based optimization process for identifying multilayered photonic nanostructures with high reflectivity for applications as thermal barrier coatings. Here, we study  $\text{CeO}_2\text{-MgO}$  multilayered structures with varying total thicknesses ( $1 - 50\mu\text{m}$ ) and average layer thicknesses. Our results for spectral reflectivity in periodic superlattices of these materials show a photonic stopband, which can be manipulated by varying the average layer thickness to obtain a maximum reflectivity of the superlattice system. The addition of randomness to individual layer thicknesses is found to further enhance the spectral reflectivity due to the effect of photon localization. We employ a GA search process which is able to identify RML structures with the highest reflectivity at a given total thickness. Our results show that photon localization in certain layer thickness distributions can preferentially lower transmissivity at wavelengths corresponding to the peak intensity of the provided irradiation (calculated here for a blackbody irradiation spectrum at  $T = 1500K$ ), which leads to a high total reflectivity of the GA-optimized structures.

Chapter 7 provides a summary of the thesis and the scope of future work.



## 2. DEVELOPMENT OF INTERATOMIC POTENTIALS AND PREDICTION OF THERMAL TRANSPORT IN BULK $\text{Sb}_2\text{Te}_3$

Experimental discovery of novel materials for various applications needs to be complemented by high-throughput computer simulations of material properties. Due to the availability of modern computer architecture and massively parallel systems, atomic level methods such as *ab initio* calculations and molecular dynamics (MD) simulations enable us to efficiently predict properties over a variety of system sizes and time scales. In particular, MD simulation has emerged as a powerful tool to predict properties of both bulk materials and nanostructures, due to its capability of simulating large systems ( $\sim 1$  million atoms) for as long as several hundred nanoseconds. Another advantage of MD simulations is that it does not require any fitting parameters as inputs, except suitable interatomic potential parameters to describe the force field.

The development of an appropriate interatomic potential form for a material is a challenging task which involves approximating a complex many-body potential function with generally a simple two-body or three-body form. Although interatomic potentials have been developed for many elemental materials and simple compounds,[\[93\]](#) a significant lack of suitable potential parameters is observed for compounds with complicated crystal structures that can have important applications such as in thermoelectric power generation and photovoltaics. For example,  $\text{Bi}_2\text{Te}_3$  and  $\text{Sb}_2\text{Te}_3$  have been known to exhibit the best bulk thermoelectric properties for more than 50 years; yet interatomic potentials for  $\text{Bi}_2\text{Te}_3$  have only been developed recently[\[94\]](#), [\[95\]](#) and are still absent in literature for  $\text{Sb}_2\text{Te}_3$ . Breakthroughs in nanotechnology have enabled experimental demonstrations of even higher thermoelectric performance in  $\text{Bi}_2\text{Te}_3/\text{Sb}_2\text{Te}_3$  nanostructures.[\[14\]](#), [\[16\]](#), [\[96\]](#)–[\[104\]](#) However, computational studies on such systems are few due to absence of developed potential parameters to describe these materials. The presence of van der Waal’s interaction and polarization of charges in these compounds makes it even more difficult to develop simple and transferable potential parameters for them.

Traditionally, interatomic potentials are developed by fitting a chosen functional form to reproduce available data for a material. The data used in fitting can be obtained from

experimental measurements of bulk crystal properties like lattice constants, bond energies, and elastic and bulk moduli. Such experimental data are generally obtained for the equilibrium state of a material where the atomic interactions are harmonic in nature. However, to accurately predict anharmonic phonon-phonon scattering and heat transfer processes, the interatomic potential must be able to reproduce the anharmonicity in bonds at configurations far from the equilibrium state. Hence, most of these potentials are appropriate for the prediction of mechanical properties while not being suited for predicting thermal transport properties. An alternative to using experimental data in the potential fitting process is to generate the required data from *ab initio* calculations. The advantage of this method is that it provides the capability to sample both equilibrium and non-equilibrium states with appropriate weighting parameters chosen according to the purpose of potential development. As a result, these potentials can accurately predict anharmonic vibrational properties such as thermal conductivity. Using this method, Huang and Kaviani developed a three-body potential for bulk  $\text{Bi}_2\text{Te}_3$  and used it in equilibrium MD simulations to predict the phonon thermal conductivity,[94] while Qiu and Ruan developed a simpler two-body Morse potential for bulk  $\text{Bi}_2\text{Te}_3$ . [95] The predicted lattice thermal conductivity of the bulk crystal agrees very well with experimental data for both the potentials. As a result, these parameters have been used extensively to study the thermal properties of bulk  $\text{Bi}_2\text{Te}_3$ , [94], [95], [105] thin films [106]–[109] and nanowires. [110], [111] Katcho *et al.* [112] calculated the phonon modes of a  $(\text{Bi}_{1-x}\text{Sb}_x)_2\text{Te}_3$  alloy for any composition  $x$  by using Qiu and Ruan’s  $\text{Bi}_2\text{Te}_3$  potential for  $\text{Sb}_2\text{Te}_3$  with rescaled force constants. The rescaling factor was obtained by fitting to the experimental phonon density of states (PDOS) for bulk  $(\text{Bi}_{1-x}\text{Sb}_x)_2\text{Te}_3$ . However, the bond lengths in bulk  $\text{Sb}_2\text{Te}_3$  are different from that of  $\text{Bi}_2\text{Te}_3$ , and using the same potential parameters for both would result in a strained  $\text{Sb}_2\text{Te}_3$  lattice. More recently, Rohskopf *et al.* [113] used a genetic algorithm based optimization method to fit a combination of different functional forms of interatomic potentials for Si and Ge. Such modified potentials have been shown to predict the phonon properties well for Si and Ge. Developing simple and accurate potentials for phonon thermal transport in complex compounds is still challenging and an issue of current interest.

In this work, we describe the procedure of developing a simple two-body Morse potential for the complex binary compound  $\text{Sb}_2\text{Te}_3$  bulk crystal from *ab initio* calculations, and then predict the phonon thermal conductivity using these potential parameters in MD simulations. First, we perform density-functional theory (DFT) calculations to obtain the ground-state energies of a large number of atomic configurations of the lattice. The interatomic potential parameters are then fitted to this energy surface along with suitable experimental data such as lattice constants and bulk modulus. The obtained potential parameters are validated using lattice-dynamics calculations by reproducing the bulk crystal structure and harmonic properties. Equilibrium MD simulations are then performed using the Green-Kubo method to predict the lattice thermal conductivity over a temperature range of 200-500K. Frequency domain normal mode analysis is also used to compute the phonon modal relaxation times and the thermal conductivity accumulation with respect to phonon mean free path.

## 2.1 Electronic structure and phonon dispersion

Bulk  $\text{Sb}_2\text{Te}_3$  has a tetradymite structure and belongs to the  $D_{3d}^5 (R\bar{3}m)$  space group. The atoms are arranged along the trigonal axis in a quintuple layered structure in the order of Te1-Sb-Te2-Sb-Te1 (Fig. 2.1). The crystal can be described by the primitive rhombohedral unit cell consisting of five atoms. The corresponding lattice parameters are  $a_R = 10.447$  Å,  $\theta_R = 23.55^\circ$  with the Sb and Te1 atoms located at  $(\pm u, \pm u, \pm u)$  and  $(\pm v, \pm v, \pm v)$  respectively, where  $u = 0.3988$  and  $v = 0.2128$ .<sup>[114]</sup> The more convenient representation is the hexagonal conventional cell (Fig. 2.1) with lattice parameters  $a = 4.264$  Å and  $c = 30.458$  Å. To compute the electronic structure of the bulk crystal, we perform *ab initio* calculations based on the Density Functional Theory (DFT) framework, using the Projector-Augmented Wave (PAW) method as implemented in the Vienna *ab-initio* simulator package (VASP). Electron exchange and correlation is treated using the generalized gradient approximation (GGA) and the effect of spin-orbital coupling is included which is necessary to accurately describe heavier elements such as Sb and Te. The cutoff for the plane wave basis set and the density of the  $k$ -point grid in the Brillouin zone are chosen as 500 eV and  $8 \times 8 \times 8$  respectively according to convergence tests. To preserve the layered structure of  $\text{Sb}_2\text{Te}_3$  in

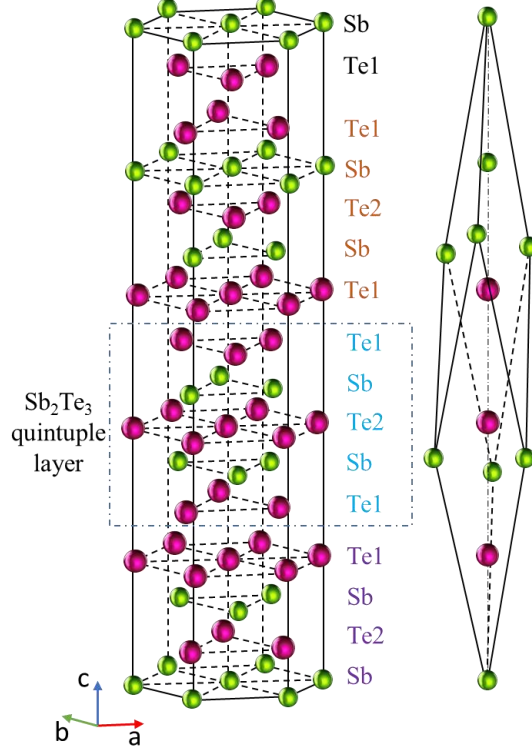


**Figure 2.1.** Quintuple-layered crystal structure of  $\text{Sb}_2\text{Te}_3$  showing rhombohedral (right) and hexagonal (left) unit cells

which the quintuple layers are held together by weak van der Waals forces of attraction, we also include the DFT-D2 correction method of Grimme.[115] We find, in accordance with previous reports,[116] that the vdW correction can better reproduce the experimental unit cell parameters. The fully relaxed rhombohedral primitive cell parameters are obtained as  $a_R = 10.597 \text{ \AA}$ ,  $\theta_R = 23.12^\circ$  with the atomic positions at  $u = 0.39712$  and  $v = 0.21370$ , which is in good agreement with previous studies using the DFT-D2 correction.[117], [118] The calculated electronic band structure along some high symmetry directions is shown in Figure 2.2. Due to the inclusion of spin-orbit coupling, a multi-valley band structure is observed which agrees well with previous studies in literature.[119]

To study the phonon properties of bulk  $\text{Sb}_2\text{Te}_3$ , we use the method of finite displacements to calculate the forces and force constants using the PHONOPY code[120] coupled with VASP as the calculator. Forces are calculated on each inequivalent atom in the rhombohedral unit cell to generate the force constants and a  $3 \times 3 \times 3$  supercell is used. Spin-orbital

coupling is not included in these calculations since previous reports suggest that the vibrational properties of  $\text{Sb}_2\text{Te}_3$  are not affected significantly by the inclusion of spin-orbital coupling.[121] The obtained phonon density of states (PDOS) is plotted in Figure 2.3 and compared to experimental results from inelastic neutron scattering.[122] As seen in the figure, the *ab initio* calculations can successfully reproduce the position and relative strength of the peaks and the overall cutoff range of frequencies with respect to the experimental measurements. The  $A_{1g}$  phonon mode calculated at the Gamma point showed a frequency of 2.15 THz which is very close to the experimental value of 2.07 THz.[123] Since our calculation of the ground state configuration including the vibrational properties are accurate and consistent previous reports, it is used to generate the *ab initio* energy surface data for parametrizing the classical interatomic potentials optimized for phonon transport properties.

Once the equilibrium lattice structure is obtained, the different configurations for the *ab initio* energy surface are generated by following a systematic approach: 1) varying the internal atomic coordinates at the equilibrium lattice constant, 2) varying the lattice constant while keeping the internal atomic coordinates (symmetry) fixed, and 3) varying the internal atomic coordinates at different lattice constants. Figure 2.4 shows a schematic for generating the energy surface in this manner using these distorted lattice configurations. Several interatomic potentials have been developed in literature by considering very small atomic

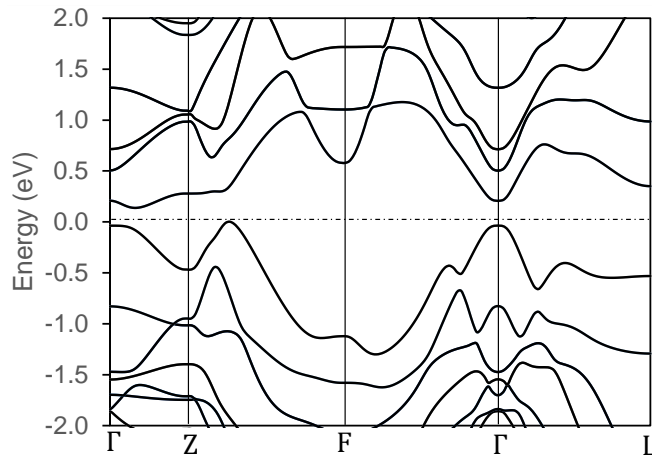


**Figure 2.2.** Electronic band structure of  $\text{Sb}_2\text{Te}_3$  along some high symmetry directions computed using DFT

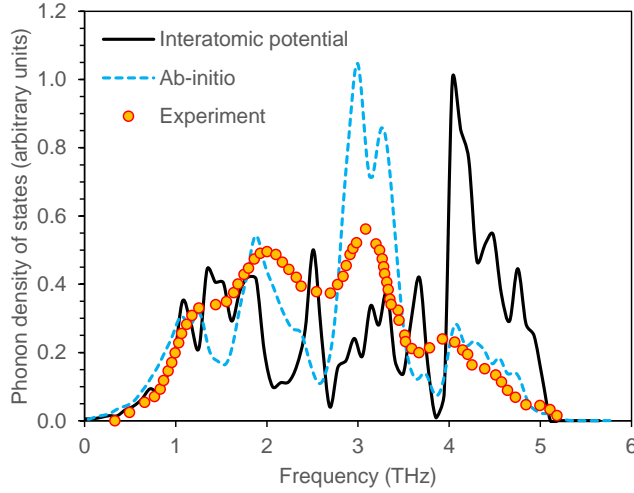


**Figure 2.3.** Phonon density of states of  $\text{Sb}_2\text{Te}_3$  computed from fitted interatomic potential parameters (solid line), *ab initio* calculations (dashed line) and experimental values from [122] (circles)

displacements from equilibrium, which can represent only the harmonic characteristics of interactions between atoms. Since our aim is to fit potential parameters which can accurately predict thermal conductivity, it is important to consider displacements that can represent the anharmonicity of pairwise interactions in our temperature of interest. To achieve this, the largest displacements from equilibrium positions given to the atoms are around  $0.35 \text{ \AA}$ . This is estimated from the characteristic thermal energy  $k_B T$  at 300K and displacements of this scale are expected to sample the anharmonicity comprehensively. We have also performed *ab initio* molecular dynamics (AIMD) simulations at 300K to verify from the trajectories that the atomic displacements are in the same range. As a result, this magnitude of displacement given is sufficient to represent the anharmonic nature of the solid around our temperature of interest. For better performance of the gradient-based fitting process, we artificially build the configurations using these displacements to maintain as much symmetry of the lattice as possible which helps in convergence of the fitting runs.

Apart from varying the internal atomic coordinates, the lattice constant is varied within 1.4% of the equilibrium value, and the atomic positions are varied at different lattice constants. The inclusion of such configurations in the energy surface is necessary to capture the temperature-dependent phonon properties due to thermal expansion. Also, since the bulk

modulus is computed from the variation of energy with respect to the volume of the unit cell, the inclusion of these configurations ensure that the fitted parameters are able to reproduce the equilibrium lattice constant and the bulk modulus. Besides fitting to the energy surface, Rohskopf *et al.*[113] proposed fitting to the forces on each atom and the harmonic and 3rd order interatomic force constants calculated from *ab initio* methods. Forces and force constants are first order and higher order derivatives of the energy surface ( $\frac{\partial E}{\partial r_i}$ ,  $\frac{\partial^2 E}{\partial r_i \partial r_j}$ ,  $\frac{\partial^3 E}{\partial r_i \partial r_j \partial r_k} \dots$ ) respectively. These are calculated using the method of finite differences from the energy surface data points near the equilibrium configuration. As a result, using force constants should be equivalent to our method of fitting to only the energy surface data, provided the same number of energy surface data points near the equilibrium is used. To generate data points representative of interatomic force constant calculations, we use the open source software ALAMODE[124] to obtain configurations which would be used in force constants

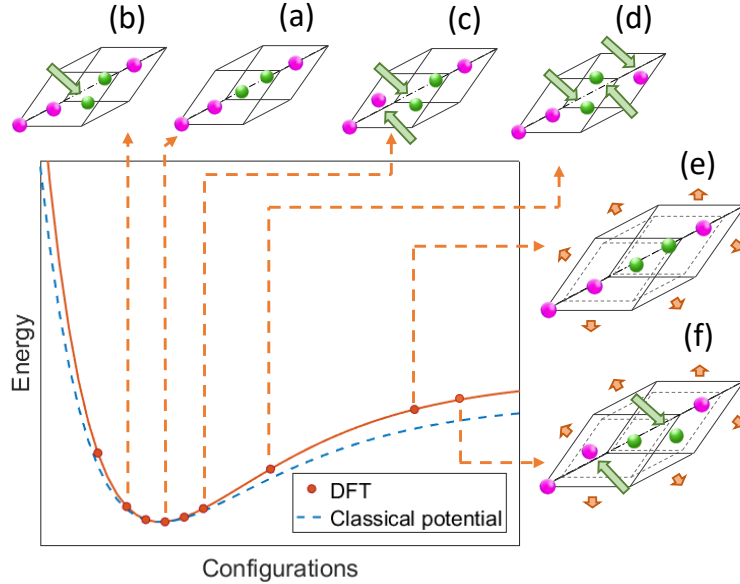


**Figure 2.4.** Schematic showing the generation of the *ab initio* energy surface. The circles represent different configurations used in the energy surface such as the equilibrium configuration (a), displacements of atom(s) at fixed lattice constant (b,c and d), variation of lattice constant with atoms fixed at equilibrium positions (e) and displacement of atom(s) at varied lattice constant (f) . The dashed line represents the classical interatomic potential fitted to the energy surface

calculations, and include these configurations in our *ab initio* energy surface. The total number of configurations we use in fitting are 108, out of which 60 configurations represent variation of internal atomic coordinates at the equilibrium lattice constant, 14 configurations represent variation of the lattice constant with fixed atomic fractional coordinates, 19 configurations represent variation of atomic fractional coordinates at a varied lattice constant, and 15 configurations are made to be representative of force constant calculations.

Above, we have described a hierarchical process of including different configurations at different stages of fitting till the thermal conductivity can be reproduced well. We shall note that currently the methodology does not work in the perfect manner that the fitting converges smoothly as more configurations are added. Due to the complicated nature of the fitting process involving 21 variables, we find that simply adding more configurations to the energy surface does not always generate a better fit. On the contrary, addition of specific structures to the fitting dataset sometimes causes the fitting process to diverge, and the relative weights of these configurations in the objective function may need to be adjusted carefully to prevent this from happening. Often, some older configurations need to be removed when new configurations are added. Another reason that inclusion of more configurations does not always ensure better potential parameters is that the *ab initio* results do not exactly match with the experimental data that are also included as fitting targets. As a result, there needs to be a balance between the number of *ab initio* configurations used and the experimental data included, so that the fitted potential parameters can reproduce both types of observables with good accuracy. Finally, the potential parameters will depend on the purpose the potential is used for and are not unique. For mechanical properties, often only the near-equilibrium configurations need to be considered; for thermal conductivity, anharmonic configurations away from the equilibrium need to receive considerable weight; while for chemical reactions, configurations far away from the equilibrium and near bond-breaking need to be included. This will impact the final fitted parameters since there is no unique way to choose the weighting factors.



## 2.2 Classical interatomic potential parameters

Interatomic potentials which can accurately reproduce the quantities of interest are the primary requisite for performing meaningful MD simulations. For complex materials, the choice of the potential functional form is also very important. Many-body potentials may be able to provide a more accurate description of a material along a wider range of simulation conditions, but they involve several parameters and are not very accessible due to their complex forms. On the other hand, most two-body potential forms are simple to implement, computationally less expensive and can reproduce material properties with good accuracy. For example, the potential parameters developed by Qiu and Ruan for  $\text{Bi}_2\text{Te}_3$  have a simple two-body form which ensures better accessibility, while being able to predict phonon anharmonicity and thermal conductivity very well among other properties.[95] Since no potential parameters exist in literature yet for  $\text{Sb}_2\text{Te}_3$ , we choose to develop two-body interatomic potential parameters which can suitably describe its phonon transport properties.

We use a two-body potential form  $\varphi(r_{ij})$  between atoms  $i$  and  $j$  composed of a short-range interaction term  $\varphi_s(r_{ij})$  and a long-range Coulombic term which can be written as

$$\varphi(r_{ij}) = \varphi_s(r_{ij}) + \frac{q_i q_j}{r_{ij}} \quad (2.1)$$

where  $r_{ij}$  is the distance between the atoms  $i$  and  $j$ .  $q_i$  and  $q_j$  are the partial charges on the atoms, which are more appropriate to use for solids like  $\text{Bi}_2\text{Te}_3$  and  $\text{Sb}_2\text{Te}_3$  that have a partially covalent nature. The partial charges used in the potential parameters are 0.30, -0.22 and -0.16 for Sb, Te1 and Te2 atoms respectively, which were obtained by allowing the charges to vary during the potential fitting process. In this work, we use a rigid ion model to fit the atomic charges. Alternatively, a core-shell model might be used to better reproduce the polarization in Sb and Te atoms. However, the increased number of fitting parameters incurred due to this approach makes it very difficult to obtain converged parameters during the parametrization process. The short-range interaction is modeled using the Morse

potential form, which is suitable to describe the vibrational properties of solids including anharmonicity. The functional form is given by

$$\varphi_s(r_{ij}) = D_e[\{1 - e^{(-a(r_{ij}-r_o))}\}^2 - 1] \quad (2.2)$$

Here,  $D_e$  is the depth of the potential well (bond strength),  $a$  is a measure of the width of the well (bond rigidity), and  $r_o$  is the location of the potential well minimum which corresponds to the bond length. As in the case of the two-body potential development of  $\text{Bi}_2\text{Te}_3$ ,<sup>[95]</sup> we consider only the nearest neighbor interactions by carefully choosing the cutoffs for different interactions. This treatment of short-range interactions has been found to be crucial for preserving the complex layered structure of the crystal. The long-range electrostatic potential is computed by the Ewald summation method with a real-space cutoff radius of 12 Å.

**Table 2.1.** Fitted short-range Morse potential parameters for  $\text{Sb}_2\text{Te}_3$ .  $D_e$  is the depth of the potential well,  $a$  is a measure of bond stiffness,  $r$  is the pairwise atomic distance and  $r_c$  is the cutoff distance

Type of interaction	$D_e$ (eV)	$a$ (1/Å)	$r_o$ (Å)	$r_c$ (Å)
Sb - Sb	0.089	2.112	4.258	5.5
Te1 - Te1	0.072	1.720	3.795	5.0
Te2 - Te2	0.066	2.639	4.261	5.0
Sb - Te1	1.008	1.292	3.018	4.0
Sb - Te2	0.538	1.166	3.172	4.0
Te1 - Te2	0.750	0.595	4.486	5.5

The potential parameters are fitted to the *ab initio* energy surface using the General Utility Lattice Program (GULP)<sup>[125]</sup> which is designed to handle multivariable optimization problems. The total number of parameters allowed to be fit during the optimization is 21, which includes 18 potential parameters for 6 different types of interactions, 2 partial charges and an energy shift to account for the difference in reference level for potential energy. The parameters obtained from the fitting process are then used to optimize the crystal structure and calculate bulk properties at the equilibrium configuration. These are compared with

experimental data and the process is iterated until the predicted results show good agreement with experimental data. The optimized potential parameters are shown in Table 2.1, along with the cutoff radii  $r_c$ . As in the Morse potential parameters for  $\text{Bi}_2\text{Te}_3$  in Ref [95], we see that the Te1-Te1 bond has a relatively weak bond energy ( $D_e$ ) along with a high bond stiffness (represented by  $a$ ), which is attributed to the fact that these parameters represent both the weak van der Waals interaction between Te1 atoms of two adjacent quintuple layers (cross-plane), as well as the covalent Te1-Te1 interaction within the same layer (in-plane). In contrast, the inter-layer (cross-plane) Sb-Te1, Sb-Te2 and Te1-Te2 bonds have a higher bond energy and larger anharmonicity which suggests the more ionic nature of these bonds. They also have lower bond stiffness due to which the material elasticity in the cross-plane direction ( $C_{33}$ ) is lower than in the in-plane direction ( $C_{11}$ ). The elastic constants and bulk modulus obtained using the fitted potential parameters are shown in Table 2.2 and compared with those obtained from our own *ab initio* calculations as well as from previous literature.[126], [127] It is apparent from these results that the phonon thermal transport in the cross-plane direction is expected to be weaker than that in the in-plane directions.

The fitted potential parameters are also used to calculate the phonon density of states by computing the dynamical matrix in GULP (Fig. 2.3). We can see that our classical interatomic potential can successfully reproduce the low frequency acoustic phonon portion

**Table 2.2.** Computation of elastic constants and bulk modulus using fitted potential parameters and comparison with *ab initio* calculations. All quantities are in Gigapascals.

Property	<i>Ab-initio</i> (this work)	<i>Ab-initio</i> <sup>1</sup>	<i>Ab-initio</i> <sup>2</sup>	Classical potential
$C_{11}$	77.5	85.5	83.2	83.8
$C_{12}$	21.9	21.0	21.2	28.1
$C_{13}$	25.5	30.8	46.1	24.7
$C_{14}$	14.3	21.1	-	9.5
$C_{33}$	46.5	50.5	99.7	49.1
$C_{44}$	27.8	37.9	44.6	20.6
$C_{66}$	27.1	-	31.0	27.9
$B$	32.7	42.1	53.2	39.9

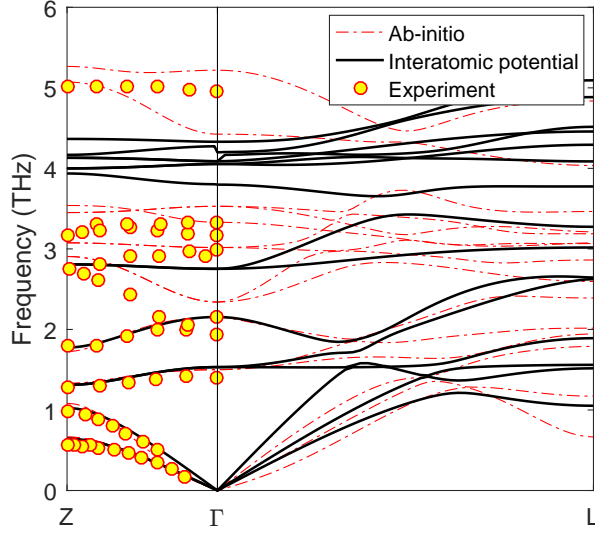


**Figure 2.5.** Phonon dispersion of  $\text{Sb}_2\text{Te}_3$  along some high-symmetry directions computed from *ab-initio* calculations (broken line), fitted interatomic potential parameters (solid line) and experimental values from Ref. [123] (circles)

of the phonon DOS compared to both *ab initio* calculations and experimental measurements in terms of the position and relative magnitude of the low-frequency peaks. In contrast, the position of the high-frequency optical peak is shifted significantly higher with respect to *ab initio* and experimental data. To further analyze the phonon properties, the phonon dispersion along high-symmetry directions is compared to *ab initio* results and inelastic neutron scattering data[123] in Figure 2.5. We can see that the acoustic phonon branches are reproduced in very good agreement with experiment, but the optical branches are overpredicted. These dissimilarities between calculation and experiment can be attributed to using a simple two-body potential form to fit the energy surface, along with the use of a rigid ion model. A more detailed core-shell charge model may be able to improve the optical phonon dispersion by accounting for the charge polarization. In spite of the limitations of our simple potential form, it is able to accurately describe the lattice structure, elastic properties and dispersion of acoustic phonons. Moreover, simulations of thermal transport in  $\text{Bi}_2\text{Te}_3$  using the Morse potential parameters showed very good agreement with experimental measurements,[95] which suggests that the contribution of optical phonons to lattice thermal conductivity is low for

these compounds. Since the thermal transport is dominated by the low-frequency acoustic phonons, we can expect that our potential parameters will be able to accurately predict the lattice thermal conductivity of  $\text{Sb}_2\text{Te}_3$ .

### 2.3 Molecular dynamics simulations of lattice thermal conductivity

We use equilibrium molecular dynamics (EMD) to predict the lattice thermal conductivity of  $\text{Sb}_2\text{Te}_3$  in the in-plane and cross-plane directions over a range of temperatures. EMD simulations use the Green-Kubo linear-response formulation[128] to predict the thermal transport properties, while the effect of system size has been found to be small due to the application of periodic boundary conditions. Under the Green-Kubo formalism, the phonon thermal conductivity of a system is given by

$$\kappa_{l,\alpha} = \frac{1}{k_B V T^2} \int_0^\infty \langle S_\alpha(0) \cdot S_\alpha(t) \rangle dt, \alpha = x, y, z \quad (2.3)$$

Here,  $V$  is the volume of the simulation cell,  $T$  is the absolute temperature in Kelvin,  $S_\alpha(t)$  is the heat current along a particular direction and  $\langle S_\alpha(0) \cdot S_\alpha(t) \rangle$  represents the heat current autocorrelation function (HCACF). For a pair potential, the heat current is commonly written as

$$\mathbf{S} = \sum_i \mathbf{e}_i \mathbf{v}_i + \frac{1}{2} \sum_{i,j} (\mathbf{F}_{ij} \cdot \mathbf{v}_i) \mathbf{r}_{ij} \quad (2.4)$$

where  $\mathbf{e}_i$  is the energy and  $\mathbf{v}_i$  is the velocity of particle  $i$ , and  $\mathbf{F}_{ij}$  is the force acting between particles  $i$  and  $j$  separated by  $\mathbf{r}_{ij}$ . The integral in Equation 2.3 is in practice carried out over a finite time interval which needs to be decided appropriately based on the longest phonon lifetimes existing in the material.

We performed MD simulations of bulk  $\text{Sb}_2\text{Te}_3$  on a system consisting of  $6 \times 6 \times 2$  hexagonal unit cells with a total of 1080 atoms. Convergence tests with larger system sizes show negligible size effects. The equations of motion are integrated using the Verlet algorithm with a time-step of 0.25 fs, which is sufficient to resolve the highest frequency phonon mode calculated from lattice dynamics, while the Nose-Hoover thermostat is used to regulate system

temperature. Initially, the bulk lattice structure is equilibrated under an NPT ensemble for 250 ps to minimize the stress on the system, after which it is switched to an NVE ensemble and run for another 250 ps to observe conservation of energy. Following this step, the heat current data is obtained for 20 ns to compute the HCACF, with a sampling interval of 10 timesteps. MD simulations are performed over a temperature range of 200K to 500K with an interval of 50K.

To minimize statistical fluctuations, we perform runs for 10 independent ensembles at every temperature. The uncertainty associated with calculation of thermal conductivity from equilibrium MD simulations has recently been quantified by Wang *et al.*[129] who correlated the standard deviation  $\sigma_\kappa$  of the predicted thermal conductivity about the average  $\kappa_{ave}$ , with the total simulation time  $t_{total}$ , HCACF correlation time length  $t_{corr}$  and number of independent runs  $N$  as

$$\frac{\sigma_\kappa}{\kappa_{ave}} = 2 \left( \frac{N \times t_{total}}{t_{corr}} \right)^{-0.5} \quad (2.5)$$

Based on their suggestion, we compared the thermal conductivity from MD simulations performed for the system at 300K with a total time of 2 ns and 20 ns and a fixed correlation time of 125 ps. Our results indeed show that the spread in thermal conductivity values from different runs reduces significantly with increasing total simulation time, which is expected since time averaging in MD simulations is equivalent to ensemble averaging.

The variation of lattice thermal conductivity  $\kappa_l$  in both in-plane and cross-plane directions with temperature is shown in Figure 2.6 along with the  $1/T$  fitting. The error bars for each data point have been obtained using Equation 2.5. Both the in-plane and the cross-plane thermal conductivities generally follow a  $1/T$  curve which indicates the dominance of Umklapp scattering. Experimental measurements of thermal conductivity of bulk  $\text{Sb}_2\text{Te}_3$  in literature have large discrepancies among themselves. This may be due to the fact that the values reported often do not separate either the contributions from electronic and lattice contributions, or the in-plane and cross-plane anisotropy which is high for a layered material such as  $\text{Sb}_2\text{Te}_3$ . The reported values for total thermal conductivity vary widely from 2 - 5  $\text{Wm}^{-1}\text{K}^{-1}$ , [20], [130], [134]–[138] while the lattice thermal conductivity is gener-

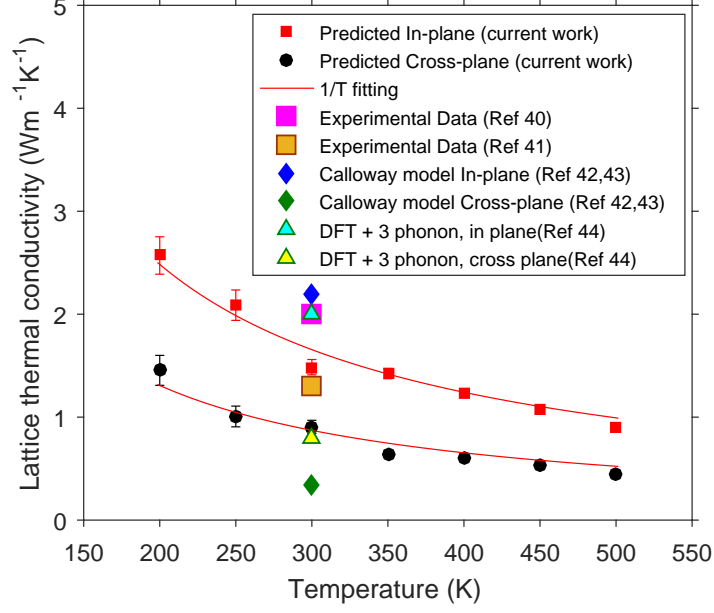


**Figure 2.6.** MD predicted thermal conductivity in in-plane and cross-plane directions and 1/T fitting compared with experimental data (Ref. [20], [130]), calculations using a modified Calloway model (Ref. [131], [132]) and BTE + 3 phonon calculations (Ref [133])

ally estimated at around  $1.3 - 2.5 \text{ Wm}^{-1}\text{K}^{-1}$ . [20], [130], [137], [138] The theoretical lattice thermal conductivity has been calculated using the modified Calloway model as  $\kappa_{\parallel} = 2.2 \text{ Wm}^{-1}\text{K}^{-1}$  and  $\kappa_{\perp} = 0.34 \text{ Wm}^{-1}\text{K}^{-1}$ . [131], [132] Campi *et al.* [133] predicted the thermal conductivity of  $\text{Sb}_2\text{Te}_3$  from first principles by solving the Boltzmann Transport Equation. The phonon-phonon scattering was derived by calculating the anharmonic force constants using the framework of Density Functional Perturbation Theory. The in-plane thermal conductivity at 300K obtained in their work is  $2.0 \text{ Wm}^{-1}\text{K}^{-1}$  which is higher than the results we observe in our calculations, while the cross-plane thermal conductivity obtained is  $0.8 \text{ Wm}^{-1}\text{K}^{-1}$  which agrees well with our results. The higher in-plane conductivity may be due to the fact that the authors in Ref. [133] have included only three-phonon scattering in their computations, while our MD treatment inherently includes higher order processes such as four-phonon scattering, which may be important. [139]–[141] Besides, the inaccuracy of the potential to reproduce the optical phonon dispersion may also contribute to the observed discrepancy.

## 2.4 Phonon modal relaxation time and thermal conductivity accumulation

We also calculate the contribution of different phonon modes to the total cross-plane lattice thermal conductivity using frequency domain normal mode analysis (FD-NMA). The total thermal conductivity can be obtained as the sum of the mode-wise thermal conductivities  $k_j$  of all phonon modes in the first Brillouin zone

$$\kappa_z = \sum_j \kappa_j = \frac{1}{(2\pi)^3} \sum_\nu \int (\mathbf{v}_\lambda \cdot \hat{z})^2 c_\lambda \tau_\lambda d\mathbf{k} \quad (2.6)$$

where,  $z$  is the cross-plane direction,  $\lambda$  represents the phonon mode  $(\mathbf{k}, \nu)$  with  $\mathbf{k}$  being the wave vector and  $\nu$  the polarization branch,  $c_\lambda$  is the phonon mode specific heat,  $\tau_\lambda$  is the relaxation time,  $\mathbf{v}_\lambda$  is the group velocity and the summation over the Brillouin zone is converted to the continuous integral form using  $\sum_k = V/(2\pi)^3 \int d\mathbf{k}$ . The specific heat per phonon mode is given by  $c_\lambda = \hbar\omega_\lambda \partial n_\lambda^0 / \partial T = k_B x^2 e^x / (e^x - 1)^2$ , where  $x = \hbar\omega / k_B T$ , and the phonon occupation number  $n_\lambda^0 = 1/(e^x - 1)$  according to the Bose-Einstein distribution. The phonon group velocity is given by the gradient of the phonon dispersion,  $v = d\omega/dk$ , where  $\omega$  is the phonon angular frequency.

The frequency domain normal mode analysis (FD-NMA) method was initially developed by Wang *et al.*[65] and later extended by Shiomi and Maruyama,[66] De Koker,[67] Thomas *et al.*[68] and Feng *et al.*[69] According to lattice dynamics, the vibrations of atoms in real space can be mapped to the time-dependent normal mode coordinates,

$$q_\lambda(t) = \sum_\alpha^3 \sum_b^n \sum_l^{N_c} \sqrt{\frac{m_b}{N_c}} u_\alpha^{l,b}(t) e_{b,\alpha}^{\lambda*} \exp[\mathbf{i}\mathbf{k} \cdot \mathbf{r}_0^l]. \quad (2.7)$$

Here,  $u_\alpha^{l,b}(t)$  is the  $\alpha$  component of displacement of the  $b$ th basis atom with mass  $m_b$  in the  $l$ th unit cell from equilibrium position,  $e_{b,\alpha}^{\lambda*}$  is the complex conjugate of the eigenvector component of the phonon mode  $\lambda$ ,  $n$  is the total number of basis atoms in a unit cell, and



$N_c$  is the total number of unit cells. In FD-NMA, the total spectral energy density (SED) is calculated for each k-point from the sum of the SED's of all phonon branches,

$$\Phi(\mathbf{k}, \omega) = \sum_{\nu}^{3n} \Phi_{\nu}(\mathbf{k}, \omega) = \sum_{\nu}^{3n} |\dot{q}_{\mathbf{k},\nu}(\omega)|^2 \quad (2.8)$$

where

$$\begin{aligned} \Phi_{\nu}(\mathbf{k}, \omega) &= |\dot{q}_{\mathbf{k},\nu}(\omega)|^2 = \left| \int_0^{\infty} \dot{q}_{\mathbf{k},\nu}(t) e^{-i\omega t} dt \right|^2 \\ &= \frac{C_{\mathbf{k},\nu}}{(\omega - \omega_{\mathbf{k},\nu}^A)^2 + \Gamma_{\mathbf{k},\nu}^2}. \end{aligned} \quad (2.9)$$

Here,  $\Phi_{\nu}(\mathbf{k}, \omega)$  is the Fourier transform of the time derivative of  $q_{\mathbf{k},\nu}(t)$  and  $C_{\mathbf{k},\nu}$  is a constant of fitting related to the normal mode vibrational amplitude  $q_{\mathbf{k},\nu,0}$ . By fitting the SED function at each k-point to  $3n$  Lorentzian forms, we can extract the anharmonic phonon frequency  $\omega$  for each phonon mode. The phonon relaxation time  $\tau_{\lambda}$  is also obtained from the full width at half maximum of the fitted curve as  $\tau_{\lambda} = 1/2\Gamma_{\mathbf{k},\nu}$ . It is to be noted here that due to the finite size and periodicity requirements of the MD domain, not all k-vectors in the Brillouin zone can be sampled. Only those k-points in the first Brillouin zone satisfying the condition  $e^{-i\mathbf{k}\cdot\mathbf{r}} = 1$  can be resolved in the MD normal mode analysis, where  $\mathbf{r} = \sum_{i=1}^3 n_i \mathbf{A}_i$  and  $\mathbf{A}_i$  is the length vector of the simulation domain in direction  $i$ .

We perform FD-NMA on a  $12 \times 12 \times 12$  rhombohedral cell with 5 basis atoms, and a  $12 \times 12 \times 12$  k-point grid uniformly sampling the first Brillouin Zone. The rhombohedral primitive cell is used since the number of phonon dispersion branches in this case is much less than that obtained using the hexagonal cell, which makes the SED analysis simpler. The system is first relaxed under an NPT ensemble at 300K for 200 ps and further under an NVE ensemble for 200 ps. Following this, the system is run in an NVE ensemble to compute the normal mode amplitudes from the MD trajectories at an interval of 10 fs, which is shorter than the shortest phonon time period. The anharmonic phonon dispersion computed from NMA along the  $\Gamma - Z$  direction is shown in Figure 2.7(a) along with the harmonic phonon dispersion computed from GULP for comparison, and also the quasi-harmonic dispersion computed with the lattice constant at 300K. It is seen that there is noticeable softening

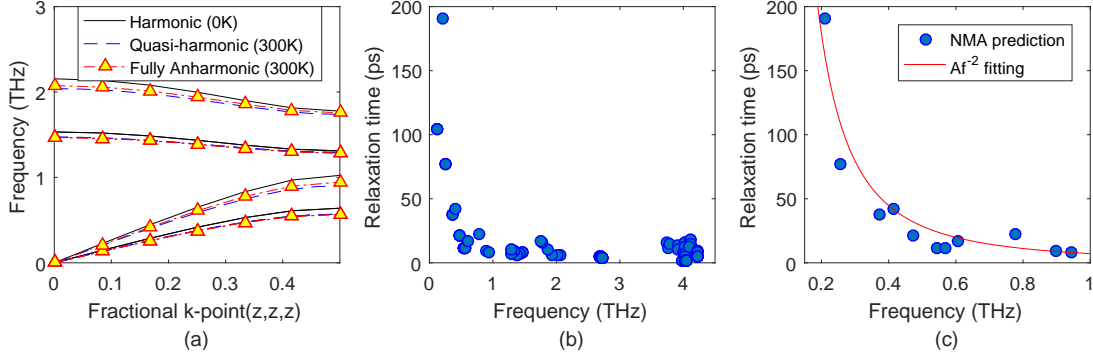


**Figure 2.7.** (a) Anharmonic phonon dispersion at 300K from NMA (triangles and broken lines), quasi-harmonic phonon dispersion (300K) from LD (dashed lines) and harmonic phonon dispersion (0K) from LD (solid lines) along the  $\Gamma - Z$  direction (b) Relaxation times of phonons along the  $\Gamma - Z$  direction (c) Relaxation times of low-frequency acoustic phonons along  $\Gamma - Z$ , along with  $f^{-2}$  fitting

of the phonon modes at finite temperature, which proves that our developed interatomic potential can capture the anharmonicity of the material. The quasi-harmonic results are very similar to the fully anharmonic results, indicating that the frequency shift is mainly due to the lattice expansion. The phonon relaxation times predicted by FD-NMA along the  $\Gamma - Z$  direction are shown in Figure 2.7(b), where it can be seen that the phonon lifetime decreases with increasing phonon frequency. The lifetimes of acoustic phonons below 1 THz are very well fitted with a  $\tau \propto f^{-2}$  form (Figure 2.7(c)), which is generally the power law expression used in many works for calculating the thermal conductivity analytically. The lifetime of the  $A_{1g}$  phonon mode is predicted by the FD-NMA to be 4.5 ps, compared to the experimental value of 3.4 ps obtained from time-resolved reflectivity measurements using femtosecond pulses.[142] The overall range of phonon lifetimes is also similar to the phonon lifetimes calculated for  $\text{Bi}_2\text{Te}_3$  using time-domain normal mode analysis (TD-NMA) by Wang *et al.*[143]

The phonon relaxation times obtained using FD-NMA and the group velocities are used in Equation 2.6 to calculate the thermal conductivity of each phonon mode as well as the total thermal conductivity. Obtaining a converged sum from Equation 2.6 requires proper discretization of the Brillouin Zone to ensure we capture all important phonon modes. Due to

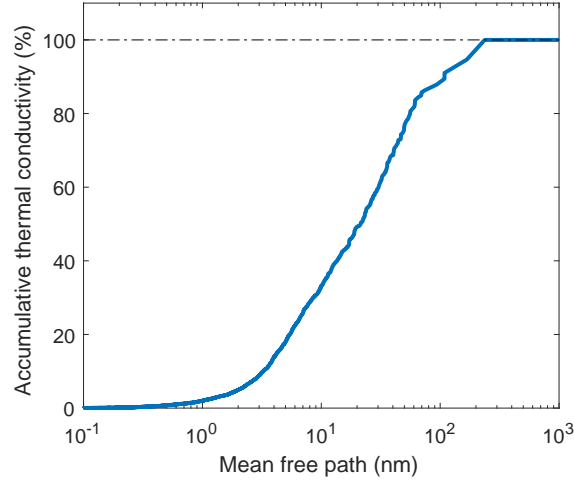


**Figure 2.8.** Accumulated thermal conductivity (%) with respect to phonon mean free path

the finite size of the MD simulation domain, the contribution of phonon modes with very long wavelengths is absent; however, the density of states for these low frequency modes is low. We have performed calculations for an  $8 \times 8 \times 8$  simulation domain with an  $8 \times 8 \times 8$  k-point grid to test the size effect. The results for phonon lifetimes and total thermal conductivity are similar to the  $12 \times 12 \times 12$  cell system, which suggests that our k-grid resolution is able to ensure a converged sum. The total cross-plane thermal conductivity obtained from FD-NMA is 0.92 W/mK, which agrees very well with the EMD value of 0.89 W/mK. The difference in the two results can be attributed to process of fitting the Lorentzian form to a large number of phonon modes, particularly for the higher frequency peaks which are often clustered together and difficult to isolate. The accumulation of thermal conductivity in the cross-plane direction with respect to phonon mean free path is shown in Figure 2.8, where the mean free paths along the cross-plane direction can also be obtained using the relation  $\lambda = (\mathbf{v} \cdot \hat{z})$ . The results in Figure 2.8 show that phonons with mean free paths between 3 and 100 nm contribute to around 80% of the total cross-plane thermal conductivity. The contribution of acoustic phonons to total thermal conductivity is 80% while the contribution of optical phonons is 20%, compared to a 35% contribution of optical phonons calculated by Campi *et al.*[133] from first principles.

## 2.5 Conclusions

In summary, we have used density functional theory to calculate the electronic band structure of bulk  $\text{Sb}_2\text{Te}_3$  and the energies of different representative configurations away from equilibrium. We then fit a two-body Morse interatomic potential form to the energy surface and experimentally observed crystal properties like lattice constants and bulk modulus. The fitted potential form can reproduce the lattice structure and acoustic phonon dispersion of the crystal in very good agreement with experiment, indicating that our developed potential is suitable to describe phonon thermal transport in the material. Molecular dynamics simulations using the Green-Kubo linear response framework have then been performed using this interatomic potential, and the lattice thermal conductivity in the in-plane and cross-plane directions have been predicted over a range of temperature from 200-500K. The in-plane thermal conductivity was found to vary from  $0.9 - 2.6 \text{ Wm}^{-1}\text{K}^{-1}$ , while the cross-plane thermal conductivity was found to vary from  $0.4 - 1.5 \text{ Wm}^{-1}\text{K}^{-1}$  as the temperature is decreased from 500 K to 200 K. The results at room temperature agree well within the range of experimental values found in literature. The nature of phonon transport in  $\text{Sb}_2\text{Te}_3$  is found to be extremely similar to that in  $\text{Bi}_2\text{Te}_3$  as expected, with the cross-plane thermal conductivity much lower than the in-plane one due to the weak nature of the van der Waal's bonds in the inter-layer direction. The modall decomposition of the cross-plane thermal conductivity is also performed using frequency domain normal mode analysis (FD-NMA). The anharmonic phonon dispersion along the  $\Gamma - Z$  cross-plane direction shows softening of phonon frequencies, while the acoustic phonons are found to be approximated well by a  $f^{-2}$  fitting. In addition to being able to predict the thermal conductivity of bulk  $\text{Sb}_2\text{Te}_3$ , this potential may be applied to the study of thermal transport in  $\text{Bi}_2\text{Te}_3$  -  $\text{Sb}_2\text{Te}_3$  alloys and nanostructures, which is the scope of future work.

### 3. THERMAL CONDUCTIVITY AND INTERFACIAL THERMAL RESISTANCE IN $\text{Bi}_2\text{Te}_3$ - $\text{Sb}_2\text{Te}_3$ MULTILAYER STRUCTURES FROM MOLECULAR DYNAMICS

Thermoelectric energy systems provide an attractive solution to convert large amounts of waste heat, such as that generated by traditional fossil fuel based energy production systems, into electrical power directly. The performance of a thermoelectric generator can be characterized by its figure of merit ( $ZT$ ), given by  $ZT = S^2\sigma T/(\kappa_e + \kappa_{ph})$ , where  $S$ ,  $\sigma$  and  $T$  are the Seebeck coefficient, electrical conductivity and temperature respectively, and  $\kappa_e$  and  $\kappa_{ph}$  are the electronic and phononic contributions to the thermal conductivity of the material. The difficulty to tune the  $ZT$  by modulating the terms in the numerator and denominator independently arises due to the coupled nature of the electrical and thermal transport properties. Bismuth telluride ( $\text{Bi}_2\text{Te}_3$ ), antimony telluride ( $\text{Sb}_2\text{Te}_3$ ) and their alloys have long been found to provide the highest figures of merit among bulk materials, due to their low lattice thermal conductivities at room temperature. In recent decades, the ability to create nanostructures comparable to phonon mean free paths has led to successful proof-of-concept demonstrations of high  $ZT$  devices based on these materials[16], [25], [144]–[153], mainly by reduction of the lattice thermal conductivity. In particular, multilayer structures such as superlattices have received widespread attention due to their ultra-low thermal conductivity caused by repeated phonon-interface scattering[16], [144], [153]–[155].

In order to expedite the search for higher efficiency systems and gain insight into the underlying transport mechanisms, such experimental demonstrations need to be complemented by computational studies of these systems. Moreover, such simulation results can also be used as the training data in informatics and machine learning methods which have become increasingly popular in performing highly accelerated design optimization of nanostructures with targeted transport properties[88], [156]–[158]. Despite the long-standing importance of  $\text{Bi}_2\text{Te}_3$ ,  $\text{Sb}_2\text{Te}_3$  and their nanostructures as thermoelectric materials, there are few modeling studies in literature to characterize thermal transport in these devices. Pattamatta and Madnia[159] studied the thermal transport in  $\text{Bi}_2\text{Te}_3$ - $\text{Sb}_2\text{Te}_3$  1-D superlattices and 2-D nanowire composites using the Boltzmann transport equation (BTE). Since only the particle nature of

phonon modes was considered within this approach, their results did not show the existence of a minimum thermal conductivity with respect to varying superlattice period, which is now widely understood to occur due to competing phonon wave effects. Katcho *et al.*[112] calculated the thermal conductivity of  $(\text{Bi}_{1-x}\text{Sb}_x)_2\text{Te}_3$  alloys with and without embedded spherical nanoparticles. Their results showed that significant reduction in thermal conductivities of the nanoparticle-alloy composites could be achieved with nanoparticle diameters less than 10 nm. Moreover, the BTE approach used in these studies required the estimation of phonon mean free paths by fitting to the bulk thermal conductivities, and cannot be considered completely predictive methods. In contrast, molecular dynamics (MD) simulations, which require no input fitting parameters except appropriate interatomic potentials, have been used to study thermal transport in bulk  $\text{Bi}_2\text{Te}_3$ [94], [95], [160] and nanostructures[111], [112], [161]–[163] with close agreement to experimental measurements. The thermal conductivity of bulk  $\text{Sb}_2\text{Te}_3$  was also calculated using MD simulations in our previous work[90]. In this work, we calculate the phonon transport properties across a  $\text{Bi}_2\text{Te}_3$ - $\text{Sb}_2\text{Te}_3$  interface and 1-D superlattices with varying periods, using non-equilibrium molecular dynamics simulations. The simulation methodology including details of the multilayer structures is described in Section 6.2. The results for thermal conductance at the single interface and thermal conductivity of the superlattices are then presented in Section 6.3.

### 3.1 Methodology

#### 3.1.1 Simulation materials

Bulk bismuth telluride ( $\text{Bi}_2\text{Te}_3$ ) and antimony telluride ( $\text{Sb}_2\text{Te}_3$ ) both occur in quintuple layered (QL) lattice structures (Fig 3.1(a)), where each layer is composed as  $\text{Te1}-\text{X}-\text{Te2}-\text{X}-\text{Te1}$  ( $\text{X} = \text{Bi}$  or  $\text{Sb}$ ). The two Te atoms are in different bonding environments, with the Te2 atom forming strong *intra*-layer bonds, and the Te1 atoms forming weaker *inter*-layer van der Waal’s bonds. The bulk materials can be described by the primitive rhombohedral cell containing 5 atoms or the conventional hexagonal unit cell having 15 atoms (3 QLs). The experimental hexagonal cell lattice constants of the two materials are  $a_{\text{Bi}_2\text{Te}_3} = 4.369 \text{ \AA}$  and  $c_{\text{Bi}_2\text{Te}_3} = 30.42 \text{ \AA}$  for  $\text{Bi}_2\text{Te}_3$ [164], and  $a_{\text{Sb}_2\text{Te}_3} = 4.264 \text{ \AA}$  and  $c_{\text{Sb}_2\text{Te}_3} = 30.458 \text{ \AA}$  for

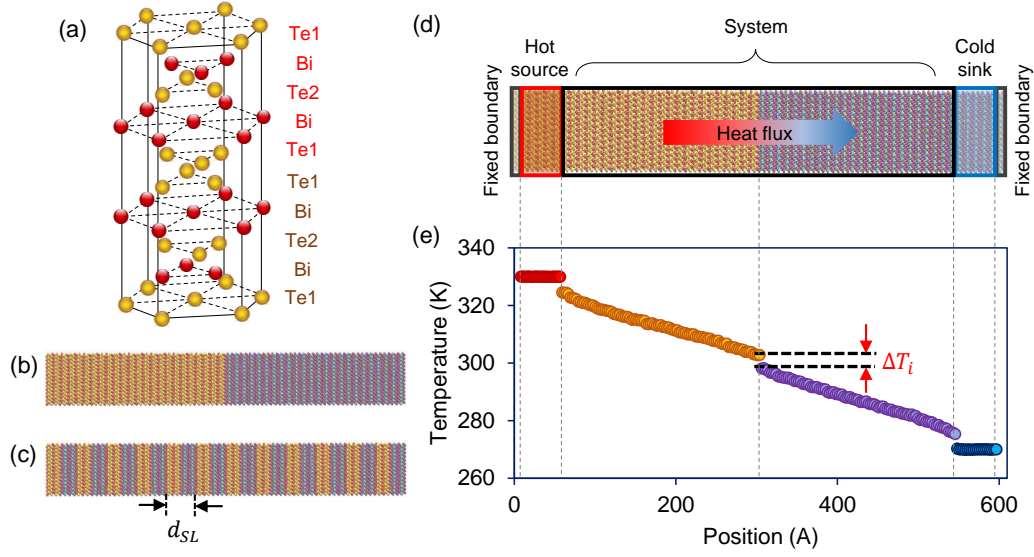


**Figure 3.1.** (a) Crystal structure of Bi<sub>2</sub>Te<sub>3</sub> showing two quintuple layers, (b) Schematic of Bi<sub>2</sub>Te<sub>3</sub>-Sb<sub>2</sub>Te<sub>3</sub> single interface and (c) superlattice with period  $d_{SL}$ . (d) NEMD simulation domain, showing the fixed layers of atoms at each end, the hot and cold baths and the direction of heat flux through the system in between. (e) Representative temperature profile for the single interface structure, showing the temperature drop  $\Delta T_i$  at the interface.

Sb<sub>2</sub>Te<sub>3</sub>[165]. In this work, orthogonal simulation domains are created using the conventional cells. A cross section size of  $10 \times 14$  unit cells is used in the  $x$  and  $y$  directions, which were found to provide converged thermal conductivity values. Along the  $z$ -direction, the single interface and superlattice structures are created by stacking of the quintuple layers. The periods of the superlattices studied in our work are varied from 1 – 5 QLs of each material (1 – 5 nm). The structures of the single interface and a representative superlattice is shown in Fig. 3.1(b-c).

### 3.1.2 Molecular dynamics simulations

Non-equilibrium molecular dynamics (NEMD) are performed using the LAMMPS package[166]. The equations of motion are integrated using a Verlet algorithm with a time step of 1 femtosecond, which is sufficient to resolve the phonon modes of both the materials. The schematic of the simulation domain is shown in Fig. 3.1(d). The Bi<sub>2</sub>Te<sub>3</sub>-Sb<sub>2</sub>Te<sub>3</sub> system is placed between two bulk regions of atoms at either end. Initially, periodic boundary condi-

tions are imposed in all three directions. The entire simulation domain is first relaxed under constant temperature and pressure (NPT) for  $1 \times 10^6$  timesteps (1 ns) to reduce the strain on the system, after which it is switched to a constant volume and energy ensemble (NVE) and run for  $0.5 \times 10^6$  timesteps (500 ps) for proper equilibration. Subsequently, 1 quintuple layer of atoms at each end are fixed to implement fixed boundary conditions along the  $z$ -direction. Next to each of the fixed ends, a 5 QL section of atoms are thermostatted using Langevin dynamics to create and maintain a temperature gradient across the system. The thermal conductivity calculated using NEMD simulations can be dependent on the lengths of the heat reservoirs. By varying the length of the thermal reservoirs, we find that the thermal conductivity does not depend on the length of the thermal reservoir if their length is 5 QL (5 nm) or more. A temperature difference of 60 K is applied across the system through the thermostatted regions. The temperature gradient in the system is obtained by dividing the simulation domain into bins of 1 QL width, and averaging the kinetic energies of the atoms within a bin. This temperature data is collected and averaged over 20 ns after steady state is achieved, to minimize statistical fluctuations. The time taken to observe a steady state temperature gradient and a stable heat current within the system depends on the simulation domain length in the  $z$ -direction, and can vary from less than 1 ns for small systems to 5 ns for larger lengths. A representative temperature profile for the single interface structure, showing the temperature drop  $\Delta T_i$  at the interface, is provided in Fig. 3.1(e). The interfacial thermal conductance ( $G$ ) can be calculated from the steady state heat flux ( $q$ ) and the temperature drop as

$$G = \frac{q}{\Delta T_i} \quad (3.1)$$

To calculate the thermal conductivity of the multilayer structure, a linear fit is made to the temperature profile across the system. The sections near the thermal reservoirs are excluded since they include non-linear effects due to the velocities of the reservoir atoms being artificially scaled. The slope of the linear fit is used to calculate the thermal conductivity as



$$\kappa = \frac{q}{dT/dz} \quad (3.2)$$

Suitable classical interatomic potentials need to be specified for each material to evaluate the interatomic forces during the MD simulation. Here, we use a two-body Morse potential form to represent the short range interactions for each material, which is given by

$$\varphi_s(r_{ij}) = D_e[\{1 - e^{-a(r_{ij}-r_0)}\} - 1] \quad (3.3)$$

where,  $\varphi_s$  is the short-range interatomic potential between atoms  $i$  and  $j$ ,  $r_{ij}$  is the distance between the atoms, and  $D_e$ ,  $a$  and  $r_0$  are the Morse potential parameters. The parameters for bulk  $\text{Bi}_2\text{Te}_3$  were fitted to this form by Qiu and Ruan[95], and have been widely used to predict thermal transport in both the bulk material[95], [160] and nanostructures such as thin films[161]–[163], nanowires[111] and alloys with embedded nanoparticles[112]. Similarly, the Morse potential parameters were fitted for  $\text{Sb}_2\text{Te}_3$  in our previous work[90], and subsequently used to predict the lattice thermal conductivity of the bulk material in good agreement with experimental measurements. We employ the above parameters in this work to describe the interactions among atoms belonging to the  $\text{Bi}_2\text{Te}_3$  layers and  $\text{Sb}_2\text{Te}_3$  layers respectively. In each of these two sets of potential parameters, the cutoff radius ( $r_c$ ) for interactions has been carefully chosen so as to preserve the layered structure of the materials. We use an arithmetic mixing rule to obtain the Morse potential parameters for cross-interactions between two atoms belonging to different materials. The cutoffs for the cross interactions are chosen to be the same as those of the corresponding types of bonds within each of the bulk materials. In addition to the short range interactions, we use a particle-particle particle-mesh (PPPM) solver to handle the long range coulombic forces due to the charges on the atoms. Considering the partially covalent nature of the materials, it is appropriate to assign partial charges to the atoms, the details of which can be found in earlier works[90], [95].

### 3.1.3 Modified Landauer transport calculation

Phonon transport across the single interface is also calculated using the modified Landauer transport calculations. For this, we consider an interface perpendicular to the  $z$  direction, between two semi-infinite bulk regions. The interfacial thermal conductance is calculated according to Eq 3.1, where the heat flux across the interface is given by

$$q_{1 \rightarrow 2} = \frac{1}{2(2\pi)^3} \sum_i \int_{\mathbf{k}} \hbar \omega(\mathbf{k}, i) |\mathbf{v}_g(\mathbf{k}, i) \cdot \mathbf{n}| [f(\omega(\mathbf{k}, i), T_1) - f(\omega(\mathbf{k}, i), T_2)] \tau_{1 \rightarrow 2}(\omega(\mathbf{k}, i)) d\mathbf{k} \quad (3.4)$$

In Eq 3.4,  $\omega(\mathbf{k}, i)$  is the frequency of the phonon mode with branch  $i$  at the  $\mathbf{k}$ -vector  $\mathbf{k}$ ,  $\mathbf{v}_g$  is the phonon group velocity,  $\mathbf{n}$  is the unit vector normal to the interface,  $f$  is the phonon occupation number given by  $f(\omega, T) = 1/(e^{(\hbar\omega/k_B T)} - 1)$  and  $\tau_{1 \rightarrow 2}$  is the frequency dependent phonon transmission across the interface. To account for the highly anisotropic phonon transport properties of the two bulk materials, the integration in Eq 3.4 is carried out over the full Brillouin Zone and the summation is over the different phonon branches or polarizations. The phonon properties are obtained from lattice dynamics calculation employing the above described interatomic potentials and performed using the General Utility Lattice Program (GULP)[167]. We discretize the Brillouin Zone using a  $65 \times 65 \times 65$   $\mathbf{k}$ -point grid to carry out the integration numerically. The acoustic mismatch model (AMM) and the diffuse mismatch model (DMM) are two widely used models for calculating phonon transmission coefficients across an interface considering elastic scattering only. Here, we use the DMM to calculate the phonon transmission coefficients to compare with our NEMD results. The DMM makes the assumption that phonons incident at an interface will lose all memory of their initial state (within the constraint of elastic scattering) and can transmit to either side with a probability proportional to the number of available phonon modes in that side of the interface. As a result, the DMM transmission probability can be calculated with respect to phonon frequency only, without considering the polarizations of the incident and transmitted phonons. The DMM transmission coefficients are calculated as

$$\begin{aligned}
\tau_{1 \rightarrow 2}(\omega) = & \left( \sum_{\mathbf{k}, i} |\mathbf{v}_g(\mathbf{k}, i) \cdot \mathbf{n}| \Delta V_{BZ, 2} \delta(\omega(\mathbf{k}, i), \omega) \right) / \\
& \left( \sum_{\mathbf{k}, i} |\mathbf{v}_g(\mathbf{k}, i) \cdot \mathbf{n}| \Delta V_{BZ, 1} \delta(\omega(\mathbf{k}, i), \omega) + \right. \\
& \left. \sum_{\mathbf{k}, i} |\mathbf{v}_g(\mathbf{k}, i) \cdot \mathbf{n}| \Delta V_{BZ, 2} \delta(\omega(\mathbf{k}, i), \omega) \right) \quad (3.5)
\end{aligned}$$

Here, the summations are carried out over the discretized BZs of each material using the corresponding phonon properties,  $\Delta V_{BZ, i}$  is the volume of a discretized cell in material  $i$  and  $\delta(\omega, \omega)$  is the Kronecker delta function which evaluates to 1 when  $\omega = \omega$  and 0 otherwise, to ensure elastic scattering.

Recently, it has been shown by Feng *et al.*[168] that phonon modes on either side of an interface can be in strong thermal non-equilibrium with each other. The original Landauer formulation does not include the effect of such non-equilibrium in the phonon temperatures used to calculate the temperature drop across the interface given by

$$\Delta T = T_{e,1} - T_{e,2} \quad (3.6)$$

Here,  $T_{e,1}$  and  $T_{e,2}$  are the emission temperatures of the phonons coming from the reservoirs in materials 1 and 2. However, the phonon temperature on each side of the interface should be calculated after taking into account the presence of incident phonons and reflected phonons from the bulk material on that side, and transmitted phonons from the material on the other side. Considering the temperature of all these types of phonons, Shi *et al.*[169] defined modal equivalent equilibrium temperatures (MEET)  $T_{\lambda,1}$  and  $T_{\lambda,2}$  given by

$$T_{\lambda,1} = T_{e,1} - \tau_{\lambda,1 \rightarrow 2}(T_{e,1} - T_{e,2})/2 \quad (3.7)$$

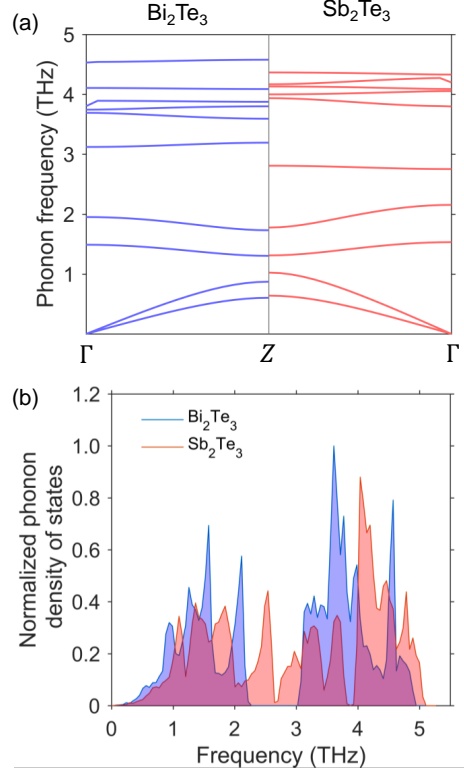


**Figure 3.2.** (a) Phonon dispersion along the high symmetry  $\Gamma - Z$  (cross-plane) direction in bulk  $\text{Bi}_2\text{Te}_3$  (left) and bulk  $\text{Sb}_2\text{Te}_3$  (right). (b) Phonon density of states in bulk  $\text{Bi}_2\text{Te}_3$  (blue) and bulk  $\text{Sb}_2\text{Te}_3$  (red)

$$T_{\lambda,2} = T_{e,2} + (1 - \tau_{\lambda,1 \rightarrow 2})(T_{e,1} - T_{e,2})/2 \quad (3.8)$$

Using these modified temperatures in the interface temperature drop as  $\Delta T_\lambda = T_{\lambda,1} - T_{\lambda,2}$ , the authors were able to show much better agreement of the calculated  $G$  with experimental results. More importantly, their approach was able to resolve the failure of the original Landauer formulation wherein a finite interfacial resistance is obtained even for an imaginary interface within a bulk material. As a result, we use the modified effective equilibrium temperatures in our Landauer transport calculations.

## 3.2 Results and discussions

### 3.2.1 Interfacial thermal conductance

We first study the phonon transport across the  $\text{Bi}_2\text{Te}_3$ - $\text{Sb}_2\text{Te}_3$  single interface. The atomic configurations, lattice constants and, thus, the phonon properties of the two bulk materials are very similar to each other. Figure 3.2(a) shows the phonon dispersions in the two bulk materials along the high symmetry  $\Gamma - Z$  direction (cross-plane), obtained from lattice dynamics calculations. The acoustic phonon branches and the lower optical phonon branches are very well matched in both materials, indicating ease of energy transmission across the interface. Since the simple two-body form of the developed interatomic potentials are not well suited for accurately reproducing the higher optical phonon branches, we ignore the mismatch at higher frequencies. Moreover, the contribution of optical phonons to the thermal conductivities of the bulk materials was found to be low from previous molecular dynamics simulation studies[90], [94], [95]. The phonon density of states (PDOS) over the entire BZ for the two materials is also shown in Fig. 3.2(b). As seen in the figure, the low frequency portions of the PDOS show very little mismatch with respect to the position and magnitude of the dominant peaks.

Non-equilibrium molecular dynamics simulations are performed to calculate the phonon transport across the  $\text{Bi}_2\text{Te}_3$ - $\text{Sb}_2\text{Te}_3$  interface for a range of interface temperatures from 200 – 400 K. The results for interfacial thermal conductance are shown in Fig 3.3(a). The thermal conductance value increases from  $0.9 \times 10^8 - 1.3 \times 10^8 \text{ W/m}^2\text{K}$  with increase in temperature, indicating the greater ease of thermal transport at higher temperatures. At low temperatures, the phonon transmission across the interface is largely expected to be elastic in nature, which places a constrain on the number of available phonon modes on the other side to receive thermal energy. With increase in temperature, the increase in inelastic scattering allows transfer of energy to a larger number of phonon modes with different frequencies due to three, four and higher order phonon-phonon scattering processes.

In order to gain insight into the spectral dependence of interfacial transport, we compute the phonon transmission coefficients using the DMM (Fig. 3.3(b)). The DMM transmission coefficient is around 0.40 – 0.45 for frequencies less than 1 THz, which can be correlated to

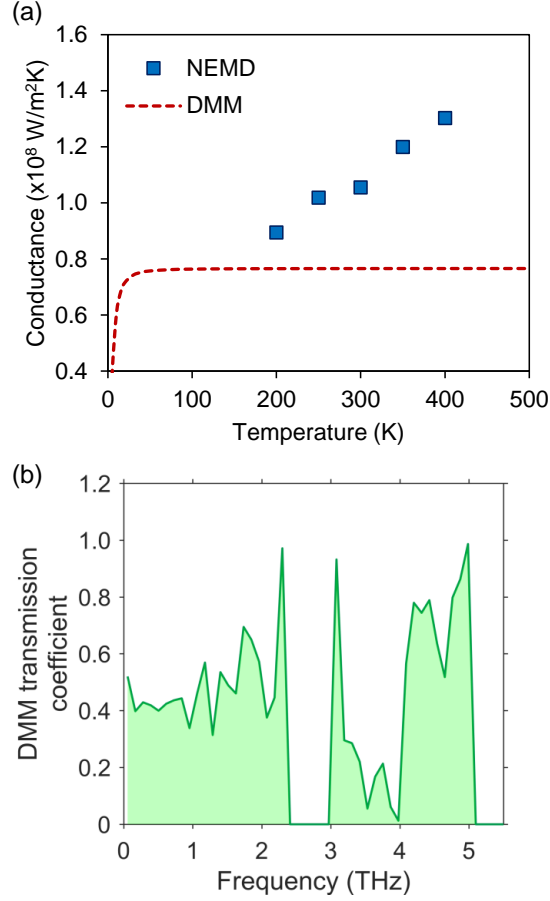


**Figure 3.3.** (a) Variation of thermal conductance of  $\text{Bi}_2\text{Te}_3\text{-Sb}_2\text{Te}_3$  interface with temperature, calculated using NEMD simulations (solid boxes) and the modified Landauer approach with DMM transmission coefficients (dashed line) (b) Phonon transmission coefficients from  $\text{Bi}_2\text{Te}_3$  to bulk  $\text{Sb}_2\text{Te}_3$  calculated using DMM

the highly matched PDOS and group velocities at these lower frequencies. The interfacial thermal conductance obtained using the modified Landauer transport calculations and DMM transmission coefficients is plotted in Fig. 3.3(a) for comparison with the NEMD calculated conductances. The DMM conductance increases with temperature and saturates at a value of  $0.75 \times 10^8 \text{ W/m}^2\text{K}$  over temperatures of 40 K. The difference between the DMM conductance and the NEMD conductance increases with increasing temperature, which is attributed to the increase in pathways for energy transfer between the phonons due to inelastic scattering processes.

### 3.2.2 Thermal conductivity of superlattices

NEMD simulations are also used to calculate the thermal conductivities of the  $N - N$  superlattice system with varying superlattice period, where  $N$  refers to the number of quintuple layers of  $\text{Bi}_2\text{Te}_3$  and  $\text{Sb}_2\text{Te}_3$  within a period. The thermal conductivity calculated using NEMD simulations is dependent on the length the system across which the non-equilibrium conditions are maintained. If the system length is too short, phonons from one reservoir can reach the other without scattering and also lead to artificial effects due to phonon reflection at the reservoirs. Schelling *et al.*[170] proposed a formulation to correlate the system length  $L$  to the limited phonon mean free path  $\lambda$ , given by  $\lambda^{-1} = \lambda_{\infty}^{-1} + L^{-1}$ , where  $\lambda_{\infty}$  is the intrinsic phonon mean free path. As a result, a linear relation between the inverse of thermal conductivity and the inverse of system length can be expected. The bulk thermal conductivity can then be obtained by extrapolating the linear curve to infinite length. Figure 3.4(a) shows the calculation of bulk thermal conductivity from the extrapolated linear fits for the 1 – 1 and 4 – 4 SLs.

The variation of the superlattice thermal conductivity with respect to SL period is shown in Fig. 3.4(b). The thermal conductivity initially decreases with increasing superlattice period and reaches a minimum thermal conductivity of 0.27 W/mK at a period of 4 nm. With further increase in superlattice period, the thermal conductivity increases. Several experimental [16], [51], [53], [171], [172] and numerical[46], [47], [49], [50], [173] studies have highlighted the existence of a minimum superlattice thermal conductivity as the period length is varied, which has been attributed to the competition between incoherent phonon and coherent phonon dominated transport regimes. At large superlattice periods, the thermal transport is mainly limited by incoherent phonon scattering at the interfaces, which increases at lower superlattice periods or higher interface densities. In this regime, anharmonic phonon-phonon scattering leads to loss of phase information before the phonons encounter an interface. However, if the period is reduced further, interference of phonons undergoing *phase-preserved* reflections at the interfaces leads to a modified phonon spectrum. In this regime, the coherent phonons are not scattered at the interfaces, and the thermal conductivity actually increases at very low superlattice periods, which has been explained by

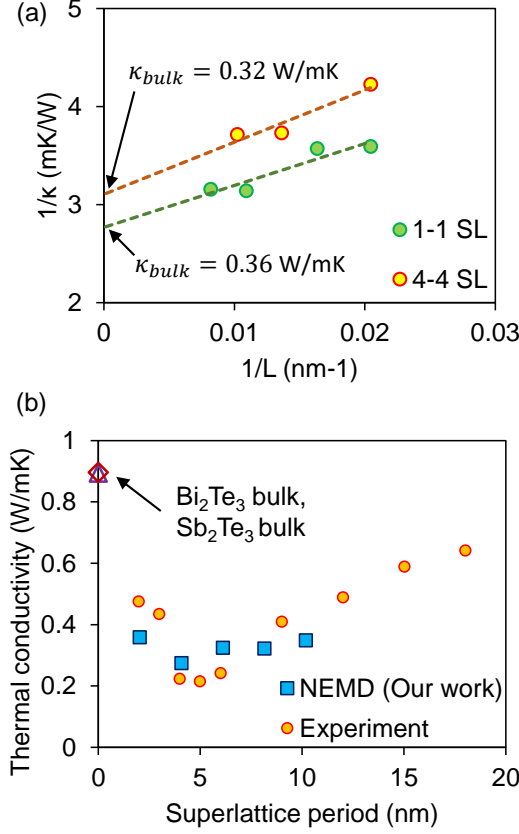


**Figure 3.4.** (a) Variation of  $1/\kappa$  with  $1/L$  for the 1–1 and 4–4  $\text{Bi}_2\text{Te}_3$ - $\text{Sb}_2\text{Te}_3$  SLs, and the bulk thermal conductivity calculated by extrapolating the linear fit to infinite length (b) Variation of the  $N - N$   $\text{Bi}_2\text{Te}_3$  - $\text{Sb}_2\text{Te}_3$  SL  $\kappa$  with SL period calculated using NEMD simulations (blue squares). Experimental data by Venkatasubramanian[16] are plotted for comparison (orange circles)

mechanisms such as less zone folding leading to weaker band flattening and increased group velocities.

The thermal conductivities of  $\text{Bi}_2\text{Te}_3$  - $\text{Sb}_2\text{Te}_3$  SLs were experimentally measured by Venkatasubramanian[16] using a thin film  $3-\omega$  method. Their data is plotted in Fig. 3.4(b) for comparison with our NEMD calculations. The experimental data shows a larger variation in thermal conductivity ( $0.22 - 0.48 \text{ W/mK}$ ) than our NEMD results ( $0.27 - 0.36 \text{ W/mK}$ ) for the range of superlattice periods considered in our calculations. Despite this, we find that our calculated values lie in the same range as the experimental results and exhibit similar trends. Moreover, the observed minimum thermal conductivity in our results occurs around the same superlattice period as the experimental data. The discrepancies between



experimental and calculated results can partly arise from difficulties in fabricating superlattices with nanometer-scale periods, which can lead to presence of atomic interdiffusion at the interfaces and variance in the superlattice period thicknesses.

### 3.3 Conclusions

In summary, we have calculated the interfacial thermal conductance across  $\text{Bi}_2\text{Te}_3$ - $\text{Sb}_2\text{Te}_3$  interfaces using non-equilibrium molecular dynamics (NEMD) simulations which employ the two-body interatomic Morse potential parameters developed in our earlier works. The interfacial conductances are found to increase over a range of temperatures from 200 – 400 K. We also use the modified Landauer transport calculations with the phonon transmission coefficients obtained from the diffuse mismatch model (DMM). Our calculations consider the phonon dispersion over the full Brillouin zone to account for the anisotropic phonon transport properties of the bulk materials. The highly matched nature of the acoustic phonons and the lower optical phonon branches are reflected in the DMM transmission coefficients at low frequencies. The difference between our NEMD calculated conductances and those from our Landauer transport calculations increases at higher temperatures, which is attributed to the increasing contribution of inelastic phonon scattering processes. We also use NEMD simulations to calculate the thermal conductivities of  $\text{Bi}_2\text{Te}_3$ - $\text{Sb}_2\text{Te}_3$  superlattices (SLs) with varying periods. A minimum SL thermal conductivity of 0.27 W/mK is observed at a period of 4 nm from our NEMD calculations. Our results show good agreement with experimental measurements found in literature, with respect to the range of thermal conductivities and the location of the minimum SL thermal conductivities. The insight gained in our study paves the way for designing efficient thermoelectric devices and investigating other potential multilayer structures such as interfaces with atomic diffusion and random multilayers.

## 4. MACHINE LEARNING MAXIMIZED ANDERSON LOCALIZATION OF PHONONS IN APERIODIC SUPERLATTICES

### 4.1 Introduction

The design and discovery of nanostructured materials with targeted thermal transport properties has become increasingly important in various applications such as thermal management of electronic chips and batteries [174], [175], thermal interface materials [176], [177], thermal barrier coatings [178], [179] and thermoelectrics [180]. For example, high figure-of-merit thermoelectric devices require ultra-low thermal conductivity materials without significantly reduced electrical conductivity. Several methods have been investigated to reduce thermal conductivity by increasing phonon scattering using isotopes[181], [182], defects[183], [184] and grain boundaries[6]. In the past few decades, multilayer phononic structures such as binary superlattices (SLs) have gained widespread attention due to their potential for low thermal conductivity caused by increased interface scattering[16], [144], [154], [155]. The thermal conductivity of SLs exhibits a minimum with variation of superlattice period, which has been observed in many numerical studies[46]–[50] and confirmed in some experimental investigations[16], [51]–[54].

Recently, it has been predicted that the minimum thermal conductivity can be further suppressed by randomizing the SL layer thicknesses,[55], [58]–[60] which introduces phase-preserving scattering mechanisms leading to coherent phonon localization. Wang *et al.* [59] formulated a two-phonon model to decompose the thermal conductivity of SLs and RMLs into coherent and incoherent phonon contributions. Moreover, the influence of parameters such as bond strength[55], interface roughness[55], [57], [185] and isotopic modulation[186] on the thermal conductivity of multilayer structures has also been investigated. More recently, evidence of localization of coherent phonons in disordered graphene phononic crystals was shown by Hu *et al.*[187], while Juntunen *et al.*[188] provided a spectral description of the frequency-dependent phonon localization lengths in Si/Ge RML systems. We note that in many of the above studies, the variation in thermal conductivities of RMLs arising from

independently generated random structures was not elucidated. In contrast, Ju *et al.*[156] observed a significant spread in thermal conductivities of Si/Ge RMLs with different distributions of layer thickness, even at the same average period and composition ratio. Their results indicate that such structural parameters give rise to a very large design space, yet their effect on the lower limit of RML thermal conductivity has not been resolved. An optimization study within this design space will enable us to obtain a more fine-grained tunability of thermal conductivity as well as gain insight into the underlying physics of phonon transport in RML structures.

The selection of experiments and simulations for materials discovery and property engineering has traditionally been guided by the domain knowledge of researchers in the relevant field. However, such intuition-based explorations, combined with prohibitively large design spaces, may preclude the discovery of low-probability-of-occurrence novel solutions which show counter-intuitive trends. Recently, metaheuristics and machine learning-based methods have increasingly been used to accelerate the exploration of new materials with targeted properties[157], [189], prediction of material structures[190], [191] and optimization of nanostructure geometry[88], [156], [158]. The availability of specialized hardware architectures has led to increased popularity of various machine learning techniques including neural networks[192]–[194], genetic algorithms[195], [196] and support vector machines[197] among others. In this work, we use a genetic algorithm (GA)-based search process in conjunction with molecular dynamics (MD) simulations to discover the lower limit of thermal conductivity in Si/Ge random multilayer systems. Our machine learning-based approach demonstrates the elimination of human bias in the search process, thereby allowing us to identify non-intuitive trends in structural features leading to ultralow thermal conductivity. It is observed that the minimum RML thermal conductivity occurs, surprisingly, at a lower average period than that at which the minimum superlattice thermal conductivity is found. Finally, it is desirable, but challenging, to come up with a set of descriptors out of the optimization process, which can be intuitively understood and adopted during experimental realizations of such systems. Our work provides a hierarchical description of these structural features that will provide guidance for application of RML systems in various applications.

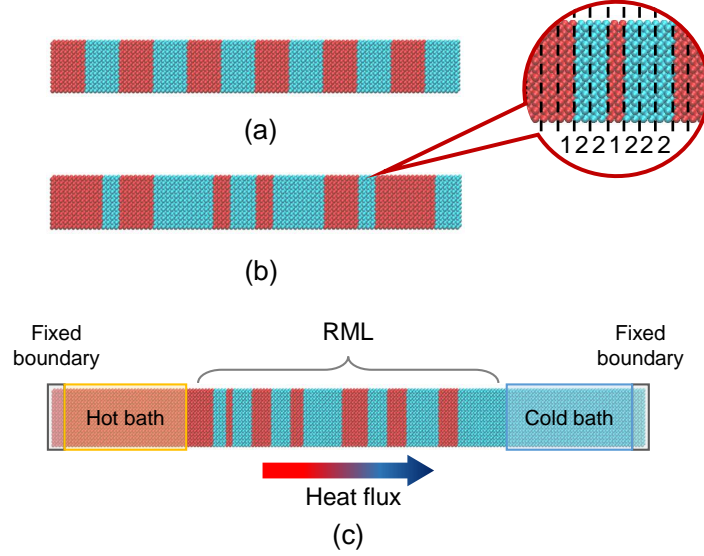


**Figure 4.1.** Representative structures showing (a) superlattice of period 4.4 nm and (b) random multilayer with the same average period. Inset shows encoding of the RML structure in the GA as an  $N$ -bit array, where each bit is assigned 1 or 2 if the unit cell is Si or Ge respectively. (c) Schematic of the NEMD simulation setup showing the RML sandwiched between two heat baths which are thermostatted to impose a heat flux through the system.

## 4.2 Simulation methods

### 4.2.1 Designing RML structures

We have studied superlattice (SL) and random multilayer (RML) structures created from diamond structured Si and Ge with the heat transport along the  $[001]$  direction. A number of theoretical and numerical studies have been performed on Si/Ge systems such as bulk alloys[198], [199], superlattice thin films[200]–[203] and superlattice nanowires[204]–[206], due to the ubiquitous presence of these semiconductors in a variety of applications. The lattice constant is initially set at 0.543 nm which is the room temperature lattice constant of silicon. To create the SL and RML structures, layers of Si and Ge are stacked along the  $[001]$  direction in a periodic and random manner, respectively. The smallest allowable thickness of a layer is chosen to be one unit cell. The representative SL and RML structures are shown in Fig 4.1 (a-b). The period of the SL is defined as the total thickness of a pair of consecutive Si and Ge layers, while for the RML, the period is calculated as the sum of the

average thicknesses of Si and Ge layers in the whole structure. We perform our calculations for system sizes of  $6 \times 6$  unit cells in the in-plane direction (cross-section), and 10 or 40 unit cells (5.43 nm or 21.72 nm respectively) in the cross-plane direction. No constraint is placed on the composition ratio of the RML structures (ratio of the number of layers of Si and Ge), which is allowed to vary during the optimization procedure.

#### 4.2.2 Non-equilibrium molecular dynamics simulations

Non-equilibrium molecular dynamics (NEMD) simulations are performed using LAMMPS[166] to calculate the thermal conductivity of the multilayer structures. The schematic of the simulation setup is shown in Fig 4.1 (c). The SL/RML is placed between two heat bath regions on either side which are capped by two end regions of fixed atoms to prevent sublimation. The interaction between Si and Ge atoms is modeled using the Tersoff potential[207], which has been widely used to predict thermal transport in Si-Ge system. The equations of motion are integrated using a Verlet algorithm with a timestep of 0.5 fs. Initially, periodic boundary conditions are applied in all directions and the system is relaxed at zero pressure and a temperature of 300 K in an NPT ensemble for 500 ps, after which it is run for another 250 ps in an NVE ensemble to observe proper conservation of energy. To introduce non-equilibrium conditions, the atoms in the two end regions are then fixed, and the temperatures of the hot and cold baths are maintained at 330 K and 270 K respectively using Langevin thermostats to create a temperature gradient in the multilayer region. The system is allowed to reach steady state over a time of 4.5 ns and the temperature profile is monitored by binning the velocities of atoms along the direction of heat transport. The cross-plane thermal conductivity is then obtained from the steady state heat flux  $q$  as

$$\kappa = \frac{q}{\Delta T/L} \quad (4.1)$$

where  $L$  is the length of the multilayer structure. The thermal boundary resistance (TBR) is calculated from the temperature drop at each individual interface ( $\Delta T_i$ ) as

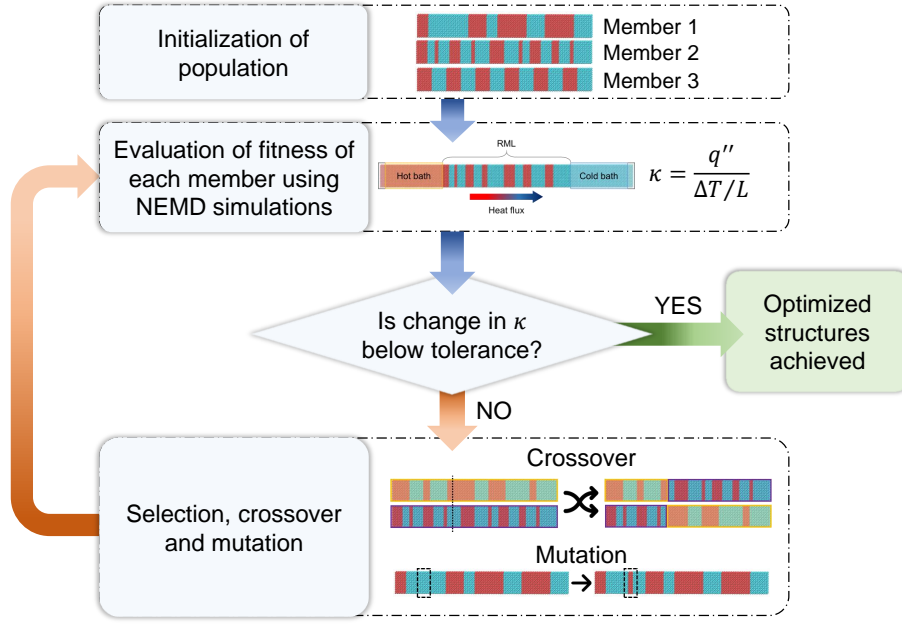


**Figure 4.2.** Schematic of the genetic algorithm based optimization method showing the different steps involved. The GA population is initialized randomly with a chosen number of members and the fitness of each member is based on its thermal conductivity evaluated using NEMD simulations. The stopping criteria is checked and if it is not achieved, selection, crossover and mutation operations are carried out on the best individuals to obtain the next generation.

$$R_i = \frac{\Delta T_i}{q} \quad (4.2)$$

### 4.2.3 Genetic Algorithm based optimization method

Genetic algorithms are a class of evolutionary algorithms which mimic the principle of natural selection to arrive at the fittest solution in an optimization problem. The basic principle used by the by a GA is that already identified good solutions can provide potentially better solutions by evolutionary operations. In a GA based optimization approach, each candidate solution in a multivariate design space is represented by a string called a *chromosome*, formed by concatenating the individual encoded variables or *genes*. A commonly used

approach to encode variables in a GA is converting numeric values to binary strings, which lends itself conveniently to evolutionary operations. Subsequently, an initial population is formed out of a chosen number of chromosomes, which may be generated randomly or using previous intuition about the design space. An objective function is designed for the particular problem to evaluate the performance of candidate solutions. Each member of the initial population is assigned a fitness value based on its evaluation against the objective function. In the next step of the iteration, a new population of the same size is generated by performing the evolutionary operations of selection, crossover and mutation on the individuals of the current population. Selection ensures that only the fittest individuals in the current iteration are carried over to the next, and can be done probabilistically based on the fitness values of the individuals. Crossover (or reproduction) produces new candidate solutions by combining genes from the selected individuals, while mutation perturbs the value of randomly selected genes within a chromosome so that unexplored areas of the design space can be accessed. Together, these operators ensure that the search does not get trapped in a local optimum within the solution space. The GA progresses by performing the above operations on the new population members, until a convergence criteria is reached, which can be set with respect to the change in fitness value over successive generations.

We now discuss the implementation of the above steps in our GA based optimization process. To encode RML structures as chromosomes, an  $N$ -bit binary array is used for an RML of  $N$  unit cells length in the cross-plane direction. As shown in the inset of Fig 4.1, each position in the array is coded as 1 if it is a Si unit cell and 2 if it is a Ge unit cell. In this way, each chromosome representing an RML structure is formed of  $N$  binary variables, each of which can take values of 0 or 1. Additionally, the first and last unit cells which are in contact with the heat baths at each end are fixed to be Si (0) and Ge (1) respectively. As a result, the number of possible solutions in the design space is  $2^{N-2}$ . A population size of 20 is used and the initial population is formed out of 20 RML structures which can be generated randomly or according to our choice. The inverse of the cross-plane thermal conductivity is chosen as the objective function, which is maximum for the structure with the lowest thermal conductivity. We employ a rank-based selection scheme, in which the probability of each individual being selected is proportional to the inverse of its rank when

the individuals are sorted by fitness values from best to worst. For every two individuals selected, crossover and mutation operations are performed to partially alter their genes so that possibly better solutions can be obtained from the fittest individuals identified so far. We implement a single-point crossover, in which a position along the  $N$ -bit array is chosen randomly and the sections of the chromosome following this position are interchanged among the two individuals. In contrast, mutation involves a single chromosome and is implemented probabilistically in either of two ways: (i) at a single position randomly chosen along the chromosome, the value of the gene is flipped (1 to 0 or vice-versa), or (ii) the size of a layer of contiguous variables with the same value (0 or 1) is increased or decreased by switching its neighboring variables to the same value. The first process can change the number of interfaces in the RML structure by flipping the material type at a location, whereas the second process alters the average period and composition ratio of the structure by changing the thickness of a layer of Si or Ge. We use a crossover probability of 0.8 and a mutation probability of 0.4 based on convergence rates observed in preliminary trials. A schematic process flow of the GA based optimization process, involving evaluation of the fitness function and implementation of the crossover and mutation operations, is shown in Fig 4.2.

### 4.3 Results and discussions

#### 4.3.1 Manual intuition-based search for the minimum RML thermal conductivity

The thermal conductivities of the  $N - N$  superlattice system of length 40 unit cells are first calculated, where  $N = 1, 2, 4, 5, 10$  and 20 to allow only an integral number of periods. Figure 4.3 (a) shows that a minimum superlattice thermal conductivity of around 3.5 W/mK is found to occur at period of 4.43 nm. The nature of the variation of thermal conductivity with average SL period has been explored in literature in significant detail [16], [46]–[54]. The existence of the minimum superlattice thermal conductivity has been attributed to the competition between incoherent and coherent phonon dominated transport regimes. When the superlattice period  $\bar{d}$  is large, phase breaking occurs due to anharmonic phonon-phonon scattering and the role of incoherent phonons become more important. As the superlattice



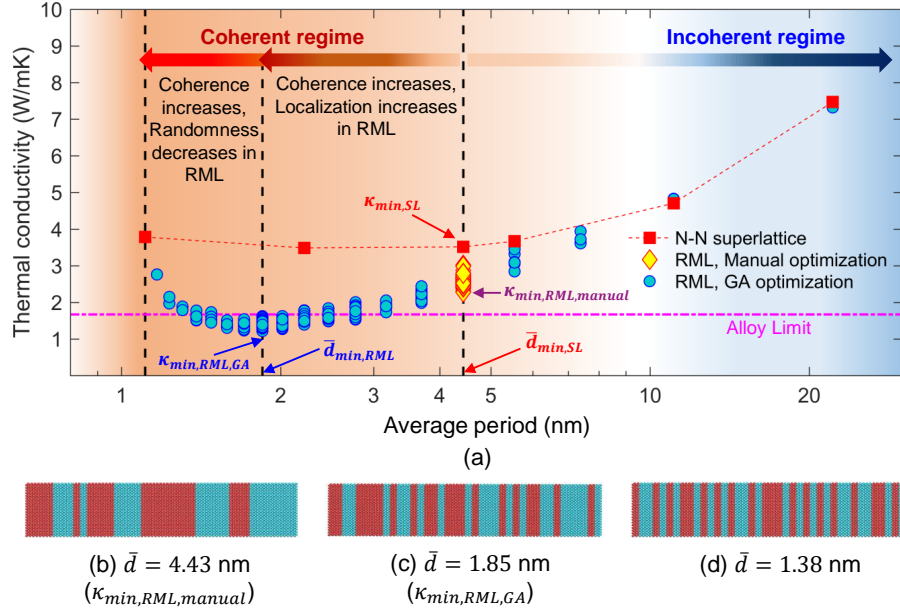


**Figure 4.3.** (a) Variation of thermal conductivity with average period length for N-N superlattices (red squares), RML structures obtained using manual intuition-based optimization (diamonds) and RML structures obtained using machine-learning based optimization (filled circles). The minimum RML thermal conductivity obtained from our optimization algorithm occurs at a smaller average period than that at which the minimum superlattice thermal conductivity is observed. The dashed purple line marks the random alloy limit. (b) RML structure with minimum thermal conductivity obtained from a manual optimization, (c) RML structure with minimum thermal conductivity obtained from a machine-learning based optimization, and (d) RML structure with average period below  $\bar{d}_{min, RML}$ .

period decreases, the increase in interface density leads to higher phonon-boundary scattering and reduced thermal conductivity. On the other hand, wave interference effects become increasingly important at small  $\bar{d}$ , and the phase breaking of phonons does not take place before the phonons scatter at the interfaces. The repeated reflections at periodic interfaces give rise to a modified phonon spectra including coherent phonon modes which are not scattered at the interfaces. Decreasing  $\bar{d}$  below the critical superlattice period leads to an increase in thermal conductivity, which has been explained by effects such as less zone folding leading to weaker band flattening and increased group velocities.

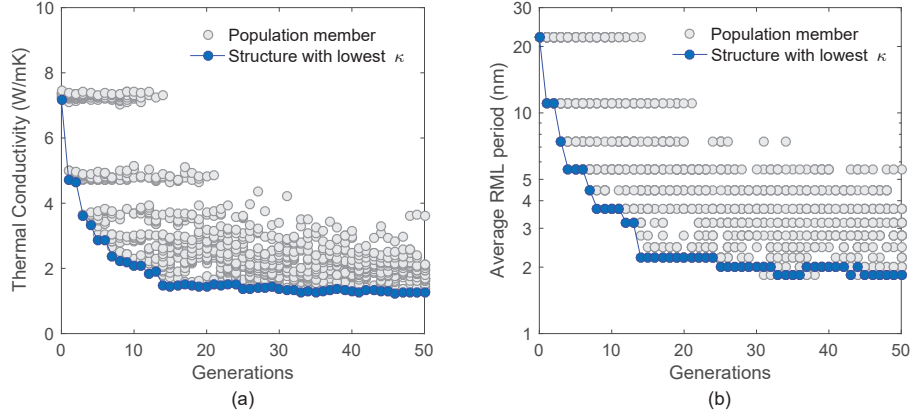


**Figure 4.4.** Variation of (a) thermal conductivity and (b) average RML period of the population with each iteration of the genetic algorithm based search process. The blue circles mark the best individual (lowest  $\kappa$ ) of each generation

The design space for imparting randomization to the superlattices is extremely high, making an exhaustive search for the RML with minimum thermal conductivity impossible. For a multilayer system consisting of  $N$  unit cells where the shortest layer length is constrained to be one unit cell, the total number of possible RML structures is  $2^N$ . In such cases, the traditionally adopted best approach is to search a smaller subset of the solution space, guided by previously discovered knowledge and intuition about heat transport in multilayer structures. Since the superlattice thermal conductivity minimum is obtained around a period of 4 nm considering our results and those in literature[202], it can be intuitively expected that the RML with minimum thermal conductivity can be obtained by randomizing the layer thicknesses of the same superlattice. As a result, we perform a manual search by evaluating the thermal conductivities of 100 randomly generated RML structures with an average period of 4.43 nm. The thermal conductivities of such RML structures are plotted in Figure 4.3 (a). The lowest thermal conductivity obtained among these structures is 2.45 W/mK for the structure shown in Fig 4.3 (b), which represents a 30% reduction from the minimum superlattice thermal conductivity.

### 4.3.2 Genetic Algorithm-based search for the minimum RML thermal conductivity

Considering the infeasibility of an exhaustive search of the extremely large solution space, the use of machine learning can benefit the current problem significantly. Here, we choose a genetic algorithm (GA) to predict the best simulations to perform on our finite computational resources by utilizing information from the results of previously performed simulations. We apply the GA based search process on RML systems consisting of 40 unit cells (21.72 nm). In order to explore greater portions of the design space and avoid getting trapped within local minima, 15 independent GA runs are performed starting from different initial populations. Figure 4.4 shows the results of one run started with an initial population consisting entirely of structures with a single Si-Ge interface and a composition ratio of 1. Since this structure has the lowest possible interface density, we expect it to be the worst candidate in the design space. As a result, this initial population can be considered as a starting point for the search when no prior knowledge or intuition is available about the minimum thermal conductivity. The genetic operators of crossover and mutation allow the GA to converge towards the minimum thermal conductivity even with this sub-optimal initial population. The evolution of the population with iterations of the GA is shown in terms of thermal conductivity in Fig 4.4 (a) and the average RML period in Fig 4.4 (b). As seen in Figure 4.4 (a), although all individuals of the initial population show high thermal conductivities, these gradually get eliminated from the population in subsequent generations. The reason for this can be understood by noting from Fig 4.4 (b) that the later generations contain RMLs with much lower average periods and thus higher interface densities. The lowest thermal conductivity value for the entire population decreases rapidly and saturates about the minimum value in about 35 generations, in RMLs with an average period of 1.85 nm. The RML structure with the lowest thermal conductivity among all the GA searches performed is shown in Fig 4.3 (c).

### 4.3.3 Influence of average RML period on the minimum thermal conductivity

To gain insight into our optimization results, the thermal conductivity variation with average period for the RMLs sampled during all our optimization runs on the 40 unit cell RML system is plotted in Fig 4.3 (a). We only include structures with a composition ratio of 1 in order that the results can be compared to the  $N - N$  superlattice system. The major transport regimes can be easily identified from the relative magnitudes of SL and RML thermal conductivities at different average periods. At high average RML periods ( $>10$  nm), the thermal conductivity of RMLs is similar to that of SLs, indicating that randomization of layer thicknesses has negligible effect on thermal conductivity. Incoherent phonons, therefore, dominate thermal transport in both SLs and RMLs at these high periods. Below 10 nm, the thermal conductivity of RMLs keeps on decreasing with decreasing average period, while that of SL starts to level off. As a result, we can infer that coherent phonon transport starts becoming important in SLs in this region. As the average period further decreases, the thermal conductivity of the  $N - N$  superlattice reaches a minimum at the critical SL period ( $\bar{d}_{min,SL}$ ) and then bounces back. However, the thermal conductivities of RMLs keep on reducing until reaching a minimum at a period of  $\bar{d}_{min,RML} = 1.85$  nm, which is, notably, much lower than the critical SL period ( $\bar{d}_{min,SL}$ ). This surprising behaviour can be attributed to the fact that while the increasing phonon coherence leads to an increase in the thermal conductivity for the SL, it puts more phonon modes in localization in RMLs causing a decrease in thermal conductivity. Moreover, the occurrence of the observed minimum RML thermal conductivity at a smaller period than what was intuitively expected proves that our previous manual search could at best converge to a local minimum, and highlights the effectiveness of machine-learning based methods. We also calculated the random alloy limit of thermal conductivity by randomly assigning 50 percent of atomic masses in a Si structure of the same length to the mass of Ge, which is plotted in Figure 4.3 (a). As seen from the figure, the GA-optimized RML structures are able to break the random alloy limit by more than 25 %. Although the phonons in the random alloy structures have small mean free paths due to alloy scattering, they can still propagate and contribute to the thermal conductivity.

However, the majority of coherent phonons in the RML are completely localized and have no contribution to the thermal transport, leading to lower thermal conductivity values.

Below  $\bar{d}_{min,RML}$ , the thermal conductivity of RMLs increases steeply as the average period decreases further. This occurs because at such low average periods, the room for randomizing the individual layer thicknesses from the periodic SL thickness becomes small, as a result of which localization of coherent phonons is reduced significantly. This is seen in Fig 4.3 (b-d) where the RML with the lowest thermal conductivities obtained for three different average periods from the GA are plotted. For  $\bar{d} = \bar{d}_{min,RML} = 1.85\text{nm}$  (Fig 4.3 (c)), the layer thicknesses have room to become sufficiently randomized to allow for localization of coherent phonons, while providing a high interface density for incoherent phonon scattering. The combination of both of these favorable effects leads to the existence of the minimum RML thermal conductivity at this period. For  $\bar{d} = 1.38\text{nm} < \bar{d}_{min,RML}$  (Fig 4.3 (d)), the majority of the superlattice has to be composed of single layers of Si and Ge arranged periodically, which allows for less room for localization of coherent phonons. In the limiting case of the shortest average period possible ( $\bar{d} = 1$  unit cell of Si + 1 unit cell of Ge), the RML structure is the same as a 1-1 superlattice with no room for introducing randomness. On the other hand, at periods greater than  $\bar{d}_{min,RML}$  (Fig 4.3 (b)), the larger thicknesses of individual layers provide more freedom for randomization and spatial distribution of layers. However, the lower interface density also gives rise to lower incoherent phonon scattering and overall higher thermal conductivities.

#### 4.3.4 Degree of randomness

RMLs with the same average period and composition ratio can still have different distributions of layer thickness within them. Since the interface densities and hence the degree of incoherent phonon scattering in such RMLs are the same, the variation in thermal conductivity at a particular average period, observed in Fig 4.3 (a), is attributed to varying degrees of localization of coherent phonon modes within the RMLs. The existence of partially localized phonon modes in RMLs was identified from the thermal conductivity accumulation with respect to phonon frequency by Juntunen *et al.*[188]. Such partially localized modes,

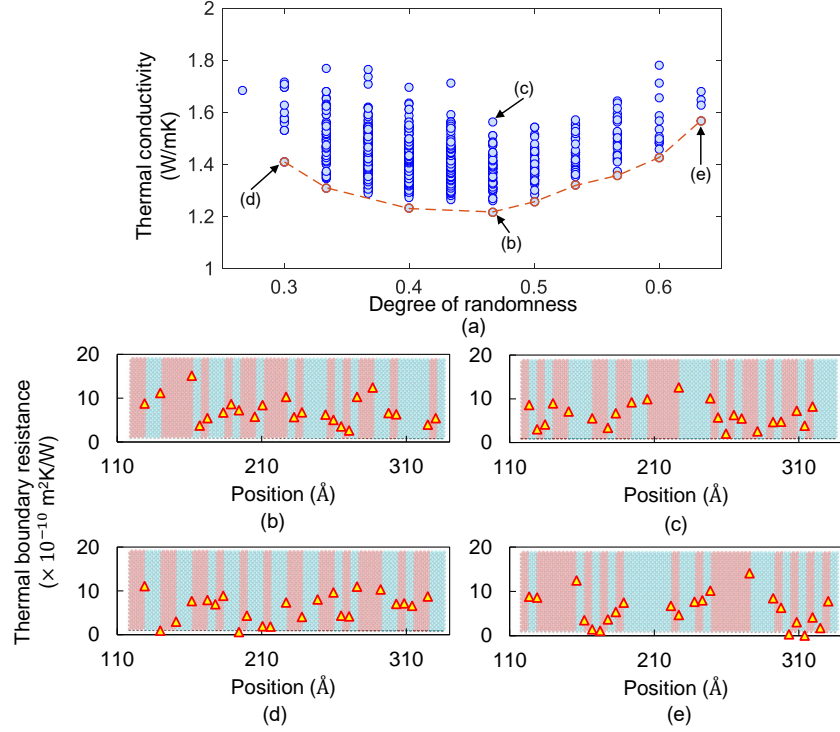


**Figure 4.5.** (a) Dependence of thermal conductivity of RML structures on the degree of randomness (DOR) as defined in the text. The orange circles and dashed lines represent the lower bound of thermal conductivity obtained using our machine-learning based search process. For the four structures marked in the plot, the calculated thermal boundary resistances of all interfaces in each of the structures, superimposed on the visualization of the RML structures themselves, are shown in figures (b)-(e).

which have finite contribution to thermal conductivity of RMLs, will depend on the local randomization of layers throughout the RML structure. The degree of randomization of a RML can be quantified by the normalized average deviation of layer thicknesses from that of the corresponding SL of the same period, and is given by

$$DOR = \frac{\sum_{i=1}^n |t_i - \bar{d}/2|}{n \times \bar{d}/2} \quad (4.3)$$

Here,  $n$  is the number of periods in the RML,  $t_i$  is the thickness of individual layers and  $\bar{d}$  is the average RML period which is also the corresponding SL period. Normalization by

the mean period accounts for the fact that the same average deviation from a smaller mean period causes a larger degree of randomness than from a larger mean period. The variation of thermal conductivity with  $DOR$  is plotted in Figure 4.5 (a) for all RML structures with an average period of  $\bar{d} = \bar{d}_{min,RML} = 1.85$  nm and a composition ratio of 1. Although it is intuitively expected that a larger deviation from the periodic SL structure leads to lower thermal conductivity of RMLs, we surprisingly find that the RML structure with minimum thermal conductivity occurs at an intermediate degree of randomness. Moreover, a variation in thermal conductivity of 25 % is observed within structures at this degree of randomness. To understand the reasons governing this non-intuitive trend, we calculate the thermal boundary resistance (TBR) at the interfaces within four RMLs selected at different degrees of randomness, as marked in Fig 4.5. To eliminate the effect of lattice mismatch, the lattice constants of both Si and Ge in these simulations are fixed at 0.543 nm. The trends in thermal conductivity obtained for these lattice-matched RMLs is verified to be similar to those in the original systems. The TBRs obtained within the four structures are shown in Figures 4.5 (b-e), superimposed on the corresponding RML structures for easier visualization. At low values of  $DOR$ , the deviation of the RML from the corresponding SL is low and much of it retains the periodic structure. As a result, localization of coherent phonons is less in these RMLs, leading to coupled interfaces with low values of TBR in these periodic regions as seen in Fig 4.5 (d). On the other hand, high values of  $DOR$  require some layer thicknesses of the RML to be quite large, while other regions are necessarily composed of contiguous single layers leading to periodic interfaces and low TBR values (Fig 4.5 (e)). However, at an intermediate degree of randomness, the occurrence of both small and large layer thicknesses interspersed among each other creates a favourable environment for coherent phonon localization, leading to relatively higher values of TBR across the entire structure (Fig 4.5 (b)). Finally, Figure 4.5 (c) shows the TBRs calculated in another RML at this intermediate  $DOR$ , in which periodic sections with low interfacial resistances are noticed. Although the distribution of layer thicknesses in this RML are similar to the best structure (b), the different relative placement of these layers within the RML leads to formation of periodic zones within this RML with low interfacial resistances and higher thermal conductivity.

## 4.4 Conclusions

To summarize, we have searched for the lower limit of thermal conductivity in Si/Ge based RML systems using both an intuition-guided manual search and a genetic algorithm based search process. We find that our manual search is, at best, able to converge to a local minimum of thermal conductivity, while the machine-learning based search can efficiently lead us toward the RML structure with the globally minimum thermal conductivity. The minimum RML thermal conductivity is found to occur at an average RML period that is much lower than the period of minimum SL thermal conductivity. The location of this average period is determined by a tradeoff between high interface density at smaller periods and sufficient scope for randomizing the layer thicknesses at larger periods. The variation in thermal conductivity within RMLs having the same period is further resolved by defining the degree of randomness as a measure of deviation of the RML layer thicknesses from the periodic SL layer thickness. We have shown that the GA optimized minimum thermal conductivity occurs for RMLs with an intermediate degree of randomness. By calculating the thermal boundary resistances within different RMLs, it is observed that greater local mismatch between adjacent layers leads to higher coherent phonon localization and thus higher TBRs. The different distributions of layer thickness and moreover the spatial placement of these layers causes a variation in the degree of coherent phonon localization. The generality of our optimization method implies that it can be applied to other systems as well such as graphene sheets with disordered arrangement of pores and binary superlattices with rough interfaces of different geometries.



## 5. AN ITERATIVE MACHINE LEARNING APPROACH FOR DISCOVERING UNEXPECTED THERMAL CONDUCTIVITY ENHANCEMENT IN APERIODIC SUPERLATTICES

### 5.1 Introduction

The demand for efficient energy systems and high-performance electronic devices has created the challenging requirement to rapidly identify new materials and design nanostructures with extreme transport properties. As the limitations of traditional intuition-driven trial-and-error search methods become more prominent, machine learning (ML) and data informatics have emerged as powerful tools for solving these design and optimization problems. In thermal transport, ML methods have found success in predicting material properties and accelerating design of nanostructures with target thermal transport **we**2020**machine**, [62], [84], [85], [87], [208]–[211]. However, the applications of ML to solve thermal engineering problems till date have been limited to finding optimal solutions which confirm previously well understood phonon transport theory. ML has not yet been used to explore and discover exceptional solutions which can help us uncover new facets of phonon transport theory and guide the design of novel nanostructures. This can be attributed to the “interpolative” nature of traditional ML algorithms which allows for accurate prediction and exploration within the subspace spanned by known data points (and, therefore, known physics), but fails for excursions outside the training dataset. Consequently, suitable adaptations are needed to use ML methods in the identification of materials or nanostructures showing exceptional physical properties.

In this work, we demonstrate the potential of an adaptive machine learning approach to identify unexpected thermal transport behavior in aperiodic superlattices. Binary superlattices (SLs), composed of periodically alternating sections of two materials, have received widespread attention in the recent decades due to their lower thermal conductivity compared to the constituent materials [212]–[215]. The cross-plane lattice thermal conductivity in SLs can be modulated by variation of the average SL period. This makes them greatly attractive for applications such as thermoelectric devices[144], [154], [155], where a low thermal

conductivity is required to maintain a temperature gradient across the device. As a result, numerous experimental and theoretical studies have been performed to understand the nature of the underlying phonon transport across SLs. Phonons travelling along the cross-plane direction of SLs can exhibit particle-like behavior when anharmonic phonon-phonon scattering causes them to lose phase information before encountering an interface. On the other hand, multiple phase-preserved reflections at closely spaced periodic interfaces can lead to wave-like phonon transport characteristics. The transition from particle-like phonon transport (incoherent regime) at large SL periods to wave-like phonon transport (coherent regime) as the period is reduced leads to a minimum SL thermal conductivity, which has been predicted theoretically [47], [48], [213], [215] and recently observed experimentally [17], [54], [171], [216].

Recently, randomizing the constituent layer thicknesses in periodic SLs has been proposed as an efficient means to further reduce the thermal conductivity, even below the random alloy limit [55], [58]–[60]. In the resulting aperiodic superlattices or random multilayers (RMLs), destructive interference of coherent phonons due to reflections at the randomly spaced interfaces can cause their localization similar to Anderson localization of electrons, thereby limiting thermal transport by these long wavelength phonon modes [59], [61]. Naturally, many studies have been performed to uncover the influence of structural parameters, such as mass ratio [55], [58], average period [55], [59], [62], isotopic modulation [186] and interfacial mixing [55]–[57] on the thermal conductivity of RMLs. Due to the extremely large design space of imparting random perturbations to the layer thicknesses, the RMLs studied in these works have been generated randomly or from the intuition of domain experts. Moreover, studies using accelerated search algorithms have been performed to find the lower limit of RML thermal conductivity and the underlying phonon transport characteristics, by searching a subset of the entire RML design space [62], [87]. Machine learning algorithms such as Bayesian optimization and genetic algorithm search have allowed efficient identification of only the RML structures with ultra-low thermal conductivities, this mitigating the computational cost associated with the prohibitively large set of candidate structures.

Since the studies mentioned above aimed to gain insight into the lower limit of thermal conductivity of RMLs, the resulting structures generated have been found to reinforce

the accepted hypothesis that any manner of randomization of the layer thicknesses of the periodic SL causes reduction in thermal conductivity. However, such intuition-based explorations precludes the discovery of novel solutions which may be contrary to previous understanding. More specifically, it has not yet been elucidated whether certain random distributions of SL layer thicknesses can lead to higher thermal conductivity than that of the periodic SLs. If such RML structures showing enhancement of thermal conductivity do exist within the search space, the governing transport characteristics can uncover new facets of phonon transport theory and guide the design of novel nanostructures. Interestingly, Wei *et al.*[86] performed a similar search over the design space of 2D graphene nanomeshes different configuration of pores, where it is understood that randomness in pore spacings leads to a lower thermal conductivity due to localization of coherent phonons. Using a machine learning based search process, they demonstrated the existence of nanomeshes with disordered pore configurations which show higher thermal conductivity than that with uniformly spaced pores. Such demonstrations further drive the search to find exceptions for other well understood systems. However, the results from the search space already explored lead us to believe that such RMLs constitute a very low fraction of the design space, and a systematic approach is required to efficiently identify these low-probability-of-occurrence solutions.

Here, we identify RML structures with unexpectedly higher  $\kappa_l$  than corresponding SLs with same total length and average period. To accelerate the search over the prohibitively large design space, a convolutional neural network (CNN)-based prediction method is used for obtaining the  $\kappa_l$  of the candidate structures. An iterative approach is employed for generating a representative training dataset that enables the CNN to accurately predict the high  $\kappa_l$  of the target RML structures that are absent from the initial dataset. Finally, the identified non-intuitive RML structures are used to gain insight into the heat transport mechanisms leading to higher  $\kappa_l$  and its correlation with RML structural features. We find that the presence of closely spaced interfaces in RMLs with a large average period leads to an increased coherent phonon contribution, thereby causing lower interfacial thermal resistance. Our work describes a general purpose and efficient method to perform an accelerated search or optimization of nanostructure design, when the computational cost of individual simulations is high.

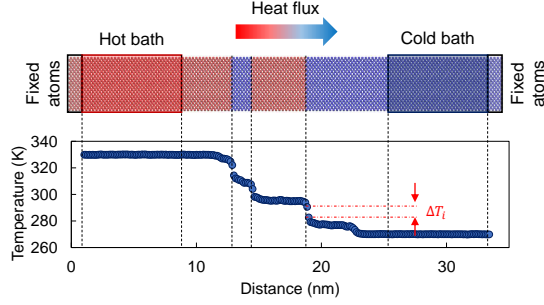


**Figure 5.1.** Schematic of the NEMD simulation setup showing the multi-layer nanostructure (SL or RML) sandwiched between two thermal baths. A layer of atoms is fixed at each end to impose fixed boundary conditions. The corresponding temperature profile is also shown.

## 5.2 Simulation methods

### 5.2.1 Non-equilibrium molecular dynamics simulations

Thermal conductivity calculations for the multilayered nanostructures are performed using non-equilibrium molecular dynamics simulations with the LAMMPS package [217]. The interatomic interactions are described using the three-body Tersoff potential [218], [219], which is commonly used to study vibrational properties of the Si/Ge system. The unequal equilibrium lattice constants of Si and Ge in these potential descriptions leads to a symmetric cross-sectional strain in the system, which can cause large oscillations at the interface regions [45]. To eliminate this strain, the lattice constant of Ge is artificially set to be equal to that of Si within the interatomic Tersoff potential parameters. A  $6 \times 6$  UC cross-section is used, which is sufficient to provide converged  $\kappa_l$  values. The thermal conductivity of the nanostructures is calculated at a temperature of 300 K. A timestep of 0.5 fs is used to integrate the equations of motion, which is sufficient to resolve the highest frequency of phonon vibrations in either material.

A schematic of the NEMD simulation domain for direct calculation of thermal conductivity is shown in Fig. 5.1. Two bulk material regions consisting of 20 UCs of Si and Ge are attached to either side of the SL or RML to act as thermal reservoirs. Initially, the entire system is relaxed for 500 ps at 300 K, under a constant pressure and temperature ensemble (NPT) with periodic boundary conditions applied to all three directions. Following this,

another 250 ps of equilibration under fixed volume and energy (NVE) is performed. Subsequently, non-equilibrium conditions are applied by thermostating the Si and Ge bulk regions on either side at 330 K and 270 K respectively, using Langevin thermostats. Two UCs of atoms at each end of the system are also kept fixed to mimic fixed boundary conditions along the heat transport direction. The system is allowed to reach steady state under this imposed temperature gradient over a period of 500 ps. Following this, the temperatures at equal intervals along the cross-plane direction are obtained by from the velocities of atoms in one-dimensional bins. The temperature and heat flux data is collected and averaged over a period of 4 ns. The cross-plane lattice thermal conductivity ( $\kappa_l$ ) is then calculated as

$$\kappa_l = \frac{q}{\Delta T/L} \quad (5.1)$$

Here,  $q$  is the steady state heat flux and  $L$  is the length of the SL or RML along the heat transport direction. The thermal boundary resistance at each interface of the system ( $R_i$ ) can also be calculated from the temperature drop across the interface ( $\Delta T_i$ ) as

$$R_i = \frac{\Delta T_i}{q} \quad (5.2)$$

### 5.2.2 Convolutional neural network-based prediction of thermal conductivity

While the NEMD simulations can provide accurate measures of thermal conductivity of the superlattice structures using a simple calculation framework, they are computationally expensive when more than hundreds of simulations need to be performed for a particular task. As a result, exhaustive searches using MD simulations over design spaces as large as the current problem become impractical. In such scenarios, the conventionally adopted approach is to use available “domain expertise” to search a subspace of the entire design space for candidates with target properties. However, this method falls short in case one wishes to search for solutions which are contrary to the previously understood knowledge,

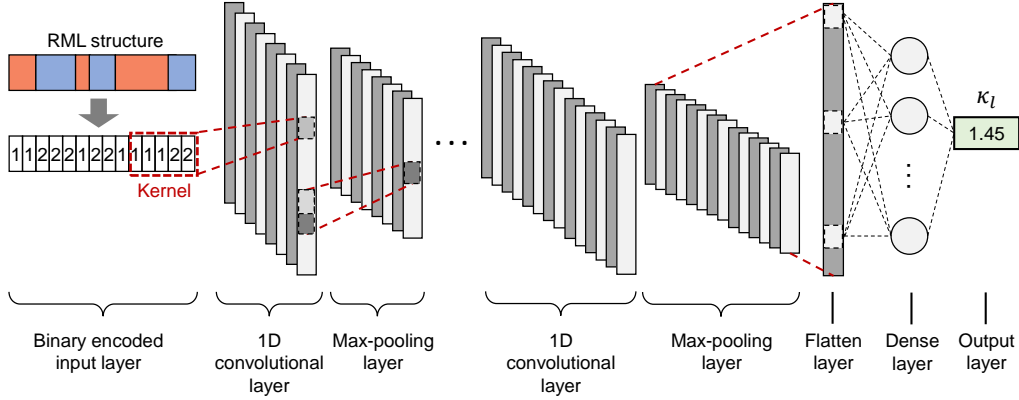


**Figure 5.2.** Schematic of the convolutional neural network architecture. The SL or RML structure is encoded as a binary array and used as the input layer. This is followed by a series of 1-D convolutional layers consisting of multiple feature kernels. A max-pooling layer is added to reduce the feature sizes. A flatten layer after the 1-D convolutional layers passes the features to a fully connected layer. The output layer consisting of a single node provides the predicted thermal conductivity.

and novel systematic methods must be considered to sample the search space. Moreover, using an intuition-guided explorative method can limit the search process to regions around a local optimum as opposed to the required globally optimum solution. This was highlighted in our previous work[62], where a manual search for the aperiodic superlattice with lowest thermal conductivity could not converge toward the structure with the globally minimum solution in the search space. In such cases, it is desirable to use search techniques that do not require previous intuition and, therefore, eliminates the possibility of confirmation bias. In particular, the use of machine learning techniques which can greatly accelerate property calculations, is considered in the context of the current problem.

With the advent of specialized computer hardware, highly parallelized computing environments and availability of large amounts of data, machine learning techniques have excelled in a variety of tasks involving data analysis, image processing and pattern recognition[220]–[224]. In particular, neural networks (NNs) have emerged as a powerful tool for regression and classification problems due to their ability to fit complex multifunctional datasets without the need for encoded sets of rules which may introduce human bias. As a result, they have been successfully used in several engineering problems, including predicting material proper-

ties and informed design of experiments for predicting nanostructures with targeted thermal transport properties[84], [85], [208]–[211]. Yang *et al.*[84] used a NN to predict the interfacial thermal resistance at a graphene-hexagonal boron nitride interface, with good agreement between predicted resistance and the values calculated from MD simulations. Chakraborty *et al.*[211] also used a neural network to predict the thermal conductivity of RML structures based on a Lennard-Jones system, and identify the structural disorder parameters influencing thermal conductivity in these structures. Convolutional neural networks (CNNs) are a class of NNs that have gained widespread popularity for their success in image and pattern recognition applications, particularly due to their translational invariance characteristics. An advantage of CNNs is their ability to form regression maps based on features extracted by the NN itself from input arrays or images. This allows CNNs to identify relevant structural features without the need for users to provide suitable descriptors, which would otherwise be a very challenging task. Wei *et al.*[85] trained a CNN to predict the effective thermal conductivities of composite materials using cross-sectional images as input data, while Rong *et al.*[210] used a similar method to obtain the thermal conductivities of 3D composites using 2D cross-sectional images.

The thermal conductivity of 1-D SLs and RMLs is governed by features such as number of interfaces and their spatial density and periodicity, which may be translationally invariant. Given these considerations, we chose to employ a CNN to predict the thermal conductivity from the multilayer structure. The architecture of the CNN used in this work is shown in Fig. ???. The input layer to the CNN is an N-bit array, corresponding to the number of UCs in the RML structure (20 or 40). Each bit can take a value of 1 or 2 depending on whether the corresponding UC at that location along the superlattice length consists of Si or Ge atoms respectively. This is followed by one or more one-dimensional convolutional layers, each of which consist of several kernels or filters to extract the relevant features from the input array by striding over the length of the input. Here, we use convolutional layers consisting of 44 – 50 filters with filter lengths of 5 – 9 bits, a stride length of 1 and no-padding. A max pooling layer is used after every two convolutional layers, which causes down-sampling of the identified features and incorporates translational invariance in the feature maps. After multiple convolutional layers, we use a flatten layer to reduce the

dimensionality of the features. Finally, a fully connected or dense layer consisting of 100 nodes is used to combine the identified features into a single output thermal conductivity value. Non-linearity is accounted for within the CNN by using a Rectified Linear Unit (ReLU) as the activation function throughout the network. For the 20 UC RML system, we use a CNN consisting of 2 convolutional layers, 1 max-pooling layer and 1 fully connected layer. On the other hand, for the 40 UC RML system where the number of input parameters is much larger, we switch to a CNN architecture consisting of 4 convolutional layers with 1 max-pooling layer after every 2 convolutional layers, and 1 fully connected layer as before.

The weights of the different layers are initiated randomly and need to be fit to the training data provided to the network. This is done by calculating a loss function over the entire training set and back-propagating the errors over the various layers of the network to minimize the loss. The loss function used to train our CNN is chosen to be the mean absolute percentage error (*MAPE*), given by

$$MAPE = \frac{1}{N} \sum_{i=1}^N \left| \frac{y_i - \bar{y}_i}{\bar{y}_i} \right| \times 100\% \quad (5.3)$$

Here,  $N$  is the number of training data points provided to the network,  $y_i$  is the predicted output and  $\bar{y}_i$  is the target output. Apart from the loss function, the root mean square error (RMSE) is also used as a metric to evaluate the performance of the network. We note that these metrics are most commonly associated with regression problems, instead of others such as accuracy which are convenient for classification tasks. The training of the network by back-propagation of errors is performed using the Adamax algorithm [225] and the fitting is performed over 300 – 500 epochs within which sufficient convergence of the loss function is observed. Overfitting of the data by the CNN, which is common occurrence in neural network training, is avoided using early stoppage of the fitting process if the testing loss is found to become constant or increase. Once the CNN is trained, it can be used to predict the thermal conductivities of the entire dataset of RML structures within several seconds, thereby making an exhaustive search possible. This is, of course, above the time required



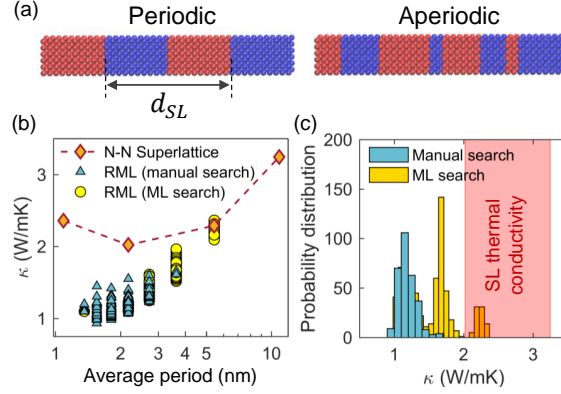


**Figure 5.3.** (a) Schematic of the Si/Ge periodic SL (left) and aperiodic SL or RML (right). (b) Variation of  $\kappa_l$  with average period at 300 K for RML structures generated during the manual random search (triangles) and the machine learning accelerated search (circles). The thermal conductivities of the reference  $N - N$  superlattices are indicated by the diamonds. (b) Probability distributions of thermal conductivities (W/mK) of the RML structures generated by a manual search (blue bars) and the ML search (yellow bars). The region spanned by the thermal conductivities of the  $N - N$  SLs is shaded in red.

to generate a representative training dataset containing a reasonable number of data points, which can be done systematically to a great advantage as explained in a subsequent section.

## 5.3 Results and discussions

### 5.3.1 Manual random search for higher thermal conductivity RMLs

We perform our calculations on the model Si/Ge system using non-equilibrium molecular dynamics simulations to search for high  $\kappa_l$  RML structures. This system has been extensively investigated in literature, given the wide application of these semiconductor materials as multilayer systems [45], [202], [203], [226]–[229] and the simplicity of performing molecular dynamics simulations using interatomic potential parameters. The SLs and RMLs are constructed by stacking the diamond cubic unit cells (UCs) of each material along the [100] direction. Two different lengths of SL and RML structures are studied in this work: a shorter 20 UC (11 nm) system and a longer 40 UC (22 nm) system. Periodic boundary conditions are maintained in the other two directions, so that our system results in a superlattice thin film. The smallest layer thickness allowed along the cross-plane heat transport direction

is set to be 1 UC, and only RMLs with equal number of Si and Ge layers are studied to ensure meaningful comparison of  $\kappa_l$  among all structures. Additionally, the first and last UCs along the RML length are constrained to be Si and Ge respectively, to prevent extra interfaces with the heat reservoirs. With these constraints imposed, the number of possible RML structures is found to be 48620 for the 20 UC system and 35345263800 for the 40 UC system. Figure 5.3(a) shows schematic images of representative periodic SL and RML structures.

First, we search for 20 UC (10 nm) RMLs showing enhanced  $\kappa_l$  from the corresponding SL structures. The thermal conductivities of the 20 UC  $N - N$  SL system are calculated, where  $N$  is the number of unit cells of Si or Ge in one period of the SL. To ensure an integral number of periods within the fixed total length of 20 UCs,  $N$  can take values of 1, 2, 5 and 10 only. The thermal conductivities obtained using NEMD simulations are shown in Fig. 5.3 (b), where a minimum of 2 W/mK is obtained at an SL period of  $\sim 2.2$  nm. This characteristic variation of  $\kappa_l$  with SL period has been predicted theoretically [47], [48], [213], [215] and recently observed experimentally [17], [54], [171], [216], and is commonly understood to be the result of the transition from coherent phonon to incoherent phonon dominated transport regimes. Phonons travelling along the cross-plane direction of SLs with large periods can exhibit particle-like behavior when anharmonic phonon-phonon scattering causes them to lose phase information before encountering an interface. On the other hand, multiple phase-preserved reflections at closely spaced periodic interfaces can lead to the formation of coherent phonon modes showing wave-like phonon transport characteristics. At periods greater than 2.2 nm, the interface density is small enough to ensure a low coherent phonon contribution. As a result, the reduction in incoherent phonon scattering by the SL interfaces leads to a greater thermal conductivity at higher periods. In contrast, when the SL period is below 2.2 nm, a significant portion of the thermal transport is contributed by the coherent phonon modes, which are no longer scattered by the closely spaced interfaces. In this regime, the increase of thermal conductivity at lower periods has been attributed to effects such as weaker band flattening and increased group velocities.

We then attempt the traditional *intuition-guided* search process to identify possible RMLs showing  $\kappa_l$  enhancement due to aperiodicity. Due to the absence of any previous evidence

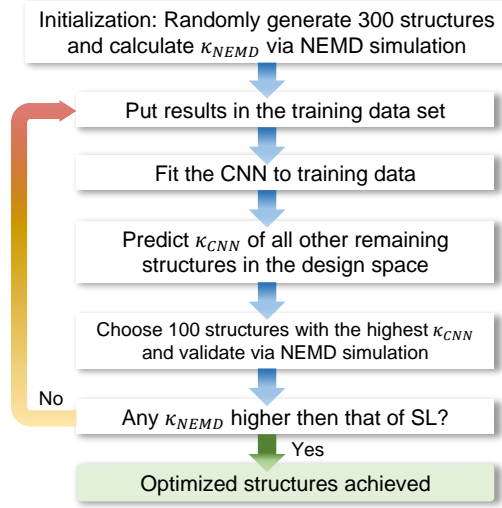


**Figure 5.4.** Schematic of the iterative search algorithm used to discover unexpected thermal conductivity ( $\kappa_l$ ) enhancement in aperiodic superlattice systems.

supporting the existence of enhanced  $\kappa_l$  RML structures, no guidance is available to narrow down the search to a computationally tractable subset of the design space. In this case, a random search can be considered to be one of the best possible search methods available. To perform the manual search, we randomly choose 300 candidate RML structures from the design space and calculate the thermal conductivities using NEMD simulations. The results of these calculations are compared with the SL thermal conductivities in Fig. 5.3 (b). We find, as expected, that all of the 300 randomly generated RMLs have significantly lower thermal conductivities than the corresponding SLs. We also calculated the histogram of thermal conductivity values for the 300 randomly generated RML structures as shown in Fig. 5.3 (c). It can be observed that the majority of RMLs have low thermal conductivities compared to the SLs. This shows the evident need for an alternative systematic and efficient way to perform the search and motivates the use of machine learning for such tasks.

### 5.3.2 Machine learning accelerated search for higher thermal conductivity RMLs

We next perform an accelerated search using a convolutional neural network for rapid thermal conductivity prediction. A well-known characteristic of neural networks is their

“interpolative” nature, *i.e.* they cannot generally be expected to extrapolate to unknown points outside the region spanned by the training dataset. This is problematic for our current objective, where the CNN is required to accurately predict thermal conductivities of high  $\kappa_l$  exceptional RMLs which are absent from the initial training dataset. To resolve this, we utilize the ability of CNNs to extract spatial features contributing to locally enhanced thermal transport. Although the training dataset is composed of RML structures with low to moderate  $\kappa_l$ , many of these structures contain spatial features that lead to locally enhanced thermal transport, such as large bulk regions or short regions of periodic interfaces. By forming feature-property maps from these structural features, the CNN is able to assimilate them and accurately predict the high  $\kappa_l$  of RMLs containing combinations of these favorable features. On the other hand, randomly sampling the design space does not automatically ensure inclusion of RML structures showing enhanced local thermal transport characteristics within the dataset. This can be seen from the probability distribution of thermal conductivities of the 300 randomly generated RML structures (Fig. 5.3 (c)), where the majority of RMLs have low thermal conductivities compared to the  $N-N$  SLs. In order to overcome this challenge, we adopt an iterative approach to generate our training dataset comprising RMLs with moderate to high thermal conductivities while performing the accelerated search. In the initial step, the CNN is trained on a dataset of the 300 randomly generated RMLs. The trained network is then used to predict the thermal conductivities ( $\kappa_{CNN}$ ) of all structures in the search space. Next, we select 100 RML structures predicted by the CNN to have the highest thermal conductivities and perform NEMD calculations of thermal conductivity ( $\kappa_{NEMD}$ ) to validate the CNN predicted values. If any of these 100 RML structures identified in the search show a higher  $\kappa_{NEMD}$  than the corresponding SL, the search is stopped with successful identification of the exceptional RML structures. Otherwise, these RML structures are included in the training data with their  $\kappa_{NEMD}$  values, and the CNN is retrained to fit the augmented data set. Subsequently, the thermal conductivities of all structures are again predicted (with potentially higher accuracy) and the algorithm is progressed in this manner. Figure 5.4 shows the complete work flow of the search algorithm followed in our work. In the initial iteration, the  $\kappa_{CNN}$  values are not expected to be accurate over the entire search space, given the relatively small size of the training dataset and the absence

of representative features. However, the accuracy of prediction improves as the size of the training dataset increases with each successive iteration and RMLs with high  $\kappa_l$  constitute a greater fraction of the training data.

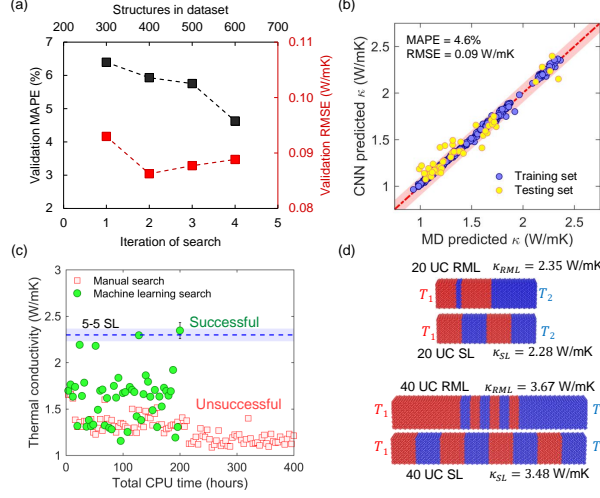


**Figure 5.5.** (a) Variation of testing MAPE (black squares, left axis) and RMSE (red squares, right axis) with each iteration of the iterative search process for the 20 UC RML system. The top axis indicates the size of the dataset on which the CNN is trained in that iteration of the search (b) Comparison of CNN predicted  $\kappa_l$  and NEMD calculated  $\kappa_l$  (true value) for the dataset of RML structures. The shaded area represents a  $\pm 0.1$  W/mK bound from  $y = x$ . (c) Thermal conductivities of 20 UC RMLs sampled by the random search (squares) and the CNN accelerated search (circles) with total computational time spent. The dashed line represents the  $\kappa_l$  of the 5-5 SL structure with error bounds. (d) The 20 UC and 40 UC RML structures with higher thermal conductivities than the corresponding SLs which were identified by the CNN accelerated search.

We first evaluate the performance of the CNN in predicting  $\kappa_l$  of the 20 UC RML system. Figure 5.5 (a) shows the variation of the MAPE and the RMSE with each iteration of the search process, when evaluated on a testing set of unknown RML structures not introduced to the CNN during training. We observe that the CNN is able to predict thermal conductivities with a very low MAPE varying from 4.6 – 6.4%, or an average RMSE of 0.09 W/mK. The MAPE generally decreases with each progressing iteration of the search due to the addition of more RML structures to the training dataset which increases the representative set of features. The comparison between the predicted ( $\kappa_{CNN}$ ) and “true” values ( $\kappa_{NEMD}$ ) is shown

by the parity plot in Fig. 5.5 (b) after training the CNN on data from 600 RML structures. It is seen that the CNN can provide accurate predictions over a wide range of thermal conductivities from 1 – 2.5 W/mK, thus demonstrating the capability of the CNN to extract suitable spatial features governing low and high  $\kappa_l$ . The progress of the ML enabled search for 20 UC RMLs with enhanced  $\kappa$  are shown in Fig. 5.5 (c), in comparison to a manually performed random search. We only compare RML structures against the corresponding SL having the same average period. As a result, the contribution of interface scattering of incoherent phonons to the thermal transport is the same in the compared multilayer structures, and any difference in  $\kappa_l$  is purely the result of coherent phonon transport. We find that our ML-based search process is able to identify RML structures with higher  $\kappa$  than the corresponding SL within two iterations of the search utilizing 200 CPU hours. In contrast, the manual random search returns far lower  $\kappa_l$  than periodic SLs even after double the simulation hours spent. The thermal conductivities of the RMLs scanned by the ML search process are plotted with respect to average period in Fig. 5.3 (b). By searching through RML structures with different average periods, the  $\kappa_l$  of RML structures are found to exceed the superlattice  $\kappa_l$  at a relatively higher average period of 5.4 nm, corresponding to the 5 – 5 SL. The identified RML  $\kappa$  of 2.36 W/mK is found to be higher than the SL  $\kappa$  of 2.28 W/mK by 3.5%, which is above the statistical uncertainty as confirmed by averaging these values over multiple independent runs. The structures of the 5 – 5 SL and the RML showing enhanced  $\kappa_l$  are shown in Fig. 5.5 (d).

We also perform a similar search for a larger RML system with a total length of 40 UCs. Since the number of possible RML structures for this system is several orders of magnitude larger than the 20 UC system, we limit our search to a tractable subset of the design space by using the knowledge gained from the results of the search on the 20 UC RML system. In particular, only RMLs with the relatively larger average period of 5.4 nm, corresponding to perturbations of the 5 – 5 SL, are sampled. With this constraint, the reduced design space consists of 938961 RML structures which can be efficiently handled by our ML search framework. Similar to the previous search process, the CNN accelerated search method can successfully identify an RML structure with higher  $\kappa$  than the corresponding SL within validation of 612 RMLs which constitute less than 0.1% of the design space. The identified

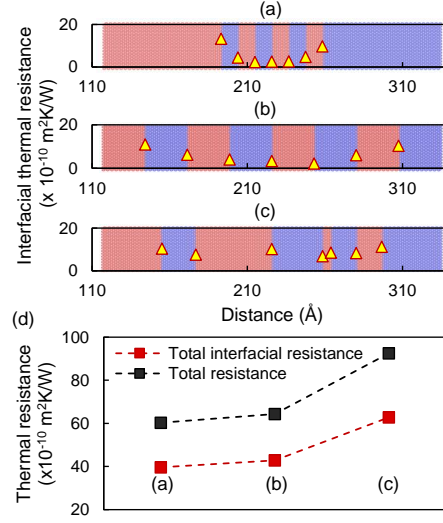


**Figure 5.6.** Calculated thermal resistances at all interfaces (yellow triangles) in three different 40 UC RML structures: (a) RML with high  $\kappa$  identified by the ML enabled search (b) 5-5 SL (c) RML with low  $\kappa$  identified by manual random search. The RML structures are underlaid for ease of visualization. (d) Comparison of the total interfacial thermal resistance (black squares) and total thermal resistance (red squares) for the three RML structures (a-c).

structure, shown in Fig. 5.5 (d), has a  $\kappa_l$  exceeding that of the SL by 5.5% which is also confirmed by averaging over multiple runs. Interestingly, the 40 UC RML structure identified by our search is found to be a composite SL which can be created by combination of the single interface structure and the shorter period 2 – 2 SL. As a result, the structure has the features of a local periodicity which enhances thermal transport despite having a globally random layer thickness distribution.

### 5.3.3 Contribution of interfacial resistance towards $\kappa_l$ enhancement

Finally, the identified exceptional RML structures shown in Fig. 5.5 (d) are studied to understand the underlying phonon transport characteristics leading to the disorder induced enhancement of  $\kappa_l$ . We observe the presence of small layer thicknesses due to closely spaced interfaces in these structures, which we attribute as the cause for the increased thermal transport. At an SL period of 5.4 nm, the relatively large layer thicknesses are above the coherence length of most phonons, as a result of which the contribution of coherent phonon

transport to the SL  $\kappa_l$  is quite low. However, the reduced thicknesses of some layers in the identified RMLs lead to an increased coherent phonon contribution, whereby the apparent thermal resistance of the interfaces are lowered. To verify our hypothesis, we calculated the total resistance across the RML as well as the contribution of the apparent interface resistances for three different 40 UC structures: (i) the RML with  $\kappa_l$  higher than the 5 – 5 SL identified through our search process, (ii) the 5 – 5 SL and (iii) a RML with low  $\kappa_l$  identified by the random search. The apparent interfacial thermal resistances at each of the interfaces in the RML structure are shown in Fig. 5.6 (a-c), superimposed on the visual representation of the RML structure. We can see that the compared to the 5 – 5 SL (Fig. 5.6 (b)), the apparent interfacial resistances are visibly reduced in the high  $\kappa$  RML (Fig. 5.6 (a)), which is the effect of a higher amount of coherent phonon transport. As a result, the RML shows a lower total interfacial thermal resistance and total thermal resistance than the SL, as seen in Fig. 5.6 (d). Finally, the localization of coherent phonon modes due to sufficient layer thickness randomization in the RML structure shown in Fig. 5.6 (c) and the absence of many closely spaced interfaces leads to a higher interfacial resistance and lower  $\kappa_l$ , which is in accordance to the previously accepted hypothesis. Our results indicate that randomness of layer thicknesses in SLs can be engineered to have dual effects via tuning the contribution of coherent phonons, which can either decrease or enhance thermal conductivities. Generally, in short period SLs, randomness can cause localization of coherent phonons and reduce  $\kappa_l$ . On the other hand, certain forms of aperiodicity in large period SLs can enable stronger coherent phonon transport that is not localized, thus enhancing  $\kappa_l$ .

## 5.4 Conclusions

In summary, we demonstrate a machine learning based approach for discovering nanostructures with non-intuitive thermal transport characteristics. Although it is generally accepted that randomization of layer thicknesses of a binary periodic superlattice lowers its cross-plane thermal conductivity, we aim to find structures showing the opposite trend, *i.e.* an enhancement of thermal conductivity due to disorder. Since no previous intuition is available to guide our search and given the extremely large design space, we first perform a



random search which fails to identify any RMLs showing thermal conductivity enhancement. Subsequently, we employ a convolutional neural network to rapidly predict the thermal conductivities of all RMLs in the design space. An iterative method is employed to dynamically generate the training dataset containing RMLs with moderate to high thermal conductivity, which helps the CNN learn the spatial features leading to locally enhance phonon transmission in the RML structures. The results show that our CNN accelerated search is able to identify RML structures with higher thermal conductivity than the superlattice at an average period of 5.4 nm. By analysing the identified optimal and suboptimal structures, we attribute the enhanced RML thermal conductivity to an increase in coherent phonon contribution at closely spaced RML interfaces as compared to the SL, thus causing lower interfacial resistance in the RMLs. Our results demonstrate the ability of machine learning based methods to help discover expectations and low-probability-of-occurrence solutions in a large search space. The general purpose neural network based method used in this work can be applied to several other tasks as well, such as identification of ideal interface configurations in RMLs or stacking configuration of 2D heterostructures for optimized thermal transport.

## 6. MACHINE LEARNING OPTIMIZED APERIODIC SUPERLATTICES WITH HIGH REFLECTIVITY FOR THERMAL BARRIER COATINGS

### 6.1 Introduction

The design of thermal barrier coatings (TBCs) for high temperature applications is extremely important in order to keep pace with the demand for higher efficiency operation of turbine engines and power generators. For example, although the efficiency of gas turbines can be increased by raising the turbine inlet temperature, this is severely limited by material considerations that provide an upper limit of temperature above which thermal degradation can occur. Thermal barrier coatings play a crucial role in preventing the turbine blades and rotors from reaching extremely high temperatures and mitigating the limitations imposed by the mechanical and thermal stability of the constituent materials. Since TBCs are responsible for retarding the transport of heat to the metallic turbine components, TBC materials are required to have low thermal conductivity and high melting points, which are commonly observed in ceramic materials such as yttria stabilized zirconia (YSZ). In the past decades, significant efforts have been made to design improved TBC materials which can provide better thermal insulation at a lower coating thickness, which reduces the parasitic mass load for rotating turbine components.

Heat transport to the metallic substrate through the TBC can take place via two pathways: heat conduction through phonons and thermal radiation through photons. At low temperatures, the heat transport is dominated by phonon mediated heat conduction and radiation effects are small. Consequently, much effort has been devoted to design materials and microstructures with low lattice thermal conductivity[230]–[235]. On the other hand, at higher temperatures, heat transport by radiation can lead to a significant temperature increase of the metallic substrate, even as high as 50°C[15]. Thermal transport due to radiation can become the dominant mechanism if the TBC material is transparent in the peak wavelengths of the irradiation, which is shifted to lower wavelength values at high temperatures according to the Wien’s displacement law. For example, it has been shown that YSZ

has a high transmittance to radiation in the wavelength of  $0.3 - 5\mu\text{m}$ [236], which accounts for 90% of the total blackbody irradiation at  $T = 1500\text{K}$ . As a result, TBC systems need to incorporate both phonon and photon scattering mechanisms for efficient thermal isolation at high temperatures. Similar to strategies for lowering lattice thermal conductivity by enhancing phonon scattering, several methods have been investigated to enhance photon scattering in TBCs for increased reflectivity to the incoming thermal radiation. Wolfe *et al.*[237] studied the performance of  $\text{ZrO}_2 - 8 \text{ wt. } \% \text{ Y}_2\text{O}_3$  (8YSZ) whose microstructure was modulated by periodic strain fields, and found that the hemispherical reflectance was increased by 28 – 56%. One of the effective methods to reduce photon transmission is the use of multilayered and functionally graded TBCs. Such systems can overcome the limitations imposed by the thermophysical and optical properties of a single material, as well as enhance photon and phonon scattering at multiple interfaces within the system. Most studies in literature on such multilayered TBC systems have focused on the fabrication[238], [239], mechanical characterization[240] and failure analysis[238], [239], [241]. Kelly *et al.*[242] reported a 73% infrared reflectance maximum at  $1.85\mu\text{m}$  and an overall increase in reflection spectrum from 1 to  $2.75\mu\text{m}$  in multilayer 7YSZ- $\text{Al}_2\text{O}_3$  TBC coatings. Huang *et al.*[243] designed and analyzed a system of similar constituent materials, where 7YSZ- $\text{Al}_2\text{O}_3$  multilayer stacks of varying layer thicknesses were used to achieve broadband photon scattering and high reflectivity. Ge *et al.*[244] fabricated and studied the radiative transport properties of YSZ/NiCoCrAlY duplex TBCs and multilayered functionally graded TBCs with varying multilayer structures, porosities and thicknesses. They found a negligible transmittance for the majority of YSZ/NiCoCrAlY functionally graded TBCs studied, with the top YSZ layer having a strong influence on the overall reflectance. Despite the superior performance of these materials, they cannot be readily used at temperatures in excess of  $1500^\circ\text{C}$  due to limitations of thermal stability. As a result, such high temperature applications require the development of novel TBC materials and systems which can efficiently limit heat transport by conduction and radiation, as well as show significant resistance to thermal degradation.

It is evident that multilayered TBC systems can exhibit superior performance in inhibiting both phonon and photon heat transfer. However, the process of development of such multilayered systems has largely been empirical and driven by experimental trial-and-error

studies. Moreover, a large number of candidate materials and several design parameters such as individual layer thicknesses and stacking order of the constituent materials lead to a huge design space for multilayered TBC systems which cannot be efficiently searched using these traditional methods. In such problems, machine learning (ML) and materials informatics (MI) are an attractive and even indispensable tool in driving design optimization and discovering novel physical phenomena. ML and MI-based optimization methods, coupled with accurate yet inexpensive numerical simulations to evaluate candidate solutions, have been recently adopted to solve thermal transport engineering problems with great success, such as accelerating design of nanostructures with target thermal transport properties[62], [84]–[87], [211]. For example, a design optimization of 1 –  $D$  aperiodic superlattices (SLs) showing ultra-low lattice thermal conductivity was performed using a Bayesian Optimizer by Ju *et al.*[87] and using a Genetic Algorithm in one of our previous works[62]. Novel insights into the phonon transport mechanisms in these structures, including the role of phonon localization, was uncovered from the results of the MI-based optimization. MI methods have also been used to optimize nanostructure design for target radiative transport properties, notably for the design of selective emitters for radiative daytime cooling[245]–[247]. The great success achieved by ML and MI methods in the above studies encourages us to employ such methods for the design optimization of multilayered and functionally graded TBC systems.

In this work, we demonstrate the performance of  $\text{CeO}_2$  and  $\text{MgO}$ -based periodic and aperiodic superlattice (SL) multilayer systems as high temperature TBCs with high reflectivity to thermal radiation. We choose these candidate materials due to their good thermal stability at the high temperature considered here, as well as their closely matched lattice structures which can enable growth of high quality crystalline structures with perfect interfaces. Using a Genetic Algorithm (GA) optimization process, we are able to identify random multilayer (RML) structures with total thicknesses of  $5 - 30\mu\text{m}$  that can reflect  $\sim 60 - 93\%$  of the blackbody radiation at  $T = 1500\text{K}$ . The spectral reflectivity and transmittance of each candidate structure is calculated using the transfer matrix method. First, we calculate the reflectance of periodic  $\text{CeO}_2$ - $\text{MgO}$  SLs with varying total and average layer thicknesses, and identify the occurrence of an optimal average layer thickness at which the total reflectivity is maximized. The effect of randomness is studied by manually providing varying degrees of

perturbation to the individual layer thicknesses, which causes localization of photons. Next, we employ our GA based optimization process on multilayer systems with total thickness varying from  $5 - 30\mu\text{m}$ . The GA-optimized structures show a broadband high reflectivity in the wavelengths coinciding with the peak blackbody radiation at the desired temperature. Moreover, our automated GA optimization framework is able to identify such high reflectivity RML structures by performing evaluations for only a small number of candidate structures in the design space, and does not require any previous intuition as input, which also removes the possibility of human bias adversely influencing the search process.

## 6.2 Simulation methods

### 6.2.1 Materials and multilayer structures

We study multilayer structures composed of  $\text{CeO}_2$  and  $\text{MgO}$ , which are chosen due to the large contrast in their refractive index, high melting points for thermal stability in high temperature TBC applications and their closely matched lattice structures. A schematic of a representative multilayer structure with  $N$  layers is shown in Fig. 6.1(a). The layer thicknesses can periodically alternate to form a superlattice (SL) or may be randomly chosen to form a random multilayer (RML). The total thickness of the systems studied in this work range from  $5 - 50\mu\text{m}$  and the shortest thickness of each individual layer is allowed to be  $10\text{nm}$ . We also assume perfectly smooth interfaces to exist between  $\text{CeO}_2$  and  $\text{MgO}$  layers.

The complex refractive indices of  $\text{MgO}$  and  $\text{CeO}_2$  are obtained from literature. The refractive indices of  $\text{MgO}$  crystal was measured by Stephens and Malitson [248] for the wavelengths of  $0.36 - 5.35\mu\text{m}$ , while those of  $\text{CeO}_2$  were measured for wavelengths of  $0.25 - 1.09\mu\text{m}$  by Guo *et al.* [249]. The refractive index at higher wavelengths till  $8\mu\text{m}$  were obtained using a simple linear extrapolation, which enables us to approximate the total reflectivity integrated over the blackbody spectrum as defined in the subsequent section. We note that the measured refractive index values were obtained at room temperature, which may be different from those at the higher temperatures which are considered in this work. However, we expect that use of lower temperature optical properties will be sufficient to capture the relative differences in reflectivity between the different multilayer structures considered.

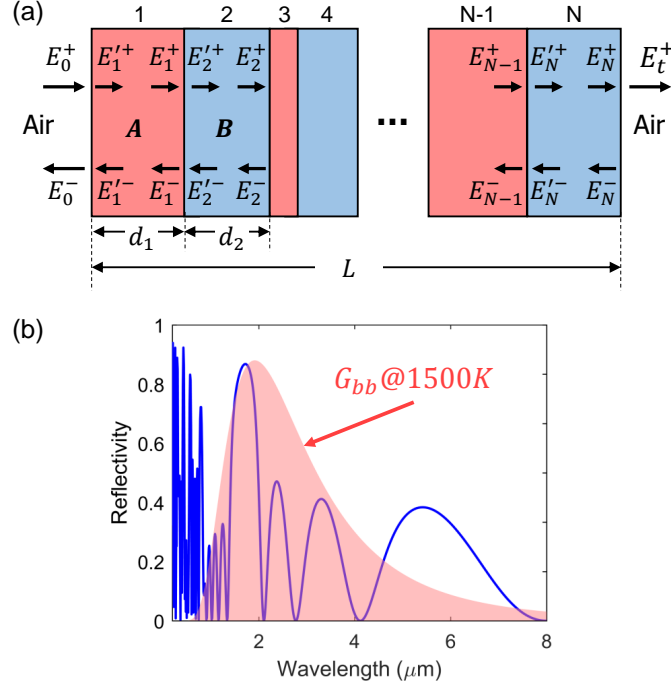


**Figure 6.1.** (a) Schematic of the multilayer system with total length  $L$ , composed of  $N$  layers with thicknesses  $d_1, d_2, \dots, d_N$ . The field amplitudes within each layer are shown, along with the incident and final transmitted fields. (b) A representative plot of spectral reflectivity vs. wavelength for a multilayer system. The shaded plot in the background represents the shape of the black-body radiation spectrum at  $T = 1500\text{K}$ .

### 6.2.2 Transfer matrix method

The reflectance and transmittance of a one-dimensional multilayer structure can be evaluated using the transfer matrix method, which solves the Maxwell's equations subject to a uniform normal electric field  $\mathbf{E}$ . Within the multilayer system, the field  $E_i$  is composed of its forward (transmitted) component  $E_i^+$  and its backward (reflected) component  $E_i^-$ . The schematic of the multilayer system with the field components is shown in Fig. 6.1(a). We use the convention of naming the fields at the left end of each layer as  $E_i^+$  and  $E_i^-$  and those at the right end as  $E_i^+$  and  $E_i^-$ . The field components on each end of a layer of material A, with complex refractive index  $m_A$ , are related by:

$$\begin{bmatrix} E_1^+ \\ E_1^- \end{bmatrix} = \begin{bmatrix} e^{ik_A(d_A)_1} & 0 \\ 0 & e^{-ik_A(d_A)_1} \end{bmatrix} \begin{bmatrix} E_1^+ \\ E_1^- \end{bmatrix} = (\mathbf{P}_A)_1 \begin{bmatrix} E_1^+ \\ E_1^- \end{bmatrix} \quad (6.1)$$

Here,  $(d_A)_1$  is the thickness of the 1st layer composed of material A (as an example),  $k_A = 2\pi m_A/\lambda_0$  is the wave number and  $\lambda_0$  is the wavelength in vacuum. At any interface between two materials A and B with complex refractive indices  $m_a$  and  $m_b$  respectively, the field components on either side are related by the equation

$$\begin{bmatrix} E_1^+ \\ E_1^- \end{bmatrix} = \begin{bmatrix} \frac{m_B+m_A}{2m_A} & \frac{m_B-m_A}{2m_A} \\ \frac{m_B-m_A}{2m_A} & \frac{m_B+m_A}{2m_A} \end{bmatrix} \begin{bmatrix} E_2^+ \\ E_2^- \end{bmatrix} = \mathbf{I}_{12} \begin{bmatrix} E_2^+ \\ E_2^- \end{bmatrix} \quad (6.2)$$

Equations 6.1 and 6.2 can be written for all  $N$  layers in a multilayer system, and the field components at the boundaries of the multilayer can be related using the equation:

$$\begin{bmatrix} E_0^+ \\ E_0^- \end{bmatrix} = \mathbf{I}_{01}(\mathbf{P}_A)_1 \mathbf{I}_{12}(\mathbf{P}_B)_2 \mathbf{I}_{23} \dots \mathbf{P}_N \mathbf{I}_{N(N+1)} \begin{bmatrix} E_t^+ \\ 0 \end{bmatrix} \quad (6.3)$$

For a given value of the incident field  $E_0^+$ , Eq. 6.3 may be solved for the reflected field component  $E_0^-$  and the transmitted field component  $E_t^+$ . One can then obtain the spectral reflection and transmission coefficients from the relations:

$$R(\lambda) = \left| \frac{E_0^-}{E_0^+} \right|^2 \quad (6.4)$$

$$T(\lambda) = \left| \frac{E_t^+}{E_0^+} \right|^2 \quad (6.5)$$

In order to evaluate the relative performances of the different multilayer structures studied, we calculate the total reflectivity using the blackbody radiation spectrum at 1500K, which is representative of the thermal irradiation encountered in the proposed applications of these multilayer structures as high temperature TBCs. Although the spectral properties can provide insight into the physical behavior of these systems, an integrated scalar value of reflectivity is required for evaluating a standardized optimization objective function as defined in a later section. The total reflectivity is calculated as:

$$R_{total} = \frac{\int R(\lambda)G_{bb}(\lambda, T = 1500)d\lambda}{\int G_{bb}(\lambda, T = 1500)d\lambda} \quad (6.6)$$

where the blackbody radiation  $G_{bb}$  at a temperature  $T$  is given by:

$$G_{bb}(\lambda, T) = \frac{2\pi hc^2}{\lambda^5} \frac{1}{e^{\frac{hc}{k_B \lambda T}} - 1} \quad (6.7)$$

Here,  $h$  is the Planck constant,  $c$  is the speed of light in vacuum and  $k_B$  is the Boltzmann constant. Figure 6.1(b) shows a representative spectral reflectivity curve with the shaded curve representing the blackbody radiation spectrum at 1500K.

### 6.2.3 Genetic Algorithm optimization of multilayer structure

In order to find the random multilayer configuration with the highest reflectivity, we employ a Genetic Algorithm (GA) optimizer, which is an evolutionary algorithm that mimics the principle of natural selection to find the optimal solution. Since the GA is not a gradient-dependent optimization process, it works well for problems involving a complex response surface since GA can avoid getting trapped within a region of local optimum. Moreover, GA's are found to have superior performance compared to other gradient-based optimization problems when the number of optimization variables is large, and candidate evaluations within each iteration can be parallelized to reduce computational time. In a GA based optimization, candidate solutions within the design space are encoded as individuals



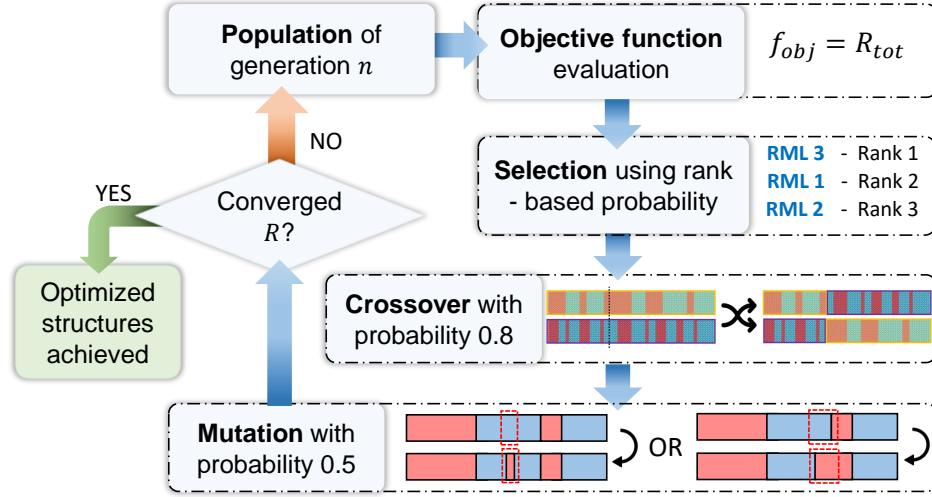


**Figure 6.2.** (a) Schematic of the Genetic Algorithm (GA) based optimization process, showing the implementation of the selection, crossover and mutation steps.

or *phenotypes* with properties represented as *chromosome* strings which are altered by evolutionary operations. The GA is started with an initial set of encoded individuals called a *population*, which may be chosen randomly or using any prior knowledge available about the design space. The set of individuals in each iteration are called a *generation*. In each iteration, the individuals in that generation are evaluated with respect to a suitably designed objective function, and a *fitness value* is assigned to the individual based on this evaluation. In the next step, a new population of parents is formed by probabilistic *selection* from the current generation, where individuals with high fitness value have higher probability of being selected. This step ensures that only the best properties or *genes* in the each generation are propagated to the next generation, thus leading the generation towards better fitness individuals. Subsequently, the evolutionary operations of *crossover* and *mutation* are performed to breed a new generation from the selected population of high-fitness parents. Crossover (or recombination) is performed by choosing a pair of individuals from the parent pool and stochastically combining genes from these parents to form two new offspring. On the other hand, mutation introduces genetic diversity in a single offspring by altering the value of one or more randomly selected genes which can introduce candidate solutions from unexplored regions of the design space. Both these operations are performed with a probability

of occurrence which needs to be suitably chosen to ensure a balance between exploration of new solutions and exploitation of already explored solutions. A new generation of candidate solutions is obtained after performing the operations of selection, crossover and mutation which is then progressed to the next iteration of the GA. To stop the GA, a convergence criteria can be set such as a target fitness value or a relative change in fitness value over several successive generations.

In the current work, we encode the periodic and random superlattices as  $N$ -bit binary arrays, where each bit in the array represents the type of material for a 10 nm thick layer at the corresponding position along the length of the superlattice. Each bit in the array is encoded as 1 if the corresponding position consists of a  $\text{CeO}_2$  layer or 2 if it consists of a  $\text{MgO}$  layer. It is to be noted that following this implementation, each individual in the solution space is composed of  $N$  chromosomes, each of which is a categorical variable taking values 1 or 2. The design space consists of  $2^N$  possible solutions for a superlattice system of  $10 \times N$  nm total thickness. A population size of 1000 is chosen for all thicknesses (and, thus, number of variables in the GA) studied. Since we are aiming to identify the superlattice structure with the highest reflectivity, the objective function is chosen as the total reflectivity calculated using the transfer matrix method as described in the previous section. The evaluation of reflectivity for each candidate structure using the transfer matrix method is very fast, and can be run in parallel to other candidates in the generation on our high-performance computing cluster. The initial generation is populated by randomly generating superlattice structures, while also ensuring that the entire range of average periods possible is represented in the population. The selection process implemented here is a rank-based selection, where the probability of an individual to be selected as for the parent pool is inversely proportional to the rank of the individual when the entire population is sorted in decreasing order of the objective function. The probability of selection is given by the expression

$$P(i) \propto \frac{1}{c + \text{rank}(i)} \quad (6.8)$$

where  $c$  is a parameter that can be adjusted to control the selectivity of best-fit individuals. After selection of the parent pool, crossover and mutation are performed with probabilities of 0.8 and 0.5 respectively, i.e. they are performed 80% and 50% of the time. We implement a single-point crossover, in which a random position is chosen along the  $N$ -bit binary arrays of two parents and the sections of the arrays succeeding the chosen position are interchanged between the two parents to form the two new offspring. The mutation operation is performed in one of two ways which can occur with equal probability: (i) a single bit is chosen along the  $N$ -bit array of the offspring, and its value of the variable is flipped (1 to 2 or vice-versa) to change the material occurring at that location, or (ii) a random layer (group of bits with the same value) is chosen and its length is increased or decreased randomly (the length of the adjacent layer is decreased or increased correspondingly to ensure the total thickness of the structure is preserved). The first method of mutation serves to perturb the number of interfaces in the structure, while the second method provides random perturbations to the layer thicknesses. Figure 6.2 provides a schematic of the GA optimization process, including the implementation of selection, crossover and mutation operations.

### 6.3 Results and discussions

#### 6.3.1 Reflectivity of multilayer structures and effect of randomness

We first evaluate the reflectivity of  $\text{CeO}_2$ - $\text{MgO}$  based periodic superlattice multilayer structures using the transfer matrix framework as described previously. The main structural features which can be varied in these SL structures are the total thickness  $L$  and the repeating layer thicknesses  $d_{\text{CeO}_2}$  and  $d_{\text{MgO}}$ . Here, we only consider SLs with equal layer thicknesses of  $\text{CeO}_2$  and  $\text{MgO}$ , i.e. the SL has a repeating period of  $2d$ . Moreover, the total thickness  $L$  is constrained to be integral multiples of the repeating period. Figure 6.3(a) shows the total reflectivity of SLs with varying total thickness from  $1 - 50\mu\text{m}$  and average individual layer thickness ranging from  $10\text{nm} - 1\mu\text{m}$ . The plots for each total thickness show a similar trend where the total reflectivity initially increases with the average layer thickness and eventually reaches a peak reflectivity value, following which a decrease in reflectivity is observed. To understand the reason behind this trend, we compared the spectral reflectivity plots of

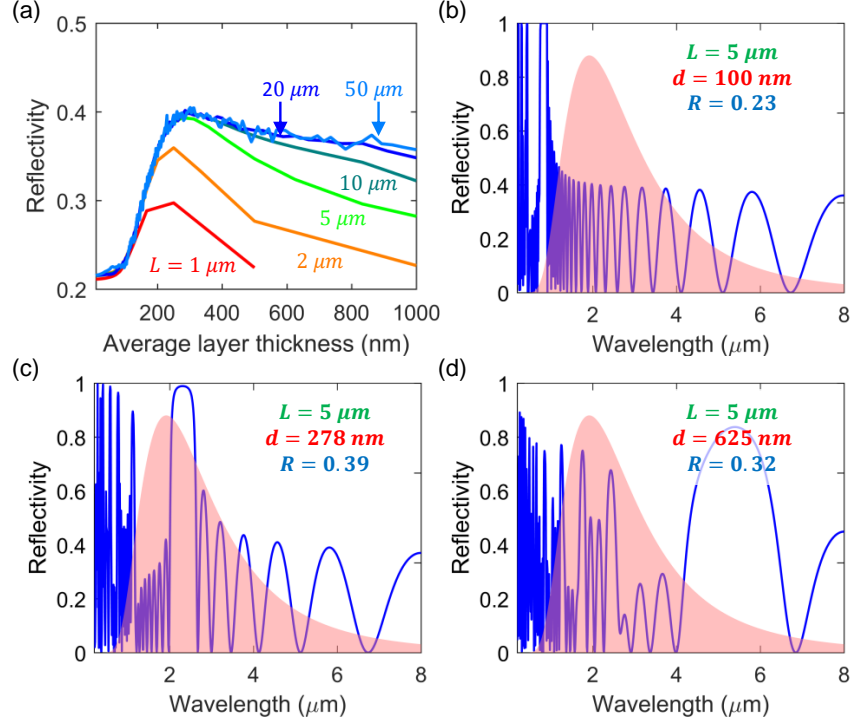


**Figure 6.3.** (a) Variation of total reflectivity with average layer thickness for  $\text{CeO}_2\text{-MgO}$  periodic superlattice (SL) structures for total thicknesses of  $1 - 50 \mu\text{m}$ . The spectral reflectivity vs. wavelength is shown for three different structures with total thickness of  $5 \mu\text{m}$  and average layer thickness of (b)  $d_{\text{avg}} = 100 \text{ nm}$ , (c)  $d_{\text{avg}} = 278 \text{ nm}$  which gives the highest reflectivity among SLs with total thickness of  $5 \mu\text{m}$ , and (d)  $d_{\text{avg}} = 625 \text{ nm}$ . The shaded plot in the background represents the shape of the blackbody thermal radiation spectrum at  $T = 1500 \text{ K}$ .

SLs with total thickness of  $5 \mu\text{m}$  and three different average layer thicknesses as shown in Fig 6.3(b)-(d). In all three cases, we observe the existence of strong oscillations in the spectral reflectivity, obtained from constructive and destructive interference due to multiple phase-preserved reflections at the different interfaces in the multilayer structure. We also notice the existence of a high reflectivity photonic “stopband” in each of the structures which is similar to that observed in distributed Bragg reflector systems. The wavelength at which this stopband occurs is found to vary with the average layer thickness of the structure, and coincides with the location of the peak blackbody thermal radiation spectrum (shown by the

shaded plot in the background) at an average SL layer thickness of 277.78 nm, which leads to the peak reflectivity at this layer thickness.

The total reflectivity of SLs with a fixed average layer thickness also shows an initially increasing trend with increasing total thickness of the system. This can be seen in Fig. 6.3(a), where the reflectivity at a constant average layer thickness increases from  $L = 1\mu\text{m}$  to  $L = 20\mu\text{m}$ . For higher total thicknesses, the reflectivity does not show an increasing trend, and can even decrease slightly, as evident from the lines corresponding to  $L = 20\mu\text{m}$  and  $L = 50\mu\text{m}$ . Moreover, the increase in reflectivity with increasing total thickness is more significant at average layer thicknesses greater than 200nm. The trend of increasing reflectivity with increasing total thickness at these average periods can be attributed to the increase in the number of interfaces within the SL structure at larger thicknesses, causing more high reflectivity peaks to appear within the range of incident wavelengths due to greater number of repeated reflections.

Next, we evaluate the effect of randomization of layer thicknesses on the reflectivity of superlattice structures. In providing such randomness to the SL layer thicknesses, we ensure that the total multilayer thickness as well as the total thickness of each constituent material are conserved. To quantify the degree of randomness in a random multilayer structure, we use the standard deviation of the layer thickness perturbations as a percentage of average layer thickness, which is calculated as:

$$\delta = \frac{\sqrt{\frac{\sum_{i=1}^N (\Delta_i - \bar{\Delta})^2}{N-1}}}{d_{avg}} \times 100\% \quad (6.9)$$

where,  $\Delta_i$  is the deviation of the  $i^{th}$  layer thickness of the  $N$ -layer RML from the corresponding SL layer thickness, and  $\bar{\Delta} = 0$  for conservation of total thickness of the constituent materials. We note that such a definition of degree of randomness does not uniquely specify a RML structure, since the relative positions of the layers does not affect  $\delta$  at all. As a result, there may still be significant variation of reflectivity among structures with the same total thickness, average layer thickness and degree of randomness. To account for this, we

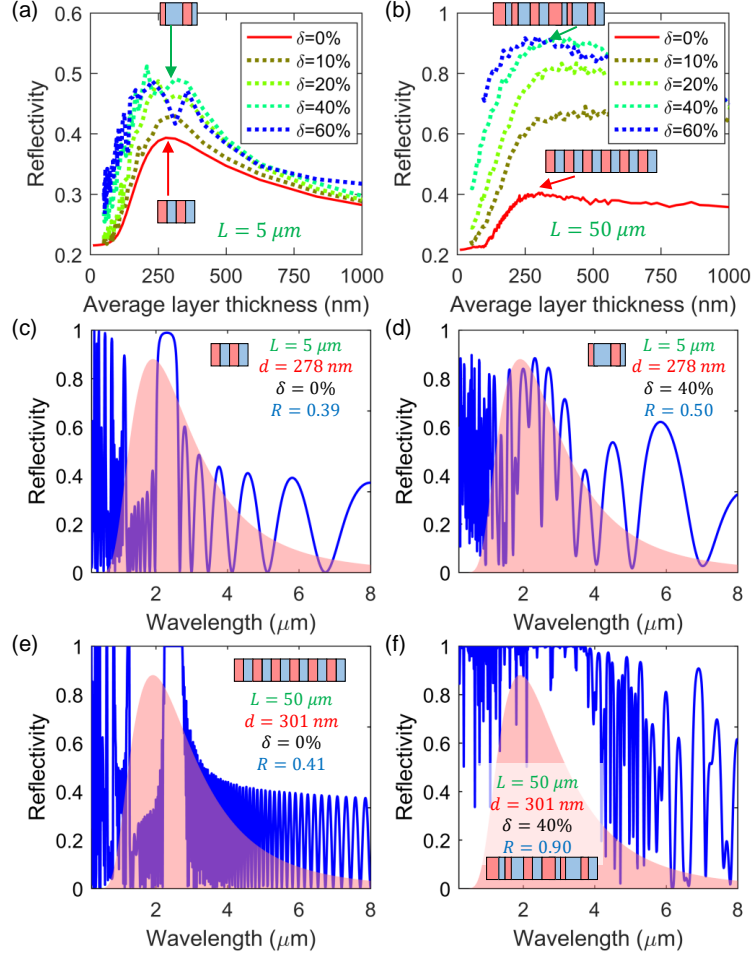


**Figure 6.4.** Total reflectivity vs. average layer thickness, showing the effect of randomizing the superlattice layer thicknesses by  $\delta = 10, 20, 40$  and  $60\%$ , for two total thicknesses of (a)  $L = 5 \mu\text{m}$  and (b)  $L = 50 \mu\text{m}$ . The spectral reflectivity vs. wavelength is plotted for comparison between two  $5 \mu\text{m}$  structures with (c)  $\delta = 0\%$  (perfectly periodic) and (d)  $\delta = 40\%$ ; and for two  $50 \mu\text{m}$  structures with (e)  $\delta = 0\%$  (perfectly periodic) and (f)  $\delta = 40\%$ . The shaded plot in the background represents the shape of the blackbody thermal radiation spectrum at  $T = 1500\text{K}$ . (Inset multilayer structures are for visual aid only and do not represent the actual structures)

generate three independent random structures at each average layer thickness and degree of randomness, and choose the maximum total reflectivity value among the three RMLs for the corresponding data point.

Figures 6.4(a) and (b) show the effect of randomization of superlattice layer thicknesses on the total reflectivity for two total thicknesses of  $5\mu\text{m}$  and  $50\mu\text{m}$  respectively. For both cases, the total reflectivity is found to increase with increasing degree of randomness upto  $\delta \sim 40\%$ , after which a non-monotonic fluctuation is observed. While the maximum reflectivity observed in the periodic structure without randomness is 0.39 and 0.40 for  $5\mu\text{m}$  and  $50\mu\text{m}$  thick superlattices respectively, the addition of randomness can increase the reflectivity to 0.51 and 0.92. The reflectivity vs. wavelength is compared between a periodic and random structure (with  $\delta = 40\%$ ) for  $5\mu\text{m}$  and  $50\mu\text{m}$  total thicknesses in Fig. 6.4(c)-(d) and Fig. 6.4(e)-(f) respectively. It can be seen that the randomization of layer thicknesses causes an overall increase of the reflectivity peaks in the spectral reflectivity plot, implying a low transmission in these structures. This effect can be attributed to the randomness-induced localization of photons, similar to Anderson localization of electrons[250], and has been studied theoretically and experimentally in similar  $1 - D$  disordered systems[251]–[253]. The phase-preserved reflections occurring at the randomly distributed interfaces within the RML can cause constructive and destructive interference in a manner that the field is enhanced in and confined to certain finite spatial regions.

### 6.3.2 Genetic Algorithm based optimization of multilayer structure for high reflectivity

As mentioned previously, for a fixed average layer thickness and degree of randomness, there may exist a large number of possible values and spatial distributions of layer thicknesses, each leading to a different “realization” of a RML structure. Considering a smallest allowable individual layer thickness of  $10\text{nm}$ , the number of possible RML structures for a total thickness of  $L\mu\text{m}$  is  $2^{100L}$ . With increase in the total thickness of the structure, the size of the design space containing all possible realizations increases exponentially, and cannot be covered comprehensively by an exhaustive or even intuition-guided search. Moreover, our simulation results on a small number of realizations for fixed total thickness, average layer

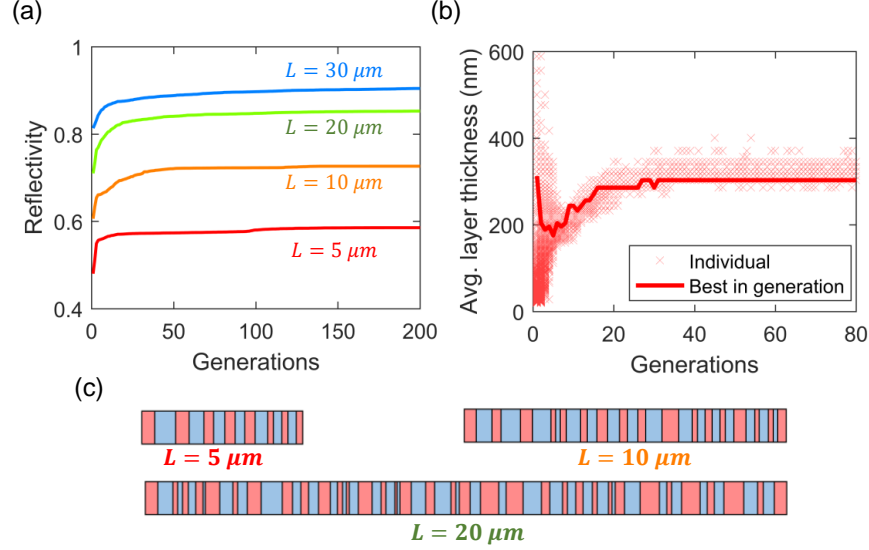


**Figure 6.5.** (a) Evolution of maximum reflectivity identified by the genetic algorithm (GA) optimizer vs. generation of optimization, for four different total thicknesses of 5, 10, 20 and  $30 \mu m$  (b) The average layer thicknesses of all individuals in the population (red crosses) at each generation of the GA optimization run for a total thickness of  $10 \mu m$ . The solid line shows the average layer thickness of the RML with highest reflectivity at each generation of the optimization process. (c) Design of the GA-optimized RML structures with high reflectivity for three total thicknesses of 5, 10 and  $20 \mu m$ .

thickness and degree of randomness show that a significant variation in total reflectivity can exist between these different structures. It is evident that in order to efficiently scan the design space for high reflectivity RML structures with a target total thickness, an alternative approach such as an automated and data-driven optimization method is necessary and can greatly benefit the current problem.

Here, we use a genetic algorithm optimization process to search for RML structures with high reflectivity. Figure 6.5(a) shows the evolution of the maximum reflectivity among all structures in each generation of the GA optimization, for the different total thicknesses studied in this work. In each case, the initial population was created with a large range of average layer thicknesses in order to promote sufficient diversity among the individuals and not provide any inherent bias to the optimization process. The maximum reflectivity for each run is found to increase from an initially lower value, corresponding to the expected



range of reflectivities obtained if an RML was randomly generated, and converge to a much higher reflectivity after a number of generations. The maximum reflectivity obtained in the optimized structures is 59, 73, 85 and 90% for total thicknesses of 5, 10, 20 and  $30\mu\text{m}$  respectively, which translates to an enhancement of  $\sim 22\%$ ,  $20\%$ ,  $20\%$  and  $10\%$  over that obtained in randomly generated RML structures of the same total thicknesses. In order to arrive at the high reflectivity RML structures, the GA optimizer searches through structures with various average layer thicknesses. This is shown in Fig. 6.5(b) for the case of an optimization run on a system with total thickness of  $10\mu\text{m}$ , where the GA initially scans through a range of average layer thicknesses and finally converges to a value of  $303\text{nm}$ , which is found to provide the structure with the highest reflectivity. The average layer thicknesses of the GA optimized structures for all total thicknesses studied are found to lie in the range of  $290 - 350\text{nm}$ .

The designs of the GA-optimized RML structures for different total thicknesses are shown in Fig. 6.5(c). An interesting feature observed in all the optimized structures is the presence of a  $\text{CeO}_2$  layer at the beginning and end of the structure, which leads to an odd number of layers within the RML. This is in contrast to the traditional method of superlattice design, where the layers are usually paired and the structure contains an even number of layers. Since  $\text{CeO}_2$  provides a higher contrast in refractive index to air than  $\text{MgO}$ , the presence of a  $\text{CeO}_2$  layer at either end of the structure results in an interface with a higher reflection coefficient leading to enhancement of the total reflectivity.

To gain insight into the superior performance of the GA-optimized RML structures, we compare the spectral reflectivity of three different structures as shown in Fig. 6.6(a)-(c): the best  $10\mu\text{m}$  total thickness RML structure identified by the GA, the reference periodic SL structure with same average layer thickness, and an unoptimized RML which was randomly generated from the reference SL structure using a degree of randomness  $\delta = 40\%$ . As can be observed in the figure, the inclusion of randomness in layer thicknesses causes an increase in the reflectivity peaks in a wide range of wavelengths from the reference periodic SL. However, the wavelengths of the high reflectivity peaks in the GA-optimized structure coincide with the location of the peak blackbody radiation spectrum at  $T = 1500\text{K}$  (shown by the shaded plot in Fig 6.6(a)-(c)). As a result, the integrated total reflectivity of the

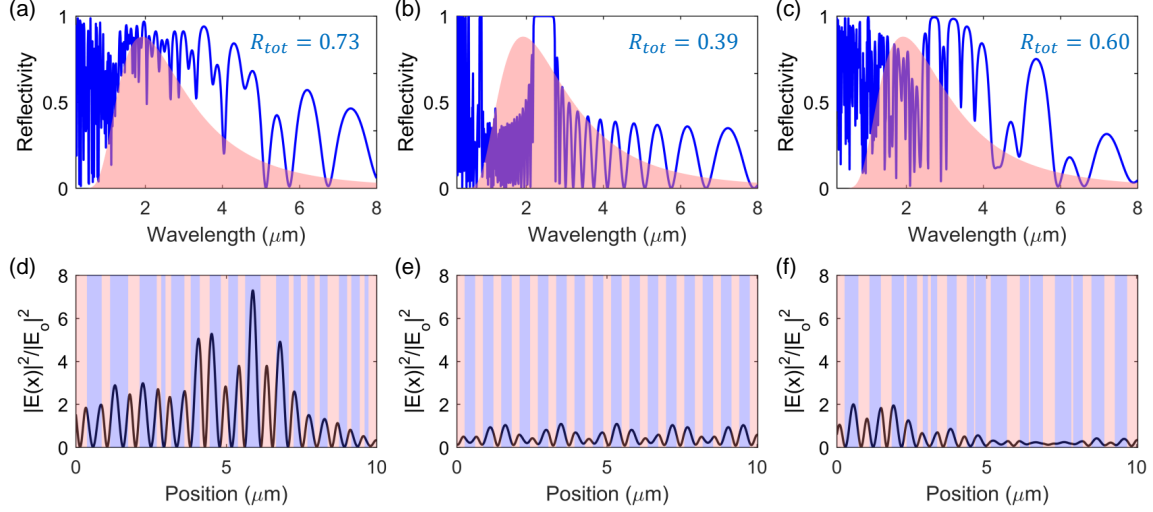


**Figure 6.6.** Spectral reflectivity vs. wavelength for three multilayer structures with total thickness of  $10\mu\text{m}$ : (a) GA-optimized RML with high reflectivity, (b) periodic SL with same average layer thickness, and (c) an unoptimized RML structure with same average layer thickness. The field intensity distribution vs. position along the multilayer structure is shown for the same structures for a wavelength of  $1.84\mu\text{m}$ : (d) GA-optimized RML with high reflectivity, showing significant field enhancement, (e) periodic SL with same average layer thickness, and (f) an unoptimized RML structure with same average layer thickness. The  $x$ -direction denotes the stacking direction of the multilayer structures.

GA-optimized structure is higher than that of the periodic SL which shows an overall lower spectral reflectivity, as well as the unoptimized RML for which the high reflectivity peaks do not coincide with the location of peak blackbody radiation.

We also calculate the distribution of field intensity inside the above multilayer structures to elucidate the effect of photon localization on the enhanced reflectivity in the GA-optimized RML structure. The magnitude of the local field at any position  $x$  along the direction of the multilayer structure can be obtained from the sum of the forward and backward components as:

$$|E(x)| = |E^+(x) + E^-(x)| \quad (6.10)$$

The normalized field intensity at any position can then be calculated as  $|E(x)|^2/|E_0|^2$ , which is shown in Fig. 6.6(d)-(f) for a representative wavelength of  $1.84\mu\text{m}$ . Our results show a significant field enhancement within certain spatial regions within the GA-optimized RML structure, which is lower in the unoptimized RML structure and largely absent in the periodic SL structure. This clearly demonstrates the presence of photon localization within the optimized RML structures leading to high reflectivity.

## 6.4 Conclusions

In this work, we employed a materials informatics (MI)-based optimization method to identify  $\text{CeO}_2$ - $\text{MgO}$  random multilayer (RML) structures with high reflectivity for applications as high temperature thermal barrier coatings (TBCs). The transfer matrix method was used to evaluate the spectral reflectivity of candidate multilayer structures, and the total reflectivity was determined by integrating over the blackbody radiation spectrum at  $T = 1500\text{K}$ , which is representative of the high temperatures of application for such TBC systems. We first systematically investigated the influence of superlattice(SL) and RML design parameters on the reflectivity, such as the total thickness, average layer thickness and degree of randomness in individual layer thicknesses. For the periodic SLs of different total thicknesses from  $1 - 50\mu\text{m}$ , the presence of an optimum average layer thickness was noticed at which the total reflectivity at  $T = 1500\text{K}$  is maximized, due to the overlap of a high reflectivity “stop band” within the spectral reflectivity curve with the peak of the blackbody radiation spectrum. The influence of randomness in layer thicknesses was found to increase the overall spectral reflectivity due to the effect of photon localization. Next, a Genetic Algorithm (GA) optimization process was used to identify high reflectivity RML structures with total thicknesses of  $5, 10, 20$  and  $30\mu\text{m}$ , and the optimized structures were found to have reflectivities of  $59, 73, 85$  and  $90\%$  respectively, which translates to an enhancement of  $22, 20, 20$  and  $10\%$  over the maximum reflectivity in periodic SLs with same total thickness. Surprisingly, all our GA-optimized structures show the presence of an odd number of layers with an unpaired  $\text{CeO}_2$  layer at the extreme end of the RML, which deviates from the traditional way of designing binary superlattices with paired layers. This

occurs because the unpaired  $\text{CeO}_2$  layer in the optimized RMLs provide a greater contrast in refractive index with air, leading to a higher interface reflectivity. Finally, we calculate the spectral reflectivity and the field intensity distribution within the optimal and sub-optimal RML structures to understand the impact of photon localization. Our work demonstrates an efficient and general purpose method for performing MI-accelerated design optimization for target radiative properties of nanostructures, as well as provides the design of high reflectivity multilayered TBCs with insight into the physical mechanisms leading to enhanced performance.

## 7. SUMMARY AND FUTURE DIRECTIONS

### 7.1 Summary

In this dissertation, we have used a combinations of computationally expensive but high-fidelity atomistic simulation methods and accelerated machine learning based prediction/search algorithms to advance the understanding of phonon thermal transport in nanostructured solids.

#### 7.1.1 Atomistic simulations of thermal transport in $\text{Sb}_2\text{Te}_3$ and $\text{Bi}_2\text{Te}_3$ nanostructures

In chapter 2, we develop classical interatomic potential parameters to describe thermal transport in the important thermoelectric material  $\text{Sb}_2\text{Te}_3$ . The lack of suitable interatomic potentials for many complex materials greatly prohibits effective use of MD simulations to investigate properties of bulk materials and nanostructures. We use the method of fitting to an *ab initio* energy surface to develop our potential parameters for the complex binary material. Density-functional theory is used to calculate the ground state electronic structure of the  $\text{Sb}_2\text{Te}_3$  crystal, following which the total energies of a series of artificially distorted lattice configurations are calculated to create the energy surface. A Morse potential functional form is fitted to the energy surface and experimental data, and the parameters are used to calculate the bulk crystal properties and phonon spectra using lattice dynamics. Our parameters are able to reproduce the lattice structure, elastic constants and acoustic phonon dispersion in good agreement with experimental data. Molecular dynamics simulations are performed using the fitted potential to calculate the thermal conductivity of bulk  $\text{Sb}_2\text{Te}_3$  using the Green-Kubo method. The predicted thermal conductivity shows a  $1/T$  variation in both in-plane and cross-plane directions with the results in the range of experimental measurements. Frequency domain normal mode analysis (FD-NMA) is used to calculate the modal phonon relaxation times and the accumulation of thermal conductivity with respect to phonon mean free path. Our results show that phonons with mean free paths between 3 and 100 nm contribute to 80% of the total cross-plane thermal conductivity.

In chapter 3, we utilize the developed potentials to investigate the phonon transport across  $\text{Bi}_2\text{Te}_3\text{-Sb}_2\text{Te}_3$  interface and superlattice nanostructures. Bismuth telluride ( $\text{Bi}_2\text{Te}_3$ ) and its alloys with antimony telluride ( $\text{Sb}_2\text{Te}_3$ ) have long been considered to be the best room temperature bulk thermoelectric (TE) materials. Particularly, ultra-low thermal conductivities have been observed in  $\text{Bi}_2\text{Te}_3\text{-Sb}_2\text{Te}_3$  1-D superlattices (SLs), leading to thermoelectric figures of merit ( $ZT$ ) as high as 2.4. In contrast, very few numerical studies have been performed to provide insight into the phonon transport across these nanostructures. In this work, we perform phonon transport calculations across a  $\text{Bi}_2\text{Te}_3\text{-Sb}_2\text{Te}_3$  interface using non-equilibrium molecular dynamics simulations. The results are compared with a modified Landauer transport approach using phonon transmission coefficients from the diffuse mismatch model. Our results show that inelastic scattering processes contribute to increased interfacial thermal conductance by as much as 40% from 200 – 400 K. We also calculate the thermal conductivities of  $\text{Bi}_2\text{Te}_3\text{-Sb}_2\text{Te}_3$  superlattices with varying periods. A minimum thermal conductivity of 0.27 W/mK is observed at a period of 4 nm, which is attributed to the competition between incoherent and coherent phonon transport regimes. Our results, when compared against previous experimental measurements, show good agreement with respect to the range of thermal conductivity values and the trend and location of the minimum superlattice thermal conductivity.

### **7.1.2 Machine learning accelerated discovery of non-intuitive phonon transport in nanostructures**

Anderson localization of phonons due to aperiodicity can reduce thermal conductivity in superlattices, but the lower limit of thermal conductivity remains elusive due to the prohibitively large design space. In Chapter 4, we demonstrate that an intuition-based manual search for aperiodic superlattice structures (random multilayers or RMLs) with the lowest thermal conductivity yields only a local minimum, while a genetic algorithm (GA) based approach can efficiently identify the globally minimum thermal conductivity by only exploring a small fraction of the design space. Our results show that this minimum value occurs at an average RML period that is, surprisingly, smaller than the period corresponding to the minimum SL thermal conductivity. Above this critical period, scattering of incoherent

phonons at interfaces is less, whereas below this period, the room for randomization becomes less, thus putting more coherent phonons out of Anderson localization and causing increased thermal conductivity. Moreover, the lower limit of the thermal conductivity occurs at a moderate rather than maximum randomness of the layer thickness. Our machine learning approach demonstrates a general process of exploring an otherwise prohibitively large design space to gain non-intuitive physical insights.

In Chapter 5, we explore the possibility of discovering exceptions to the well understood theory of randomness in superlattice layer thicknesses leading to reduced thermal conductivity. In particular, we aim to identify RML structures showing enhancement in thermal conductivity from the corresponding SL of same period, thus showing counter-intuitive trends in thermal transport. Since no intuition is available to narrow the search to a smaller subset of the large design space, a random search is first attempted but is unable to identify any exceptional structures. We then employ a machine learning accelerated search using a convolutional neural network (CNN) to replace the computationally expensive MD simulations for thermal conductivity prediction of the RML candidates. The training dataset for the CNN is generated dynamically in a systematic manner, to ensure that CNN can learn the relevant spatial features leading to locally enhanced thermal transport in the RMLs. Using the rapid prediction tool, we are able to search the entire design space in an exhaustive manner, and successfully identify RML structures with thermal conductivity higher than the corresponding SL. The enhancement in thermal conductivity is attributed to the presence of closely spaced interfaces in the RML leading to increase in local coherence, whereas the same is absent in the SLs at the relatively large average period. Apart from being able to discover exceptions to previously well understood transport mechanism, our results show the importance of a machine learning based search process in guiding nanostructure design for target applications.

### **7.1.3 Machine learning accelerated discovery of multilayered photonic structures for thermal barrier coatings**

In Chapter 6, we demonstrate the application of materials informatics based optimization for identifying multilayer photonic structures with enhanced reflectivity for application as

high temperature thermal barrier coating (TBC) systems. Although most TBC materials are chosen for their low lattice thermal conductivity, such systems also need to incorporate mechanisms to prevent thermal transport by radiation which becomes dominant at higher temperatures. We investigate the performance of  $\text{CeO}_2\text{-MgO}$  based periodic SLs and RMLs, where the spectral reflectivity and transmissivity is obtained using the transfer matrix method, and the total reflectivity is evaluated by integrating over the blackbody radiation spectrum at  $T = 1500\text{K}$ . We first manually vary design parameters such as total thickness and average layer thickness, which provides an upper limit on the reflectivity in periodic SL systems. The inclusion of randomness in individual layer thicknesses is shown to significantly enhance the reflectivity from the reference SLs, however, a large variation is seen for different realizations of RMLs with the same degree of randomness. In order to search the large design space of RML structures efficiently, we employ a GA optimization process which is able to identify RML structures with upto 22% enhancement in total reflectivity from the reference SL structures of same total thickness. By calculating the spectral reflectivity of and the field intensity distribution within the optimal and sub-optimal structures, we are able to demonstrate the effect of photon localization leading to enhancement of reflectivity in the GA-identified high reflectivity RML structures. Our results show an accelerated approach for designing multilayer TBC systems that can incorporate broadband photon and phonon scattering mechanisms, and can be extended to include other design modifications such as rough interfaces, defects and multiple-material multilayers.

## 7.2 Future directions

In this final section of the dissertation, we present a few research directions that may be explored in continuation of the objectives of this thesis work. Similar to the vein of the dissertation, future endeavors may proceed along the two avenues of high fidelity atomistic simulations of thermal transport in novel materials nanostructures, and machine learning techniques utilizing the high fidelity data for accelerated design optimization.



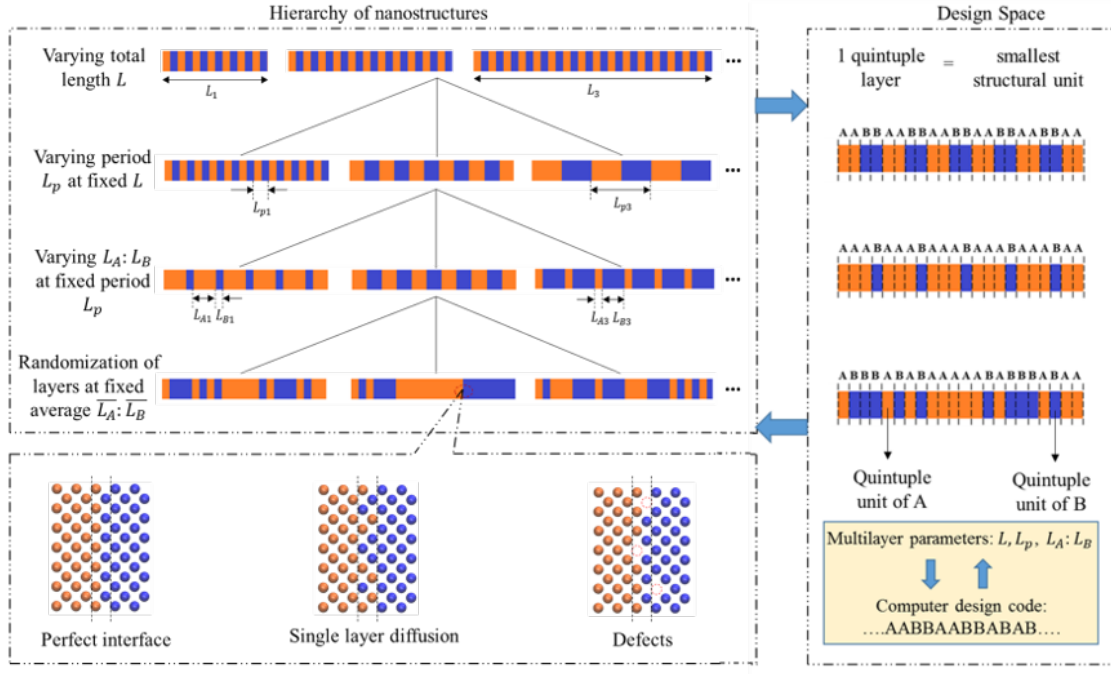


**Figure 7.1.** Generation of hierarchically disordered superlattice systems with perturbations in layer thicknesses, interface mixing and defects (left) and the interface with machine learning algorithms for prediction and optimization (right)

### 7.2.1 Thermal transport in hierarchically disordered systems

The study of thermal transport in periodic and aperiodic superlattices performed so far as part of this dissertation have shown the effectiveness of introducing disorder to reduce thermal conductivity of periodic systems. The randomly spaced interfaces in an aperiodic superlattice can scatter the long wavelength coherent phonons, but fail to affect mid-to-low wavelength phonons which can still have significant thermal transport. On the other hand, the presence of defects and rough interfaces have been shown to be effective in scattering phonons of shorter wavelengths. Although these mechanisms have been investigated separately for specific systems, the combination of these can have the effect of broadband phonon scattering over a range of phonon wavelengths and mean free paths, thus providing a powerful strategy to reduce the thermal transport in nanostructured thermoelectric materials.

In addition, the class of van der Waal's heterostructures of two-dimensional (2D) materials such as graphene, MoS<sub>2</sub>, WSe<sub>2</sub> and other materials have gained widespread attention

in the recent decades. Due to the relative ease with which such materials can be stacked as layers with little effect of lattice mismatch, systems built of combinations of these materials are attractive candidates for applications where independent tuning of electronic and thermal transport properties are required, such as in semiconductors. Several studies have been performed to investigate thermal transport in multilayer heterostructures, however, the effect of introducing disorder in these systems such as defects, angular mismatch between layers etc. have not been elucidated in detail.

In this scenario, our work may be extended to the use of atomistic simulation methods such as MD simulations to uncover the effect of various levels of disorder on the systems described above. Figure 7.1 shows a workflow involving systematically generated superlattice nanostructures with various levels of disorder including randomly spaced interfaces, imperfect interfaces and defects within bulk materials. Similar approaches may be considered for systems formed from combinations of 2D materials. Due to the extremely large design space formed, the atomistic simulations need to be interfaces with a machine learning method for rapid screening of such systems. As with our previous studies, the optimal structures will progress the current understanding of broadband phonon scattering in such systems.

### **7.2.2 Machine learning accelerated prediction of four phonon scattering rates in solids**

One of the more challenging aspects of predicting thermal transport in solids using *ab initio* methods is the calculation of the phonon scattering rates. Although all orders of phonon-phonon scattering processes are important in anharmonic materials, traditionally the phonon scattering is considered only upto three phonon scattering terms, since reasonable agreement is found with experimental measurements of many materials. However, as the focus has shifted to materials with more extreme thermal properties, a significant discrepancy has been observed in some cases between theoretical predictions and experimental measurements, indicating the need to refine existing methods.

Recently, the inclusion of four phonon scattering as a dominant scattering mechanism in some materials has been able to bridge this gap. The calculation of four phonon scattering rates is by no means a trivial task, and the sheer complexity and computational expense

involved has been a major factor in the negligence of four phonon contribution in theoretical predictions for a long time. Feng *et al.*[139], [140] were able to mitigate the high computational cost and propose an efficient method for calculating the four phonon scattering rates in solids. Their work has, since, been supported by experimental observation of high four phonon scattering rates in materials such as boron arsenide.

Calculation of the four phonon scattering rates is still an extremely challenging and computationally intensive task for any material, given the large phonon phase space and the vast number of possible four phonon scattering events for which the calculation needs to be performed. Moreover, the relative importance of different four phonon processes in comparison to others can provide a shortcut to performing all of these calculations. Finally, the relation of bulk properties to the four phonon scattering mechanisms can provide us with guidance to identifying more materials where four phonon scattering is important. Here, the full capability of machine learning may be used to identify the inherent relations in the phonon phase space to further reduce the computational workload in these calculations. One can also understand the importance of different material properties on the scattering rates, using suitable data processing techniques.

## REFERENCES

- [1] H. Ritchie and M. Roser, “Energy,” *Our World in Data*, 2020, <https://ourworldindata.org/energy>.
- [2] B. Zalba, J. M. Marin, L. F. Cabeza, and H. Mehling, “Review on thermal energy storage with phase change: Materials, heat transfer analysis and applications,” *Applied thermal engineering*, vol. 23, no. 3, pp. 251–283, 2003.
- [3] N. P. Padture, M. Gell, and E. H. Jordan, “Thermal barrier coatings for gas-turbine engine applications,” *Science*, vol. 296, no. 5566, pp. 280–284, 2002.
- [4] G. J. Snyder and E. S. Toberer, “Complex thermoelectric materials,” in *materials for sustainable energy: a collection of peer-reviewed research and review articles from Nature Publishing Group*, World Scientific, 2011, pp. 101–110.
- [5] M. S. Dresselhaus, G. Chen, M. Y. Tang, R. Yang, H. Lee, D. Wang, Z. Ren, J.-P. Fleurial, and P. Gogna, “New directions for low-dimensional thermoelectric materials,” *Advanced materials*, vol. 19, no. 8, pp. 1043–1053, 2007.
- [6] D. Medlin and G. Snyder, “Interfaces in bulk thermoelectric materials: A review for current opinion in colloid and interface science,” *Current Opinion in Colloid & Interface Science*, vol. 14, no. 4, pp. 226–235, 2009.
- [7] Z. Ling, Z. Zhang, G. Shi, X. Fang, L. Wang, X. Gao, Y. Fang, T. Xu, S. Wang, and X. Liu, “Review on thermal management systems using phase change materials for electronic components, li-ion batteries and photovoltaic modules,” *Renewable and Sustainable Energy Reviews*, vol. 31, pp. 427–438, 2014.
- [8] B. Li, L. Wang, and G. Casati, “Thermal diode: Rectification of heat flux,” *Physical review letters*, vol. 93, no. 18, p. 184301, 2004.
- [9] L. Wang and B. Li, “Thermal logic gates: Computation with phonons,” *Physical review letters*, vol. 99, no. 17, p. 177208, 2007.
- [10] C. Alaoui, “Solid-state thermal management for lithium-ion ev batteries,” *IEEE Transactions on Vehicular Technology*, vol. 62, no. 1, pp. 98–107, 2012.
- [11] F. Sarvar, D. C. Whalley, and P. P. Conway, “Thermal interface materials-a review of the state of the art,” in *2006 1st Electronic Systemintegration Technology Conference*, IEEE, vol. 2, 2006, pp. 1292–1302.

- [12] F. Kuznik, D. David, K. Johannes, and J.-J. Roux, "A review on phase change materials integrated in building walls," *Renewable and Sustainable Energy Reviews*, vol. 15, no. 1, pp. 379–391, 2011.
- [13] L. L. N. Laboratory, "Energy flow charts," Lawrence Livermore National Laboratory, Tech. Rep., 2018.
- [14] R. Venkatasubramanian, E. Siivola, T. Colpitts, and B. O'Quinn, "Thin-film thermoelectric devices with high room-temperature figures of merit," *Nature*, vol. 413, 597 EP -, Oct. 2001, Article. [Online]. Available: <http://dx.doi.org/10.1038/35098012>.
- [15] R. Siegel and C. M. Spuckler, "Analysis of thermal radiation effects on temperatures in turbine engine thermal barrier coatings," *Materials Science and Engineering: A*, vol. 245, no. 2, pp. 150–159, 1998.
- [16] R. Venkatasubramanian, "Lattice thermal conductivity reduction and phonon localizationlike behavior in superlattice structures," *Phys. Rev. B*, vol. 61, pp. 3091–3097, 4 Jan. 2000. DOI: [10.1103/PhysRevB.61.3091](https://doi.org/10.1103/PhysRevB.61.3091). [Online]. Available: <https://link.aps.org/doi/10.1103/PhysRevB.61.3091>.
- [17] M. N. Luckyanova, J. Garg, K. Esfarjani, A. Jandl, M. T. Bulsara, A. J. Schmidt, A. J. Minnich, S. Chen, M. S. Dresselhaus, Z. Ren, *et al.*, "Coherent phonon heat conduction in superlattices," *Science*, vol. 338, no. 6109, pp. 936–939, 2012.
- [18] M. Steele and F. Rosi, "Thermal conductivity and thermoelectric power of germanium-silicon alloys," *Journal of Applied Physics*, vol. 29, no. 11, pp. 1517–1520, 1958.
- [19] C. B. Vining, W. Laskow, J. O. Hanson, R. R. Van der Beck, and P. D. Gorsuch, "Thermoelectric properties of pressure-sintered  $\text{Si}_{0.8}\text{Ge}_{0.2}$  thermoelectric alloys," *Journal of applied physics*, vol. 69, no. 8, pp. 4333–4340, 1991.
- [20] L. Testardi, J. Bierly, and F. Donahoe, "Transport properties of p-type  $\text{Bi}_2\text{Te}_3$   $\text{Sb}_2\text{Te}_3$  alloys in the temperature range 80–370°K," *Journal of Physics and Chemistry of Solids*, vol. 23, no. 9, pp. 1209–1217, 1962, ISSN: 0022-3697. DOI: [https://doi.org/10.1016/0022-3697\(62\)90168-3](https://doi.org/10.1016/0022-3697(62)90168-3). [Online]. Available: <http://www.sciencedirect.com/science/article/pii/0022369762901683>.
- [21] W. Yim and F. Rosi, "Compound tellurides and their alloys for peltier cooling—a review," *Solid-State Electronics*, vol. 15, no. 10, pp. 1121–1140, 1972.

- [22] P. F. P. Poudeu, J. D'Angelo, H. Kong, A. Downey, J. L. Short, R. Pcionek, T. P. Hogan, C. Uher, and M. G. Kanatzidis, "Nanostructures versus solid solutions: low lattice thermal conductivity and enhanced thermoelectric figure of merit in pb9.6sb0.2te10-xsex bulk materials," *Journal of the American Chemical Society*, vol. 128, no. 44, pp. 14 347–14 355, 2006, PMID: 17076508. DOI: [10.1021/ja0647811](https://doi.org/10.1021/ja0647811). eprint: <https://doi.org/10.1021/ja0647811>. [Online]. Available: <https://doi.org/10.1021/ja0647811>.
- [23] Q. Zhang, F. Cao, W. Liu, K. Lukas, B. Yu, S. Chen, C. Opeil, D. Broido, G. Chen, and Z. Ren, "Heavy doping and band engineering by potassium to improve the thermoelectric figure of merit in p-type pbte, pbse, and pbte1-ysey," *Journal of the American Chemical Society*, vol. 134, no. 24, pp. 10 031–10 038, 2012, PMID: 22676702. DOI: [10.1021/ja301245b](https://doi.org/10.1021/ja301245b). eprint: <https://doi.org/10.1021/ja301245b>. [Online]. Available: <https://doi.org/10.1021/ja301245b>.
- [24] S. Bhattacharya, A. L. Pope, R. T. Littleton, T. M. Tritt, V. Ponnambalam, Y. Xia, and S. J. Poon, "Effect of sb doping on the thermoelectric properties of ti-based half-heusler compounds, tinisn1-xsbx," 2000.
- [25] B. Poudel, Q. Hao, Y. Ma, Y. Lan, A. Minnich, B. Yu, X. Yan, D. Wang, A. Muto, D. Vashaee, *et al.*, "High-thermoelectric performance of nanostructured bismuth antimony telluride bulk alloys," *Science*, vol. 320, no. 5876, pp. 634–638, 2008.
- [26] Y. Y. Ma, Q. Hao, B. Poudel, Y. Lan, B. Yu, D. Wang, G. Chen, and Z. Ren, "Enhanced thermoelectric figure-of-merit in p-type nanostructured bismuth antimony tellurium alloys made from elemental chunks.," *Nano letters*, vol. 8 8, pp. 2580–4, 2008.
- [27] W. Xie, X. Tang, Y. Yan, Q. Zhang, and T. M. Tritt, "Unique nanostructures and enhanced thermoelectric performance of melt-spun bisbte alloys," 2009.
- [28] G. Chen, "Size and interface effects on thermal conductivity of superlattices and periodic thin-film structures," 1997.
- [29] L. M. G. Gonçalves, C. Couto, P. Alpuim, A. G. Rolo, F. Völklein, and J. H. Correia, "Optimization of thermoelectric properties on bi2te3 thin films deposited by thermal co-evaporation," 2010.
- [30] M. Takashiri, M. Takiishi, S. Tanaka, K. Miyazaki, and H. Tsukamoto, "Thermoelectric properties of n-type nanocrystalline bismuth-telluride-based thin films deposited by flash evaporation," 2007.
- [31] J. Wang, X. Mu, X. Wang, N. Wang, F. Ma, W. Liang, and M. Sun, "The thermal and thermoelectric properties of in-plane c-bn hybrid structures and graphene/h-bn van der waals heterostructures," 2018.

- [32] K. S. Novoselov, A. Mishchenko, A. Carvalho, and A. H. Castro Neto, “2d materials and van der waals heterostructures,” *Science*, vol. 353, no. 6298, 2016, ISSN: 0036-8075. DOI: [10.1126/science.aac9439](https://doi.org/10.1126/science.aac9439). eprint: <https://science.sciencemag.org/content/353/6298/aac9439.full.pdf>. [Online]. Available: <https://science.sciencemag.org/content/353/6298/aac9439>.
- [33] S. Sahoo, A. P. S. Gaur, M. Ahmadi, M. J.-F. Guinel, and R. S. Katiyar, “Temperature-dependent raman studies and thermal conductivity of few-layer mos<sub>2</sub>,” 2013.
- [34] A. A. Balandin, S. Ghosh, W. Bao, I. Calizo, D. B. Teweldebrhan, F. Miao, and C. N. Lau, “Superior thermal conductivity of single-layer graphene,” *Nano letters*, vol. 8 3, pp. 902–7, 2008.
- [35] S. Ghosh, I. Calizo, D. B. Teweldebrhan, E. P. Pokatilov, D. L. Nika, A. A. Balandin, W. Bao, F. Miao, and C. N. Lau, “Extremely high thermal conductivity of graphene: Prospects for thermal management applications in nanoelectronic circuits,” 2008.
- [36] S. Chen, Q. Wu, C. Mishra, J. Kang, H. Zhang, K. Cho, W. Cai, A. A. Balandin, and R. S. Ruoff, “Thermal conductivity of isotopically modified graphene,” *Nature materials*, vol. 11 3, pp. 203–7, 2012.
- [37] M. Fujii, X. Zhang, H. Xie, H. Ago, K. Takahashi, T. Ikuta, H. Abe, and T. Shimizu, “Measuring the thermal conductivity of a single carbon nanotube,” *Physical review letters*, vol. 95 6, p. 065 502, 2005.
- [38] Y. Wang, A. K. Vallabhaneni, J. Hu, B. Qiu, Y. P. Chen, and X. Ruan, “Phonon lateral confinement enables thermal rectification in asymmetric single-material nanostructures,” *Nano letters*, vol. 14 2, pp. 592–6, 2014.
- [39] L. R. Lindsay, W. Li, J. Carrete, N. Mingo, D. Broido, and T. L. Reinecke, “Phonon thermal transport in strained and unstrained graphene from first principles,” 2014.
- [40] B. Kong, S. Paul, M. B. Nardelli, and K. W. Kim, “First-principles analysis of lattice thermal conductivity in monolayer and bilayer graphene,” 2009.
- [41] J. Hu, X. Ruan, and Y. P. Chen, “Thermal conductivity and thermal rectification in graphene nanoribbons: A molecular dynamics study,” *Nano letters*, vol. 9 7, pp. 2730–5, 2009.
- [42] T. Feng and X. Ruan, “Four-phonon scattering reduces intrinsic thermal conductivity of graphene and the contributions from flexural phonons,” 2018.
- [43] K. Gordiz and A. Henry, “Phonon transport at interfaces: Determining the correct modes of vibration,” 2016.

- [44] D. G. Cahill, A. J. Bullen, and S. M. Lee, “Interface thermal conductance and the thermal conductivity of multilayer thin films,” 2000.
- [45] T. Feng, Y. Zhong, J. Shi, and X. Ruan, “Unexpected high inelastic phonon transport across solid-solid interface: Modal nonequilibrium molecular dynamics simulations and landauer analysis,” *Physical Review B*, vol. 99, no. 4, p. 045 301, 2019.
- [46] M. V. Simkin and G. D. Mahan, “Minimum thermal conductivity of superlattices,” *Phys. Rev. Lett.*, vol. 84, pp. 927–930, 5 Jan. 2000. DOI: [10.1103/PhysRevLett.84.927](https://doi.org/10.1103/PhysRevLett.84.927). [Online]. Available: <https://link.aps.org/doi/10.1103/PhysRevLett.84.927>.
- [47] B. C. Daly, H. J. Maris, K. Imamura, and S. Tamura, “Molecular dynamics calculation of the thermal conductivity of superlattices,” *Phys. Rev. B*, vol. 66, p. 024 301, 2 Jun. 2002. DOI: [10.1103/PhysRevB.66.024301](https://doi.org/10.1103/PhysRevB.66.024301). [Online]. Available: <https://link.aps.org/doi/10.1103/PhysRevB.66.024301>.
- [48] Y. Chen, D. Li, J. R. Lukes, Z. Ni, and M. Chen, “Minimum superlattice thermal conductivity from molecular dynamics,” *Physical Review B*, vol. 72, no. 17, p. 174 302, 2005.
- [49] H. Mizuno, S. Mossa, and J.-L. Barrat, “Beating the amorphous limit in thermal conductivity by superlattices design,” *Scientific reports*, vol. 5, p. 14 116, 2015.
- [50] K. Termentzidis, P. Chantrenne, J.-Y. Duquesne, and A. Saci, “Thermal conductivity of gaas/alas superlattices and the puzzle of interfaces,” *Journal of Physics: Condensed Matter*, vol. 22, no. 47, p. 475 001, 2010.
- [51] T. Borca-Tasciuc, W. Liu, J. Liu, T. Zeng, D. W. Song, C. D. Moore, G. Chen, K. L. Wang, M. S. Goorsky, T. Radetic, *et al.*, “Thermal conductivity of symmetrically strained si/ge superlattices,” *Superlattices and microstructures*, vol. 28, no. 3, pp. 199–206, 2000.
- [52] B. Saha, Y. R. Koh, J. Comparan, S. Sadasivam, J. L. Schroeder, M. Garbrecht, A. Mohammed, J. Birch, T. Fisher, A. Shakouri, *et al.*, “Cross-plane thermal conductivity of (ti, w) n/(al, sc) n metal/semiconductor superlattices,” *Physical Review B*, vol. 93, no. 4, p. 045 311, 2016.
- [53] S. Chakraborty, C. Kleint, A. Heinrich, C. Schneider, J. Schumann, M. Falke, and S. Teichert, “Thermal conductivity in strain symmetrized si/ge superlattices on si (111),” *Applied Physics Letters*, vol. 83, no. 20, pp. 4184–4186, 2003.
- [54] J. Caylor, K. Coonley, J. Stuart, T. Colpitts, and R. Venkatasubramanian, “Enhanced thermoelectric performance in pbte-based superlattice structures from reduction of lattice thermal conductivity,” *Applied physics letters*, vol. 87, no. 2, p. 023 105, 2005.



- [55] Y. Wang, C. Gu, and X. Ruan, “Optimization of the random multilayer structure to break the random-alloy limit of thermal conductivity,” *Applied Physics Letters*, vol. 106, no. 7, p. 073 104, 2015.
- [56] B. Qiu, G. Chen, and Z. Tian, “Effects of aperiodicity and roughness on coherent heat conduction in superlattices,” *Nanoscale and Microscale Thermophysical Engineering*, vol. 19, no. 4, pp. 272–278, 2015. DOI: [10.1080/15567265.2015.1102186](https://doi.org/10.1080/15567265.2015.1102186). eprint: <https://doi.org/10.1080/15567265.2015.1102186>. [Online]. Available: <https://doi.org/10.1080/15567265.2015.1102186>.
- [57] P. Chakraborty, L. Cao, and Y. Wang, “Ultralow lattice thermal conductivity of the random multilayer structure with lattice imperfections,” *Scientific reports*, vol. 7, no. 1, p. 8134, 2017.
- [58] A. Frachioni and B. White Jr, “Simulated thermal conductivity of silicon-based random multilayer thin films,” *Journal of Applied Physics*, vol. 112, no. 1, p. 014 320, 2012.
- [59] Y. Wang, H. Huang, and X. Ruan, “Decomposition of coherent and incoherent phonon conduction in superlattices and random multilayers,” *Phys. Rev. B*, vol. 90, p. 165 406, 16 Oct. 2014. DOI: [10.1103/PhysRevB.90.165406](https://doi.org/10.1103/PhysRevB.90.165406). [Online]. Available: <https://link.aps.org/doi/10.1103/PhysRevB.90.165406>.
- [60] X. Mu, L. Wang, X. Yang, P. Zhang, A. C. To, and T. Luo, “Ultra-low thermal conductivity in si/ge hierarchical superlattice nanowire,” *Scientific reports*, vol. 5, p. 16 697, 2015.
- [61] T. Juntunen, O. Vänskä, and I. Tittonen, “Anderson localization quenches thermal transport in aperiodic superlattices,” *Physical review letters*, vol. 122, no. 10, p. 105 901, 2019.
- [62] P. R. Chowdhury, C. Reynolds, A. Garrett, T. Feng, S. P. Adiga, and X. Ruan, “Machine learning maximized anderson localization of phonons in aperiodic superlattices,” *Nano Energy*, vol. 69, p. 104 428, 2020.
- [63] O. Hellman, P. Steneteg, I. A. Abrikosov, and S. I. Simak, “Temperature dependent effective potential method for accurate free energy calculations of solids,” *Physical Review B*, vol. 87, no. 10, p. 104 111, 2013.
- [64] J. Turney, A. McGaughey, and C. Amon, “Assessing the applicability of quantum corrections to classical thermal conductivity predictions,” *Physical Review B*, vol. 79, no. 22, p. 224 305, 2009.

- [65] C. Z. Wang, C. T. Chan, and K. M. Ho, “Molecular-dynamics study of anharmonic effects in silicon,” *Phys. Rev. B*, vol. 40, pp. 3390–3393, 5 Aug. 1989. DOI: [10.1103/PhysRevB.40.3390](https://doi.org/10.1103/PhysRevB.40.3390). [Online]. Available: <https://link.aps.org/doi/10.1103/PhysRevB.40.3390>.
- [66] J. Shiomi and S. Maruyama, “Non-fourier heat conduction in a single-walled carbon nanotube: Classical molecular dynamics simulations,” *Phys. Rev. B*, vol. 73, p. 205 420, 20 May 2006. DOI: [10.1103/PhysRevB.73.205420](https://doi.org/10.1103/PhysRevB.73.205420). [Online]. Available: <https://link.aps.org/doi/10.1103/PhysRevB.73.205420>.
- [67] N. de Koker, “Thermal conductivity of mgo periclase from equilibrium first principles molecular dynamics,” *Phys. Rev. Lett.*, vol. 103, p. 125 902, 12 Sep. 2009. DOI: [10.1103/PhysRevLett.103.125902](https://doi.org/10.1103/PhysRevLett.103.125902). [Online]. Available: <https://link.aps.org/doi/10.1103/PhysRevLett.103.125902>.
- [68] J. A. Thomas, J. E. Turney, R. M. Iutzi, C. H. Amon, and A. J. H. McGaughey, “Predicting phonon dispersion relations and lifetimes from the spectral energy density,” *Phys. Rev. B*, vol. 81, p. 081 411, 8 Feb. 2010. DOI: [10.1103/PhysRevB.81.081411](https://doi.org/10.1103/PhysRevB.81.081411). [Online]. Available: <https://link.aps.org/doi/10.1103/PhysRevB.81.081411>.
- [69] T. Feng, B. Qiu, and X. Ruan, “Anharmonicity and necessity of phonon eigenvectors in the phonon normal mode analysis,” *Journal of Applied Physics*, vol. 117, no. 19, p. 195 102, 2015.
- [70] L. Lindsay, C. Hua, X. Ruan, and S. Lee, “Survey of ab initio phonon thermal transport,” *Materials Today Physics*, vol. 7, pp. 106–120, 2018.
- [71] R. Ramprasad, R. Batra, G. Pilania, A. Mannodi-Kanakkithodi, and C. Kim, “Machine learning in materials informatics: Recent applications and prospects,” *npj Computational Materials*, vol. 3, no. 1, pp. 1–13, 2017.
- [72] K. T. Butler, D. W. Davies, H. Cartwright, O. Isayev, and A. Walsh, “Machine learning for molecular and materials science,” *Nature*, vol. 559, no. 7715, pp. 547–555, 2018.
- [73] R. Ramakrishnan, P. O. Dral, M. Rupp, and O. A. von Lilienfeld, “Big data meets quantum chemistry approximations: The  $\Delta$ -machine learning approach,” *Journal of chemical theory and computation*, vol. 11, no. 5, pp. 2087–2096, 2015.
- [74] P. Baldi, S. Brunak, and F. Bach, *Bioinformatics: the machine learning approach*. MIT press, 2001.
- [75] S. Ju and J. Shiomi, “Materials informatics for heat transfer: Recent progresses and perspectives,” *Nanoscale and Microscale Thermophysical Engineering*, pp. 1–16, 2019.

- [76] X. Wan, W. Feng, Y. Wang, H. Wang, X. Zhang, C. Deng, and N. Yang, “Materials discovery and properties prediction in thermal transport via materials informatics: A mini review,” *Nano letters*, vol. 19, no. 6, pp. 3387–3395, 2019.
- [77] H. Babaei, R. Guo, A. Hashemi, and S. Lee, “Machine-learning-based interatomic potential for phonon transport in perfect crystalline si and crystalline si with vacancies,” *Physical Review Materials*, vol. 3, no. 7, p. 074 603, 2019.
- [78] J. Behler, “Perspective: Machine learning potentials for atomistic simulations,” *The Journal of chemical physics*, vol. 145, no. 17, p. 170 901, 2016.
- [79] V. L. Deringer, M. A. Caro, and G. Csányi, “Machine learning interatomic potentials as emerging tools for materials science,” *Advanced Materials*, vol. 31, no. 46, p. 1 902 765, 2019.
- [80] N. Artrith and J. Behler, “High-dimensional neural network potentials for metal surfaces: A prototype study for copper,” *Physical Review B*, vol. 85, no. 4, p. 045 439, 2012.
- [81] G. C. Sosso, G. Miceli, S. Caravati, J. Behler, and M. Bernasconi, “Neural network interatomic potential for the phase change material gete,” *Physical Review B*, vol. 85, no. 17, p. 174 103, 2012.
- [82] A. P. Bartók, J. Kermode, N. Bernstein, and G. Csányi, “Machine learning a general-purpose interatomic potential for silicon,” *Physical Review X*, vol. 8, no. 4, p. 041 048, 2018.
- [83] *AlphaGo: The story so far*, <https://deepmind.com/research/case-studies/alphago-the-story-so-far>. [Online]. Available: <https://deepmind.com/research/case-studies/alphago-the-story-so-far>.
- [84] H. Yang, Z. Zhang, J. Zhang, and X. C. Zeng, “Machine learning and artificial neural network prediction of interfacial thermal resistance between graphene and hexagonal boron nitride,” *Nanoscale*, vol. 10, no. 40, pp. 19 092–19 099, 2018.
- [85] H. Wei, S. Zhao, Q. Rong, and H. Bao, “Predicting the effective thermal conductivities of composite materials and porous media by machine learning methods,” *International Journal of Heat and Mass Transfer*, vol. 127, pp. 908–916, 2018.
- [86] H. Wei, H. Bao, and X. Ruan, “Genetic algorithm-driven discovery of unexpected thermal conductivity enhancement by disorder,” *Nano Energy*, vol. 71, p. 104 619, 2020.

- [87] S. Ju, T. Shiga, L. Feng, Z. Hou, K. Tsuda, and J. Shiomi, “Designing nanostructures for phonon transport via bayesian optimization,” *Physical Review X*, vol. 7, no. 2, p. 021 024, 2017.
- [88] M. Yamawaki, M. Ohnishi, S. Ju, and J. Shiomi, “Multifunctional structural design of graphene thermoelectrics by bayesian optimization,” *Science advances*, vol. 4, no. 6, eaar4192, 2018.
- [89] A. Sakurai, K. Yada, T. Simomura, S. Ju, M. Kashiwagi, H. Okada, T. Nagao, K. Tsuda, and J. Shiomi, “Ultrannarrow-band wavelength-selective thermal emission with aperiodic multilayered metamaterials designed by bayesian optimization,” *ACS central science*, vol. 5, no. 2, pp. 319–326, 2019.
- [90] P. Roy Chowdhury, T. Feng, and X. Ruan, “Development of interatomic potentials for the complex binary compound sb2te3 and the prediction of thermal conductivity,” *Phys. Rev. B*, vol. 99, p. 155 202, 15 Apr. 2019. DOI: [10.1103/PhysRevB.99.155202](https://doi.org/10.1103/PhysRevB.99.155202). [Online]. Available: <https://link.aps.org/doi/10.1103/PhysRevB.99.155202>.
- [91] P. Roy Chowdhury, J. Shi, T. Feng, and X. Ruan, “Prediction of bi2te3-sb2te3 interfacial conductance and superlattice thermal conductivity using molecular dynamics simulations,” *ACS Applied Materials & Interfaces*, vol. 13, no. 3, pp. 4636–4642, 2021.
- [92] P. R. Chowdhury and X. Ruan, “An iterative machine learning approach for discovering unexpected thermal conductivity enhancement in aperiodic superlattices,” *arXiv preprint arXiv:2012.08657*, 2020.
- [93] *Nist interatomic potentials repository: Http://www.ctcms.nist.gov/potentials*. [Online]. Available: <http://www.ctcms.nist.gov/potentials>.
- [94] B.-L. Huang and M. Kaviani, “Ab initio,” *Phys. Rev. B*, vol. 77, p. 125 209, 12 Mar. 2008. DOI: [10.1103/PhysRevB.77.125209](https://doi.org/10.1103/PhysRevB.77.125209). [Online]. Available: <https://link.aps.org/doi/10.1103/PhysRevB.77.125209>.
- [95] B. Qiu and X. Ruan, “Molecular dynamics simulations of lattice thermal conductivity of bismuth telluride using two-body interatomic potentials,” *Phys. Rev. B*, vol. 80, p. 165 203, 16 Oct. 2009. DOI: [10.1103/PhysRevB.80.165203](https://doi.org/10.1103/PhysRevB.80.165203). [Online]. Available: <https://link.aps.org/doi/10.1103/PhysRevB.80.165203>.
- [96] X. Tang, W. Xie, H. Li, W. Zhao, Q. Zhang, and M. Niino, “Preparation and thermoelectric transport properties of high-performance p-type bi2te3 with layered nanostructure,” *Applied Physics Letters*, vol. 90, no. 1, p. 012 102, 2007. DOI: [10.1063/1.2425007](https://doi.org/10.1063/1.2425007). eprint: <https://doi.org/10.1063/1.2425007>. [Online]. Available: <https://doi.org/10.1063/1.2425007>.

- [97] B. Poudel, Q. Hao, Y. Ma, Y. Lan, A. Minnich, B. Yu, X. Yan, D. Wang, A. Muto, D. Vashaee, X. Chen, J. Liu, M. S. Dresselhaus, G. Chen, and Z. Ren, “High-thermoelectric performance of nanostructured bismuth antimony telluride bulk alloys,” *Science*, vol. 320, no. 5876, pp. 634–638, 2008, ISSN: 0036-8075. DOI: [10.1126/science.1156446](https://doi.org/10.1126/science.1156446). eprint: <http://science.sciencemag.org/content/320/5876/634.full.pdf>. [Online]. Available: <http://science.sciencemag.org/content/320/5876/634>.
- [98] Y. Q. Cao, X. B. Zhao, T. J. Zhu, X. B. Zhang, and J. P. Tu, “Syntheses and thermoelectric properties of  $\text{Bi}_2\text{Te}_3/\text{Sb}_2\text{Te}_3$  bulk nanocomposites with laminated nanostructure,” *Applied Physics Letters*, vol. 92, no. 14, p. 143 106, 2008. DOI: [10.1063/1.2900960](https://doi.org/10.1063/1.2900960). eprint: <https://doi.org/10.1063/1.2900960>. [Online]. Available: <https://doi.org/10.1063/1.2900960>.
- [99] J. Zhou, C. Jin, J. H. Seol, X. Li, and L. Shi, “Thermoelectric properties of individual electrodeposited bismuth telluride nanowires,” *Applied Physics Letters*, vol. 87, no. 13, p. 133 109, 2005. DOI: [10.1063/1.2058217](https://doi.org/10.1063/1.2058217). eprint: <https://doi.org/10.1063/1.2058217>. [Online]. Available: <https://doi.org/10.1063/1.2058217>.
- [100] A. Mavrokefalos, A. L. Moore, M. T. Pettes, L. Shi, W. Wang, and X. Li, “Thermoelectric and structural characterizations of individual electrodeposited bismuth telluride nanowires,” *Journal of Applied Physics*, vol. 105, no. 10, p. 104 318, 2009. DOI: [10.1063/1.3133145](https://doi.org/10.1063/1.3133145). eprint: <https://doi.org/10.1063/1.3133145>. [Online]. Available: <https://doi.org/10.1063/1.3133145>.
- [101] H. Fang, T. Feng, H. Yang, X. Ruan, and Y. Wu, “Synthesis and thermoelectric properties of compositional-modulated lead telluride–bismuth telluride nanowire heterostructures,” *Nano Letters*, vol. 13, no. 5, pp. 2058–2063, 2013, PMID: 23586462. DOI: [10.1021/nl400319u](https://doi.org/10.1021/nl400319u). eprint: <http://dx.doi.org/10.1021/nl400319u>. [Online]. Available: <http://dx.doi.org/10.1021/nl400319u>.
- [102] L. Li, S. Xu, and G. Li, “Enhancement of thermoelectric properties in  $\text{Bi-Sb-Te}$  alloy nanowires by pulsed electrodeposition,” *Energy Technology*, vol. 3, no. 8, pp. 825–829, 2015, ISSN: 2194-4296. DOI: [10.1002/ente.201500071](https://doi.org/10.1002/ente.201500071). [Online]. Available: <http://dx.doi.org/10.1002/ente.201500071>.
- [103] M. B. Khedim, L. Cagnon, V. Serradeil, T. Fournier, and D. Bourgault, “Thermoelectric nanowires based on bismuth telluride,” *Materials Today: Proceedings*, vol. 2, no. 2, pp. 602–609, 2015, 12th European Conference on Thermoelectrics, ISSN: 2214-7853. DOI: <https://doi.org/10.1016/j.matpr.2015.05.082>. [Online]. Available: <http://www.sciencedirect.com/science/article/pii/S2214785315001534>.

- [104] I. Ng, K. Kok, C. C. A. Rahman, T. Choo, and N. Saidin, “Bismuth telluride based nanowires for thermoelectric power generation,” *Materials Today: Proceedings*, vol. 3, no. 2, pp. 533–537, 2016, Advances in Functional Materials (Conference 2015), ISSN: 2214-7853. DOI: <https://doi.org/10.1016/j.matpr.2016.01.086>. [Online]. Available: <http://www.sciencedirect.com/science/article/pii/S2214785316000870>.
- [105] Y. Tong, F. Yi, L. Liu, P. Zhai, and Q. Zhang, “Molecular dynamics study on thermo-mechanical properties of bismuth telluride bulk,” *Computational Materials Science*, vol. 48, no. 2, pp. 343–348, 2010, ISSN: 0927-0256. DOI: <https://doi.org/10.1016/j.commatsci.2010.01.019>. [Online]. Available: <http://www.sciencedirect.com/science/article/pii/S0927025610000376>.
- [106] C. Shao and H. Bao, “Thermal transport in bismuth telluride quintuple layer: Mode-resolved phonon properties and substrate effects,” *Scientific Reports*, vol. 6, 27492 EP-, Jun. 2016, Article. [Online]. Available: <http://dx.doi.org/10.1038/srep27492>.
- [107] Y. Tong, F. Yi, L. Liu, P. Zhai, and Q. Zhang, “Molecular dynamics study of mechanical properties of bismuth telluride nanofilm,” *Physica B: Condensed Matter*, vol. 405, no. 15, pp. 3190–3194, 2010, ISSN: 0921-4526. DOI: <https://doi.org/10.1016/j.physb.2010.04.038>. [Online]. Available: <http://www.sciencedirect.com/science/article/pii/S092145261000400X>.
- [108] B. Qiu and X. Ruan, “Thermal conductivity prediction and analysis of few-quintuple bi<sub>2</sub>te<sub>3</sub> thin films: A molecular dynamics study,” *Applied Physics Letters*, vol. 97, no. 18, p. 183 107, 2010. DOI: [10.1063/1.3514252](https://doi.org/10.1063/1.3514252). eprint: <https://doi.org/10.1063/1.3514252>. [Online]. Available: <https://doi.org/10.1063/1.3514252>.
- [109] J. Zhang, H. J. Liu, L. Cheng, J. Wei, J. Shi, X. F. Tang, and C. Uher, “Enhanced thermoelectric performance of a quintuple layer of bi<sub>2</sub>te<sub>3</sub>,” *Journal of Applied Physics*, vol. 116, no. 2, p. 023 706, 2014. DOI: [10.1063/1.4889921](https://doi.org/10.1063/1.4889921). eprint: <https://doi.org/10.1063/1.4889921>. [Online]. Available: <https://doi.org/10.1063/1.4889921>.
- [110] Y. Tong, F. J. Yi, L. S. Liu, and Q. J. Zhang, “Molecular dynamics simulation of mechanical properties of single-crystal bismuth telluride nanowire,” *Journal of Electronic Materials*, vol. 39, no. 9, pp. 1730–1734, Sep. 2010, ISSN: 1543-186X. DOI: [10.1007/s11664-010-1204-6](https://doi.org/10.1007/s11664-010-1204-6). [Online]. Available: <https://doi.org/10.1007/s11664-010-1204-6>.
- [111] B. Qiu, L. Sun, and X. Ruan, “Lattice thermal conductivity reduction in bi<sub>2</sub>te<sub>3</sub> quantum wires with smooth and rough surfaces: A molecular dynamics study,” *Phys. Rev. B*, vol. 83, p. 035 312, 3 Jan. 2011. DOI: [10.1103/PhysRevB.83.035312](https://doi.org/10.1103/PhysRevB.83.035312). [Online]. Available: <https://link.aps.org/doi/10.1103/PhysRevB.83.035312>.



- [112] N. A. Katcho, N. Mingo, and D. A. Broido, “Lattice thermal conductivity of  $(\text{bi}1 - x\text{sb}x)_2\text{te}3$  alloys with embedded nanoparticles,” *Phys. Rev. B*, vol. 85, p. 115 208, 11 Mar. 2012. DOI: [10.1103/PhysRevB.85.115208](https://doi.org/10.1103/PhysRevB.85.115208). [Online]. Available: <https://link.aps.org/doi/10.1103/PhysRevB.85.115208>.
- [113] A. Rohskopf, H. R. Seyf, K. Gordiz, T. Tadano, and A. Henry, “Empirical interatomic potentials optimized for phonon properties,” *npj Computational Materials*, vol. 3, no. 1, p. 27, 2017, ISSN: 2057-3960. DOI: [10.1038/s41524-017-0026-y](https://doi.org/10.1038/s41524-017-0026-y). [Online]. Available: <https://doi.org/10.1038/s41524-017-0026-y>.
- [114] T. L. Anderson and H. B. Krause, “Refinement of the  $\text{Sb}_2\text{Te}_3$  and  $\text{Sb}_2\text{Te}_2\text{Se}$  structures and their relationship to nonstoichiometric  $\text{Sb}_2\text{Te}_{3-y}\text{Se}_y$  compounds,” *Acta Crystallographica Section B*, vol. 30, no. 5, pp. 1307–1310, May 1974. DOI: [10.1107/S0567740874004729](https://doi.org/10.1107/S0567740874004729). [Online]. Available: <https://doi.org/10.1107/S0567740874004729>.
- [115] S. Grimme, “Semiempirical gga-type density functional constructed with a long-range dispersion correction,” *Journal of Computational Chemistry*, vol. 27, no. 15, pp. 1787–1799, 2006, ISSN: 1096-987X. DOI: [10.1002/jcc.20495](https://doi.org/10.1002/jcc.20495). [Online]. Available: <http://dx.doi.org/10.1002/jcc.20495>.
- [116] R. P. Stoffel, V. L. Deringer, R. E. Simon, R. P. Hermann, and R. Dronskowski, “A density-functional study on the electronic and vibrational properties of layered antimony telluride,” *Journal of Physics: Condensed Matter*, vol. 27, no. 8, p. 085 402, 2015. [Online]. Available: <http://stacks.iop.org/0953-8984/27/i=8/a=085402>.
- [117] K. Zhao, Y. Wang, Y. Sui, C. Xin, X. Wang, Y. Wang, Z. Liu, and B. Li, “First principles study of isostructural phase transition in  $\text{sb}_2\text{te}_3$  under high pressure,” *physica status solidi (RRL)–Rapid Research Letters*, vol. 9, no. 6, pp. 379–383, 2015.
- [118] R. P. Stoffel, V. L. Deringer, R. E. Simon, R. P. Hermann, and R. Dronskowski, “A density-functional study on the electronic and vibrational properties of layered antimony telluride,” *Journal of Physics: Condensed Matter*, vol. 27, no. 8, p. 085 402, 2015.
- [119] T. Thonhauser, T. J. Scheidemantel, J. O. Sofo, J. V. Badding, and G. D. Mahan, “Thermoelectric properties of  $\text{sb}_2\text{te}_3$  under pressure and uniaxial stress,” *Phys. Rev. B*, vol. 68, p. 085 201, 8 Aug. 2003. DOI: [10.1103/PhysRevB.68.085201](https://doi.org/10.1103/PhysRevB.68.085201). [Online]. Available: <https://link.aps.org/doi/10.1103/PhysRevB.68.085201>.
- [120] A. Togo and I. Tanaka, “First principles phonon calculations in materials science,” *Scripta Materialia*, vol. 108, pp. 1–5, 2015, ISSN: 1359-6462. DOI: <https://doi.org/10.1016/j.scriptamat.2015.07.021>. [Online]. Available: <http://www.sciencedirect.com/science/article/pii/S1359646215003127>.

- [121] V. Chis, I. Y. Sklyadneva, K. A. Kokh, V. A. Volodin, O. E. Tereshchenko, and E. V. Chulkov, “Vibrations in binary and ternary topological insulators: First-principles calculations and raman spectroscopy measurements,” *Phys. Rev. B*, vol. 86, p. 174 304, 17 Nov. 2012. DOI: [10.1103/PhysRevB.86.174304](https://doi.org/10.1103/PhysRevB.86.174304). [Online]. Available: <https://link.aps.org/doi/10.1103/PhysRevB.86.174304>.
- [122] H. Rauh, R. Geick, H. Kohler, N. Nucker, and N. Lehner, “Generalized phonon density of states of the layer compounds  $\text{Bi}_2\text{Se}_3$ ,  $\text{Bi}_2\text{Te}_3$ ,  $\text{Sb}_2\text{Te}_3$  and  $\text{Bi}_2(\text{Te}_{0.5}\text{Se}_{0.5})_3$ ,  $(\text{Bi}_{0.5}\text{Sb}_{0.5})_2\text{Te}_3$ ,” *Journal of Physics C: Solid State Physics*, vol. 14, no. 20, p. 2705, 1981. [Online]. Available: <http://stacks.iop.org/0022-3719/14/i=20/a=009>.
- [123] O. Madelung, U. Rössler, and M. Schulz, Eds., *Antimony telluride ( $\text{Sb}_2\text{Te}_3$ ) phonon dispersion, phonon frequencies: Datasheet from landolt-börnstein - group iii condensed matter · volume 41c: “non-tetrahedrally bonded elements and binary compounds i” in springer materials* ([http://dx.doi.org/10.1007/10681727\\_1054](http://dx.doi.org/10.1007/10681727_1054)), accessed 2018-01-31. DOI: [10.1007/10681727\\_1054](https://doi.org/10.1007/10681727_1054). [Online]. Available: [http://materials.springer.com/lb/docs/sm\\_lbs\\_978-3-540-31360-1\\_1054](http://materials.springer.com/lb/docs/sm_lbs_978-3-540-31360-1_1054).
- [124] T. Tadano, Y. Gohda, and S. Tsuneyuki, “Anharmonic force constants extracted from first-principles molecular dynamics: Applications to heat transfer simulations,” *Journal of Physics: Condensed Matter*, vol. 26, no. 22, p. 225 402, 2014. [Online]. Available: <http://stacks.iop.org/0953-8984/26/i=22/a=225402>.
- [125] J. D. Gale, “Gulp: A computer program for the symmetry-adapted simulation of solids,” *J. Chem. Soc., Faraday Trans.*, vol. 93, pp. 629–637, 4 1997. DOI: [10.1039/A606455H](https://doi.org/10.1039/A606455H). [Online]. Available: <http://dx.doi.org/10.1039/A606455H>.
- [126] Q. Lu, H.-Y. Zhang, Y. Cheng, X.-R. Chen, and G.-F. Ji, “Phase transition, elastic and electronic properties of topological insulator  $\text{Sb}_2\text{Te}_3$  under pressure: First principle study,” *Chinese Physics B*, vol. 25, no. 2, p. 026 401, 2016. [Online]. Available: <http://stacks.iop.org/1674-1056/25/i=2/a=026401>.
- [127] H. Koc, A. M. Mamedov, and E. Ozbay, “Structural, elastic, and electronic properties of topological insulators:  $\text{Sb}_2\text{Te}_3$  and  $\text{Bi}_2\text{Te}_3$ ,” in *2013 Joint IEEE International Symposium on Applications of Ferroelectric and Workshop on Piezoresponse Force Microscopy (ISAF/PFM)*, Jul. 2013, pp. 41–44. DOI: [10.1109/ISAF.2013.6748739](https://doi.org/10.1109/ISAF.2013.6748739).
- [128] R. Kubo, M. Toda, and N. Hashitsume, *Statistical physics II: nonequilibrium statistical mechanics*. Springer Science & Business Media, 2012, vol. 31.



- [129] Z. Wang, S. Safarkhani, G. Lin, and X. Ruan, "Uncertainty quantification of thermal conductivities from equilibrium molecular dynamics simulations," *International Journal of Heat and Mass Transfer*, vol. 112, pp. 267–278, 2017, ISSN: 0017-9310. DOI: <https://doi.org/10.1016/j.ijheatmasstransfer.2017.04.077>. [Online]. Available: <http://www.sciencedirect.com/science/article/pii/S0017931016341643>.
- [130] L. E. Shelimova, O. G. Karpinskii, P. P. Konstantinov, M. A. Kretova, E. S. Avilov, and V. S. Zemskov, "Composition and properties of layered compounds in the  $\text{GeTe-Sb}_2\text{Te}_3$  system," *Inorganic Materials*, vol. 37, no. 4, pp. 342–348, Apr. 2001, ISSN: 1608-3172. DOI: [10.1023/A:1017519625907](https://doi.org/10.1023/A:1017519625907). [Online]. Available: <https://doi.org/10.1023/A:1017519625907>.
- [131] D. M. Rowe, *CRC handbook of thermoelectrics*. CRC press, 1995.
- [132] W.-Y. Lee, N.-W. Park, S.-G. Yoon, and S.-K. Lee, "Analysis of thermal conductivity of antimony telluride thin films by modified callaway and sondheimer models," *Journal of Nanoscience and Nanotechnology*, vol. 16, no. 7, pp. 7567–7572, 2016, ISSN: 1533-4880. DOI: [doi:10.1166/jnn.2016.11118](https://doi.org/10.1166/jnn.2016.11118). [Online]. Available: <http://www.ingentaconnect.com/content/asp/jnn/2016/00000016/00000007/art00135>.
- [133] D. Campi, L. Paulatto, G. Fugallo, F. Mauri, and M. Bernasconi, "First-principles calculation of lattice thermal conductivity in crystalline phase change materials:  $\text{GeTe}$ ,  $\text{Sb}_2\text{Te}_3$ , and  $\text{GeSb}_2\text{Te}_5$ ," *Phys. Rev. B*, vol. 95, p. 024311, 2 Jan. 2017. DOI: [10.1103/PhysRevB.95.024311](https://doi.org/10.1103/PhysRevB.95.024311). [Online]. Available: <https://link.aps.org/doi/10.1103/PhysRevB.95.024311>.
- [134] T. Harman, B. Paris, S. Miller, and H. Goering, "Preparation and some physical properties of  $\text{Bi}_2\text{Te}_3$ ,  $\text{Sb}_2\text{Te}_3$ , and  $\text{As}_2\text{Te}_3$ ," *Journal of Physics and Chemistry of Solids*, vol. 2, no. 3, pp. 181–190, 1957, ISSN: 0022-3697. DOI: [https://doi.org/10.1016/0022-3697\(57\)90081-1](https://doi.org/10.1016/0022-3697(57)90081-1). [Online]. Available: <http://www.sciencedirect.com/science/article/pii/0022369757900811>.
- [135] C. H. Champness, P. T. Chiang, and P. Parekh, "Thermoelectric properties of  $\text{Bi}_2\text{Te}_3$ – $\text{Sb}_2\text{Te}_3$  alloys," *Canadian Journal of Physics*, vol. 43, no. 4, pp. 653–669, 1965. DOI: [10.1139/p65-060](https://doi.org/10.1139/p65-060). eprint: <https://doi.org/10.1139/p65-060>. [Online]. Available: <https://doi.org/10.1139/p65-060>.
- [136] Y. Touloukian, R. Powell, C. Ho, P. Klemens, THERMOPHYSICAL, and E. P. I. A. C. L. IN., *Thermophysical Properties of Matter - The TPRC Data Series. Volume 1. Thermal Conductivity - Metallic Elements and Alloys*. Defense Technical Information Center, 1970. [Online]. Available: <https://books.google.com/books?id=shc0OAAACAAJ>.

- [137] K. Yokota and S. Katayama, “Thermal conductivities of  $(\text{Bi}_{1-x}\text{Sb}_x)_2\text{Te}_3$  and  $\text{Bi}_2(\text{Te}_{1-y}\text{Se}_y)_3$  compounds,” *Japanese Journal of Applied Physics*, vol. 12, no. 8, p. 1205, 1973. [Online]. Available: <http://stacks.iop.org/1347-4065/12/i=8/a=1205>.
- [138] R. Lan, R. Endo, M. Kuwahara, Y. Kobayashi, and M. Susa, “Thermal conductivity measurements of solid  $\text{Sb}_2\text{Te}_3$  by hot-strip method,” *Japanese Journal of Applied Physics*, vol. 49, no. 7R, p. 078 003, 2010. [Online]. Available: <http://stacks.iop.org/1347-4065/49/i=7R/a=078003>.
- [139] T. Feng and X. Ruan, “Quantum mechanical prediction of four-phonon scattering rates and reduced thermal conductivity of solids,” *Phys. Rev. B*, vol. 93, p. 045 202, 4 Jan. 2016. DOI: [10.1103/PhysRevB.93.045202](https://doi.org/10.1103/PhysRevB.93.045202). [Online]. Available: <https://link.aps.org/doi/10.1103/PhysRevB.93.045202>.
- [140] T. Feng, L. Lindsay, and X. Ruan, “Four-phonon scattering significantly reduces intrinsic thermal conductivity of solids,” *Phys. Rev. B*, vol. 96, p. 161 201, 16 Oct. 2017. DOI: [10.1103/PhysRevB.96.161201](https://doi.org/10.1103/PhysRevB.96.161201). [Online]. Available: <https://link.aps.org/doi/10.1103/PhysRevB.96.161201>.
- [141] T. Feng and X. Ruan, “Four-phonon scattering reduces intrinsic thermal conductivity of graphene and the contributions from flexural phonons,” *Phys. Rev. B*, vol. 97, p. 045 202, 4 Jan. 2018. DOI: [10.1103/PhysRevB.97.045202](https://doi.org/10.1103/PhysRevB.97.045202). [Online]. Available: <https://link.aps.org/doi/10.1103/PhysRevB.97.045202>.
- [142] Y. Wang, X. Xu, and R. Venkatasubramanian, “Reduction in coherent phonon lifetime in  $\text{Bi}_2\text{Te}_3/\text{Sb}_2\text{Te}_3$  superlattices,” *Applied Physics Letters*, vol. 93, no. 11, p. 113 114, 2008. DOI: [10.1063/1.2987518](https://doi.org/10.1063/1.2987518). eprint: <https://doi.org/10.1063/1.2987518>. [Online]. Available: <https://doi.org/10.1063/1.2987518>.
- [143] Y. Wang, B. Qiu, A. J. McGaughey, X. Ruan, and X. Xu, “Mode-wise thermal conductivity of bismuth telluride,” *Journal of Heat Transfer*, vol. 135, no. 9, p. 091 102, 2013.
- [144] R. Venkatasubramanian, E. Siivola, T. Colpitts, and B. O’quinn, “Thin-film thermoelectric devices with high room-temperature figures of merit,” *Nature*, vol. 413, no. 6856, p. 597, 2001.
- [145] X. Tang, W. Xie, H. Li, W. Zhao, Q. Zhang, and M. Niino, “Preparation and thermoelectric transport properties of high-performance p-type  $\text{Bi}_2\text{Te}_3$  with layered nanostructure,” *Applied physics letters*, vol. 90, no. 1, p. 012 102, 2007.
- [146] Y. Cao, X. Zhao, T. Zhu, X. Zhang, and J. Tu, “Syntheses and thermoelectric properties of  $\text{Bi}_2\text{Te}_3/\text{Sb}_2\text{Te}_3$  bulk nanocomposites with laminated nanostructure,” *Applied Physics Letters*, vol. 92, no. 14, p. 143 106, 2008.

- [147] J. Zhou, C. Jin, J. H. Seol, X. Li, and L. Shi, “Thermoelectric properties of individual electrodeposited bismuth telluride nanowires,” *Applied Physics Letters*, vol. 87, no. 13, p. 133 109, 2005.
- [148] A. Mavrokefalos, A. L. Moore, M. T. Pettes, L. Shi, W. Wang, and X. Li, “Thermoelectric and structural characterizations of individual electrodeposited bismuth telluride nanowires,” *Journal of Applied Physics*, vol. 105, no. 10, p. 104 318, 2009.
- [149] H. Fang, T. Feng, H. Yang, X. Ruan, and Y. Wu, “Synthesis and thermoelectric properties of compositional-modulated lead telluride–bismuth telluride nanowire heterostructures,” *Nano letters*, vol. 13, no. 5, pp. 2058–2063, 2013.
- [150] L. Li, S. Xu, and G. Li, “Enhancement of thermoelectric properties in bi–sb–te alloy nanowires by pulsed electrodeposition,” *Energy Technology*, vol. 3, no. 8, pp. 825–829, 2015.
- [151] M. B. Khedim, L. Cagnon, V. Serradeil, T. Fournier, and D. Bourgault, “Thermoelectric nanowires based on bismuth telluride,” *Materials Today: Proceedings*, vol. 2, no. 2, pp. 602–609, 2015.
- [152] I. Ng, K. Kok, C. C. A. Rahman, T. Choo, and N. Saidin, “Bismuth telluride based nanowires for thermoelectric power generation,” *Materials Today: Proceedings*, vol. 3, no. 2, pp. 533–537, 2016.
- [153] N. F. Hinsche, B. Y. Yavorsky, M. Gradhand, M. Czerner, M. Winkler, J. König, H. Böttner, I. Mertig, and P. Zahn, “Thermoelectric transport in bi<sub>2</sub>te<sub>3</sub>/sb<sub>2</sub>te<sub>3</sub> superlattices,” *Phys. Rev. B*, vol. 86, p. 085 323, 8 Aug. 2012. DOI: [10.1103/PhysRevB.86.085323](https://link.aps.org/doi/10.1103/PhysRevB.86.085323). [Online]. Available: <https://link.aps.org/doi/10.1103/PhysRevB.86.085323>.
- [154] H. Böttner, G. Chen, and R. Venkatasubramanian, “Aspects of thin-film superlattice thermoelectric materials, devices, and applications,” *MRS bulletin*, vol. 31, no. 3, pp. 211–217, 2006.
- [155] I. Chowdhury, R. Prasher, K. Lofgreen, G. Chrysler, S. Narasimhan, R. Mahajan, D. Koester, R. Alley, and R. Venkatasubramanian, “On-chip cooling by superlattice-based thin-film thermoelectrics,” *Nature nanotechnology*, vol. 4, no. 4, p. 235, 2009.
- [156] S. Ju, T. Shiga, L. Feng, Z. Hou, K. Tsuda, and J. Shiomi, “Designing nanostructures for phonon transport via bayesian optimization,” *Phys. Rev. X*, vol. 7, p. 021 024, 2 May 2017. DOI: [10.1103/PhysRevX.7.021024](https://link.aps.org/doi/10.1103/PhysRevX.7.021024). [Online]. Available: <https://link.aps.org/doi/10.1103/PhysRevX.7.021024>.

- [157] A. Seko, A. Togo, H. Hayashi, K. Tsuda, L. Chaput, and I. Tanaka, “Prediction of low-thermal-conductivity compounds with first-principles anharmonic lattice-dynamics calculations and bayesian optimization,” *Phys. Rev. Lett.*, vol. 115, p. 205 901, 20 Nov. 2015. DOI: [10.1103/PhysRevLett.115.205901](https://doi.org/10.1103/PhysRevLett.115.205901). [Online]. Available: <https://link.aps.org/doi/10.1103/PhysRevLett.115.205901>.
- [158] H. Zhang and A. J. Minnich, “The best nanoparticle size distribution for minimum thermal conductivity,” *Scientific reports*, vol. 5, p. 8995, 2015.
- [159] A. Pattamatta and C. K. Madnia, “Modeling heat transfer in bi2te3–sb2te3 nanostructures,” *International Journal of Heat and Mass Transfer*, vol. 52, no. 3-4, pp. 860–869, 2009.
- [160] Y. Wang and X. Xu, “Mode-wise phonon properties of bismuth telluride,” in *ASME 2012 International Mechanical Engineering Congress and Exposition*, American Society of Mechanical Engineers Digital Collection, 2012, pp. 2965–2969.
- [161] B. Qiu and X. Ruan, “Thermal conductivity prediction and analysis of few-quintuple bi 2 te 3 thin films: A molecular dynamics study,” *Applied Physics Letters*, vol. 97, no. 18, p. 183 107, 2010.
- [162] C. Shao and H. Bao, “Thermal transport in bismuth telluride quintuple layer: Mode-resolved phonon properties and substrate effects,” *Scientific reports*, vol. 6, p. 27 492, 2016.
- [163] J. Zhang, H. Liu, L. Cheng, J. Wei, J. Shi, X. Tang, and C. Uher, “Enhanced thermoelectric performance of a quintuple layer of bi2te3,” *Journal of Applied Physics*, vol. 116, no. 2, p. 023 706, 2014.
- [164] P. W. Lange, “Ein vergleich zwischen bi2te3 und bi2te2s,” *Naturwissenschaften*, vol. 27, no. 8, pp. 133–134, Feb. 1939, ISSN: 1432-1904. DOI: [10.1007/BF01490284](https://doi.org/10.1007/BF01490284). [Online]. Available: <https://doi.org/10.1007/BF01490284>.
- [165] T. L. Anderson and H. B. Krause, “Refinement of the sb2te3 and sb2te2se structures and their relationship to nonstoichiometric sb2te3- ysey compounds,” *Acta Crystallographica Section B: Structural Crystallography and Crystal Chemistry*, vol. 30, no. 5, pp. 1307–1310, 1974.
- [166] S. Plimpton, “Fast parallel algorithms for short-range molecular dynamics,” *Journal of computational physics*, vol. 117, no. 1, pp. 1–19, 1995.

- [167] J. D. Gale and A. L. Rohl, “The general utility lattice program (gulp),” *Molecular Simulation*, vol. 29, no. 5, pp. 291–341, 2003. DOI: [10.1080/0892702031000104887](https://doi.org/10.1080/0892702031000104887). eprint: <https://doi.org/10.1080/0892702031000104887>. [Online]. Available: <https://doi.org/10.1080/0892702031000104887>.
- [168] T. Feng, W. Yao, Z. Wang, J. Shi, C. Li, B. Cao, and X. Ruan, “Spectral analysis of nonequilibrium molecular dynamics: Spectral phonon temperature and local nonequilibrium in thin films and across interfaces,” *Phys. Rev. B*, vol. 95, p. 195 202, 19 May 2017. DOI: [10.1103/PhysRevB.95.195202](https://doi.org/10.1103/PhysRevB.95.195202). [Online]. Available: <https://link.aps.org/doi/10.1103/PhysRevB.95.195202>.
- [169] J. Shi, X. Yang, T. S. Fisher, and X. Ruan, *Dramatic increase in the thermal boundary conductance and radiation limit from a nonequilibrium landauer approach*, 2018. arXiv: [1812.07910](https://arxiv.org/abs/1812.07910) [[cond-mat.mes-hall](https://arxiv.org/archive/cond-mat)].
- [170] P. K. Schelling, S. R. Phillpot, and P. Keblinski, “Comparison of atomic-level simulation methods for computing thermal conductivity,” *Phys. Rev. B*, vol. 65, p. 144 306, 14 Apr. 2002. DOI: [10.1103/PhysRevB.65.144306](https://doi.org/10.1103/PhysRevB.65.144306). [Online]. Available: <https://link.aps.org/doi/10.1103/PhysRevB.65.144306>.
- [171] B. Saha, Y. R. Koh, J. Comparan, S. Sadasivam, J. L. Schroeder, M. Garbrecht, A. Mohammed, J. Birch, T. Fisher, A. Shakouri, and T. D. Sands, “Cross-plane thermal conductivity of (ti,w)n/(al,sc)n metal/semiconductor superlattices,” *Phys. Rev. B*, vol. 93, p. 045 311, 4 Jan. 2016. DOI: [10.1103/PhysRevB.93.045311](https://doi.org/10.1103/PhysRevB.93.045311). [Online]. Available: <https://link.aps.org/doi/10.1103/PhysRevB.93.045311>.
- [172] J. C. Caylor, K. Coonley, J. Stuart, T. Colpitts, and R. Venkatasubramanian, “Enhanced thermoelectric performance in pbte-based superlattice structures from reduction of lattice thermal conductivity,” *Applied Physics Letters*, vol. 87, no. 2, p. 023 105, 2005. DOI: [10.1063/1.1992662](https://doi.org/10.1063/1.1992662). eprint: <https://doi.org/10.1063/1.1992662>. [Online]. Available: <https://doi.org/10.1063/1.1992662>.
- [173] Y. Chen, D. Li, J. R. Lukes, Z. Ni, and M. Chen, “Minimum superlattice thermal conductivity from molecular dynamics,” *Phys. Rev. B*, vol. 72, p. 174 302, 17 Nov. 2005. DOI: [10.1103/PhysRevB.72.174302](https://doi.org/10.1103/PhysRevB.72.174302). [Online]. Available: <https://link.aps.org/doi/10.1103/PhysRevB.72.174302>.
- [174] A. L. Moore and L. Shi, “Emerging challenges and materials for thermal management of electronics,” *Materials today*, vol. 17, no. 4, pp. 163–174, 2014.
- [175] P. Goli, S. Legedza, A. Dhar, R. Salgado, J. Renteria, and A. A. Balandin, “Graphene-enhanced hybrid phase change materials for thermal management of li-ion batteries,” *Journal of Power Sources*, vol. 248, pp. 37–43, 2014.

- [176] R. Prasher, “Thermal interface materials: Historical perspective, status, and future directions,” *Proceedings of the IEEE*, vol. 94, no. 8, pp. 1571–1586, Aug. 2006, ISSN: 0018-9219. DOI: [10.1109/JPROC.2006.879796](https://doi.org/10.1109/JPROC.2006.879796).
- [177] K. M. Shahil and A. A. Balandin, “Graphene–multilayer graphene nanocomposites as highly efficient thermal interface materials,” *Nano letters*, vol. 12, no. 2, pp. 861–867, 2012.
- [178] D. Clarke and C. Levi, “Materials design for the next generation thermal barrier coatings,” *Annual review of materials research*, vol. 33, no. 1, pp. 383–417, 2003.
- [179] D. R. Clarke and S. R. Phillpot, “Thermal barrier coating materials,” *Materials today*, vol. 8, no. 6, pp. 22–29, 2005.
- [180] T. Feng and X. Ruan, “Prediction of spectral phonon mean free path and thermal conductivity with applications to thermoelectrics and thermal management: A review,” *Journal of Nanomaterials*, vol. 2014, 2014.
- [181] L. Lindsay, D. A. Broido, and T. L. Reinecke, “Phonon-isotope scattering and thermal conductivity in materials with a large isotope effect: A first-principles study,” *Phys. Rev. B*, vol. 88, p. 144 306, 14 Oct. 2013. DOI: [10.1103/PhysRevB.88.144306](https://doi.org/10.1103/PhysRevB.88.144306). [Online]. Available: <https://link.aps.org/doi/10.1103/PhysRevB.88.144306>.
- [182] J. Hu, S. Schiffl, A. Vallabhaneni, X. Ruan, and Y. P. Chen, “Tuning the thermal conductivity of graphene nanoribbons by edge passivation and isotope engineering: A molecular dynamics study,” *Applied Physics Letters*, vol. 97, no. 13, p. 133 107, 2010.
- [183] N. Burger, A. Laachachi, M. Ferriol, M. Lutz, V. Toniazzo, and D. Ruch, “Review of thermal conductivity in composites: Mechanisms, parameters and theory,” *Progress in Polymer Science*, vol. 61, pp. 1–28, 2016.
- [184] T. Feng, X. Ruan, Z. Ye, and B. Cao, “Spectral phonon mean free path and thermal conductivity accumulation in defected graphene: The effects of defect type and concentration,” *Physical Review B*, vol. 91, no. 22, p. 224 301, 2015.
- [185] B. Qiu, G. Chen, and Z. Tian, “Effects of aperiodicity and roughness on coherent heat conduction in superlattices,” *Nanoscale and Microscale Thermophysical Engineering*, vol. 19, no. 4, pp. 272–278, 2015.
- [186] R. Frieling, S. Eon, D. Wolf, and H. Bracht, “Molecular dynamics simulations of thermal transport in isotopically modulated semiconductor nanostructures,” *physica status solidi (a)*, vol. 213, no. 3, pp. 549–556, 2016.



- [187] S. Hu, Z. Zhang, P. Jiang, J. Chen, S. Volz, M. Nomura, and B. Li, “Randomness-induced phonon localization in graphene heat conduction,” *The journal of physical chemistry letters*, vol. 9, no. 14, pp. 3959–3968, 2018.
- [188] T. Juntunen, O. Vänskä, and I. Tittonen, “Anderson localization quenches thermal transport in aperiodic superlattices,” *Phys. Rev. Lett.*, vol. 122, p. 105 901, 10 Mar. 2019. DOI: [10.1103/PhysRevLett.122.105901](https://doi.org/10.1103/PhysRevLett.122.105901). [Online]. Available: <https://link.aps.org/doi/10.1103/PhysRevLett.122.105901>.
- [189] T. M. Dieb, S. Ju, K. Yoshizoe, Z. Hou, J. Shiomi, and K. Tsuda, “Mdts: Automatic complex materials design using monte carlo tree search,” *Science and technology of advanced materials*, vol. 18, no. 1, pp. 498–503, 2017.
- [190] A. R. Oganov and C. W. Glass, “Crystal structure prediction using ab initio evolutionary techniques: Principles and applications,” *The Journal of chemical physics*, vol. 124, no. 24, p. 244 704, 2006.
- [191] T. M. Dieb, Z. Hou, and K. Tsuda, “Structure prediction of boron-doped graphene by machine learning,” *The Journal of chemical physics*, vol. 148, no. 24, p. 241 716, 2018.
- [192] N. P. Jouppi, C. Young, N. Patil, D. Patterson, G. Agrawal, R. Bajwa, S. Bates, S. Bhatia, N. Boden, A. Borchers, *et al.*, “In-datacenter performance analysis of a tensor processing unit,” in *2017 ACM/IEEE 44th Annual International Symposium on Computer Architecture (ISCA)*, IEEE, 2017, pp. 1–12.
- [193] S. Wen, X. Xie, Z. Yan, T. Huang, and Z. Zeng, “General memristor with applications in multilayer neural networks,” *Neural Networks*, vol. 103, pp. 142–149, 2018.
- [194] S. Sen, S. Venkataramani, and A. Raghunathan, “Approximate computing for spiking neural networks,” in *Design, Automation & Test in Europe Conference & Exhibition (DATE), 2017*, IEEE, 2017, pp. 193–198.
- [195] C. Aporntewan and P. Chongstitvatana, “A hardware implementation of the compact genetic algorithm,” in *Proceedings of the 2001 Congress on Evolutionary Computation (IEEE Cat. No. 01TH8546)*, IEEE, vol. 1, 2001, pp. 624–629.
- [196] S. Wakabayashi, T. Koide, K. Hatta, Y. Nakayama, M. Goto, and N. Toshine, “Gaa: A vlsi genetic algorithm accelerator with on-the-fly adaptation of crossover operators,” in *ISCAS’98. Proceedings of the 1998 IEEE International Symposium on Circuits and Systems (Cat. No. 98CH36187)*, IEEE, vol. 2, 1998, pp. 268–271.

- [197] K. Irick, M. DeBole, V. Narayanan, and A. Gayasen, “A hardware efficient support vector machine architecture for fpga,” in *2008 16th International Symposium on Field-Programmable Custom Computing Machines*, IEEE, 2008, pp. 304–305.
- [198] J. Garg, N. Bonini, B. Kozinsky, and N. Marzari, “Role of disorder and anharmonicity in the thermal conductivity of silicon-germanium alloys: A first-principles study,” *Phys. Rev. Lett.*, vol. 106, p. 045 901, 4 Jan. 2011. DOI: [10.1103/PhysRevLett.106.045901](https://doi.org/10.1103/PhysRevLett.106.045901). [Online]. Available: <https://link.aps.org/doi/10.1103/PhysRevLett.106.045901>.
- [199] T. Hori, T. Shiga, and J. Shiomi, “Phonon transport analysis of silicon germanium alloys using molecular dynamics simulations,” *Journal of Applied Physics*, vol. 113, no. 20, p. 203 514, 2013.
- [200] S.-i. Tamura, Y. Tanaka, and H. J. Maris, “Phonon group velocity and thermal conduction in superlattices,” *Phys. Rev. B*, vol. 60, pp. 2627–2630, 4 Jul. 1999. DOI: [10.1103/PhysRevB.60.2627](https://doi.org/10.1103/PhysRevB.60.2627). [Online]. Available: <https://link.aps.org/doi/10.1103/PhysRevB.60.2627>.
- [201] S. Volz, J. Saulnier, G. Chen, and P. Beauchamp, “Computation of thermal conductivity of si/ge superlattices by molecular dynamics techniques,” *Microelectronics Journal*, vol. 31, no. 9-10, pp. 815–819, 2000.
- [202] E. S. Landry and A. J. H. McGaughey, “Effect of interfacial species mixing on phonon transport in semiconductor superlattices,” *Phys. Rev. B*, vol. 79, p. 075 316, 7 Feb. 2009. DOI: [10.1103/PhysRevB.79.075316](https://doi.org/10.1103/PhysRevB.79.075316). [Online]. Available: <https://link.aps.org/doi/10.1103/PhysRevB.79.075316>.
- [203] Y. Chalopin, K. Esfarjani, A. Henry, S. Volz, and G. Chen, “Thermal interface conductance in si/ge superlattices by equilibrium molecular dynamics,” *Phys. Rev. B*, vol. 85, p. 195 302, 19 May 2012. DOI: [10.1103/PhysRevB.85.195302](https://doi.org/10.1103/PhysRevB.85.195302). [Online]. Available: <https://link.aps.org/doi/10.1103/PhysRevB.85.195302>.
- [204] C. Dames and G. Chen, “Theoretical phonon thermal conductivity of si/ge superlattice nanowires,” *Journal of Applied Physics*, vol. 95, no. 2, pp. 682–693, 2004.
- [205] M. Hu, K. P. Giapis, J. V. Goicochea, X. Zhang, and D. Poulikakos, “Significant reduction of thermal conductivity in si/ge core-shell nanowires,” *Nano letters*, vol. 11, no. 2, pp. 618–623, 2010.
- [206] M. Hu and D. Poulikakos, “Si/ge superlattice nanowires with ultralow thermal conductivity,” *Nano letters*, vol. 12, no. 11, pp. 5487–5494, 2012.



- [207] J. Tersoff, “Modeling solid-state chemistry: Interatomic potentials for multicomponent systems,” *Phys. Rev. B*, vol. 39, pp. 5566–5568, 8 Mar. 1989. DOI: [10.1103/PhysRevB.39.5566](https://doi.org/10.1103/PhysRevB.39.5566). [Online]. Available: <https://link.aps.org/doi/10.1103/PhysRevB.39.5566>.
- [208] K. Ermis, A. Erek, and I. Dincer, “Heat transfer analysis of phase change process in a finned-tube thermal energy storage system using artificial neural network,” *International Journal of Heat and Mass Transfer*, vol. 50, no. 15-16, pp. 3163–3175, 2007.
- [209] M. H. Esfe, S. Saedodin, M. Bahiraei, D. Toghraie, O. Mahian, and S. Wongwises, “Thermal conductivity modeling of mgo/eg nanofluids using experimental data and artificial neural network,” *Journal of Thermal Analysis and Calorimetry*, vol. 118, no. 1, pp. 287–294, 2014.
- [210] Q. Rong, H. Wei, X. Huang, and H. Bao, “Predicting the effective thermal conductivity of composites from cross sections images using deep learning methods,” *Composites Science and Technology*, vol. 184, p. 107861, 2019.
- [211] P. Chakraborty, Y. Liu, T. Ma, X. Guo, L. Cao, R. Hu, and Y. Wang, “Quenching thermal transport in aperiodic superlattices: A molecular dynamics and machine learning study,” *ACS Applied Materials & Interfaces*, vol. 12, no. 7, pp. 8795–8804, 2020.
- [212] S.-M. Lee, D. G. Cahill, and R. Venkatasubramanian, “Thermal conductivity of si-ge superlattices,” *Applied physics letters*, vol. 70, no. 22, pp. 2957–2959, 1997.
- [213] M. Simkin and G. Mahan, “Minimum thermal conductivity of superlattices,” *Physical Review Letters*, vol. 84, no. 5, p. 927, 2000.
- [214] G. Chen, “Thermal conductivity and ballistic-phonon transport in the cross-plane direction of superlattices,” *Physical Review B*, vol. 57, no. 23, p. 14958, 1998.
- [215] R. Venkatasubramanian, “Lattice thermal conductivity reduction and phonon localizationlike behavior in superlattice structures,” *Physical Review B*, vol. 61, no. 4, p. 3091, 2000.
- [216] J. Ravichandran, A. K. Yadav, R. Cheaito, P. B. Rossen, A. Soukiassian, S. Suresha, J. C. Duda, B. M. Foley, C.-H. Lee, Y. Zhu, *et al.*, “Crossover from incoherent to coherent phonon scattering in epitaxial oxide superlattices,” *Nature materials*, vol. 13, no. 2, pp. 168–172, 2014.
- [217] S. Plimpton, “Fast parallel algorithms for short-range molecular dynamics,” Sandia National Labs., Albuquerque, NM (United States), Tech. Rep., 1993.

- [218] J. Tersoff, “Modeling solid-state chemistry: Interatomic potentials for multicomponent systems,” *Phys. Rev. B*, vol. 39, pp. 5566–5568, 8 Mar. 1989. DOI: [10.1103/PhysRevB.39.5566](https://doi.org/10.1103/PhysRevB.39.5566). [Online]. Available: <https://link.aps.org/doi/10.1103/PhysRevB.39.5566>.
- [219] J. Tersoff, “Erratum: Modeling solid-state chemistry: Interatomic potentials for multicomponent systems,” *Phys. Rev. B*, vol. 41, pp. 3248–3248, 5 Feb. 1990. DOI: [10.1103/PhysRevB.41.3248.2](https://doi.org/10.1103/PhysRevB.41.3248.2). [Online]. Available: <https://link.aps.org/doi/10.1103/PhysRevB.41.3248.2>.
- [220] A. Krizhevsky, I. Sutskever, and G. E. Hinton, “Imagenet classification with deep convolutional neural networks,” in *Advances in neural information processing systems*, 2012, pp. 1097–1105.
- [221] K. He, X. Zhang, S. Ren, and J. Sun, “Deep residual learning for image recognition,” in *Proceedings of the IEEE conference on computer vision and pattern recognition*, 2016, pp. 770–778.
- [222] Y. Wu, M. Schuster, Z. Chen, Q. V. Le, M. Norouzi, W. Macherey, M. Krikun, Y. Cao, Q. Gao, K. Macherey, *et al.*, “Google’s neural machine translation system: Bridging the gap between human and machine translation,” *arXiv preprint arXiv:1609.08144*, 2016.
- [223] G. Hinton, L. Deng, D. Yu, G. E. Dahl, A.-r. Mohamed, N. Jaitly, A. Senior, V. Vanhoucke, P. Nguyen, T. N. Sainath, *et al.*, “Deep neural networks for acoustic modeling in speech recognition: The shared views of four research groups,” *IEEE Signal processing magazine*, vol. 29, no. 6, pp. 82–97, 2012.
- [224] M. Naumov, D. Mudigere, H.-J. M. Shi, J. Huang, N. Sundaraman, J. Park, X. Wang, U. Gupta, C.-J. Wu, A. G. Azzolini, *et al.*, “Deep learning recommendation model for personalization and recommendation systems,” *arXiv preprint arXiv:1906.00091*, 2019.
- [225] D. P. Kingma and J. Ba, “Adam: A method for stochastic optimization,” *arXiv preprint arXiv:1412.6980*, 2014.
- [226] Z. Tian, K. Esfarjani, and G. Chen, “Enhancing phonon transmission across a si/ge interface by atomic roughness: First-principles study with the green’s function method,” *Phys. Rev. B*, vol. 86, p. 235 304, 23 Dec. 2012. DOI: [10.1103/PhysRevB.86.235304](https://doi.org/10.1103/PhysRevB.86.235304). [Online]. Available: <https://link.aps.org/doi/10.1103/PhysRevB.86.235304>.
- [227] W. Zhang, T. Fisher, and N. Mingo, “Simulation of interfacial phonon transport in si–ge heterostructures using an atomistic green’s function method,” 2007.

- [228] K. Gordiz and A. Henry, “Phonon transport at crystalline si/ge interfaces: The role of interfacial modes of vibration,” *Scientific reports*, vol. 6, no. 1, pp. 1–9, 2016.
- [229] L. Sun and J. Y. Murthy, “Molecular dynamics simulation of phonon scattering at silicon/germanium interfaces,” *Journal of heat transfer*, vol. 132, no. 10, 2010.
- [230] R. Vassen, X. Cao, F. Tietz, D. Basu, and D. Stöver, “Zirconates as new materials for thermal barrier coatings,” *Journal of the American Ceramic Society*, vol. 83, no. 8, pp. 2023–2028, 2000.
- [231] J. R. Nicholls, K. Lawson, A. Johnstone, and D. Rickerby, “Low thermal conductivity eb-pvd thermal barrier coatings,” in *Materials science forum*, Trans Tech Publ, vol. 369, 2001, pp. 595–606.
- [232] J. Wu, X. Wei, N. P. Padture, P. G. Klemens, M. Gell, E. García, P. Miranzo, and M. I. Osendi, “Low-thermal-conductivity rare-earth zirconates for potential thermal-barrier-coating applications,” *Journal of the American Ceramic Society*, vol. 85, no. 12, pp. 3031–3035, 2002.
- [233] D. Zhu, Y. L. Chen, and R. A. Miller, “Defect clustering and nano-phase structure characterization of multi-component rare earth oxide doped zirconia-yttria thermal barrier coatings,” in *Ceram. Eng. Sci. Proc.*, vol. 24, 2003, pp. 525–534.
- [234] J. Wang, Y. Zhou, X. Chong, R. Zhou, and J. Feng, “Microstructure and thermal properties of a promising thermal barrier coating: Ytao4,” *Ceramics International*, vol. 42, no. 12, pp. 13 876–13 881, 2016.
- [235] J. Wang, X. Chong, R. Zhou, and J. Feng, “Microstructure and thermal properties of retao4 (re= nd, eu, gd, dy, er, yb, lu) as promising thermal barrier coating materials,” *Scripta Materialia*, vol. 126, pp. 24–28, 2017.
- [236] J. I. Eldridge, C. M. Spuckler, K. W. Street, and J. R. Markham, “Infrared radiative properties of yttria-stabilized zirconia thermal barrier coatings,” in *26th Annual Conference on Composites, Advanced Ceramics, Materials, and Structures: B: Ceramic Engineering and Science Proceedings*, John Wiley & Sons, Inc, vol. 23, 2002, pp. 417–430.
- [237] D. E. Wolfe, J. Singh, R. A. Miller, J. I. Eldridge, and D.-M. Zhu, “Tailored microstructure of eb-pvd 8ysz thermal barrier coatings with low thermal conductivity and high thermal reflectivity for turbine applications,” *Surface and coatings technology*, vol. 190, no. 1, pp. 132–149, 2005.

- [238] V. Stathopoulos, V. Sadykov, S. Pavlova, Y. Bepalko, Y. Fedorova, L. Bobrova, A. Salanov, A. Ishchenko, V. Stoyanovsky, T. Larina, *et al.*, “Design of functionally graded multilayer thermal barrier coatings for gas turbine application,” *Surface and Coatings Technology*, vol. 295, pp. 20–28, 2016.
- [239] H. Chen, Y. Liu, Y. Gao, S. Tao, and H. Luo, “Design, preparation, and characterization of graded ysz/la2zr2o7 thermal barrier coatings,” *Journal of the American Ceramic Society*, vol. 93, no. 6, pp. 1732–1740, 2010.
- [240] L. Swadźba, G. Moskal, B. Mendala, and M. Hetmańczyk, “Characterization of microstructure and properties of tbc systems with gradient of chemical composition and porosity,” *Archives of Metallurgy and Materials*, vol. 53, no. 3, pp. 945–954, 2008.
- [241] C. Tekmen, I. Ozdemir, and E. Celik, “Failure behaviour of functionally gradient materials under thermal cycling conditions,” *Surface and Coatings Technology*, vol. 174, pp. 1101–1105, 2003.
- [242] M. J. Kelly, D. E. Wolfe, J. Singh, J. Eldridge, D.-M. Zhu, and R. Miller, “Thermal barrier coatings design with increased reflectivity and lower thermal conductivity for high-temperature turbine applications,” *International journal of applied ceramic technology*, vol. 3, no. 2, pp. 81–93, 2006.
- [243] X. Huang, D. Wang, P. Patnaik, and J. Singh, “Design and computational analysis of highly reflective multiple layered thermal barrier coating structure,” *Materials Science and Engineering: A*, vol. 460, pp. 101–110, 2007.
- [244] W. Ge, C. Zhao, and B. Wang, “Thermal radiation and conduction in functionally graded thermal barrier coatings. part i: Experimental study on radiative properties,” *International Journal of Heat and Mass Transfer*, vol. 134, pp. 101–113, 2019.
- [245] J. Guo, S. Ju, and J. Shiomi, “Design of a highly selective radiative cooling structure accelerated by materials informatics,” *Optics Letters*, vol. 45, no. 2, pp. 343–346, 2020.
- [246] D. Chae, M. Kim, P.-H. Jung, S. Son, J. Seo, Y. Liu, B. J. Lee, and H. Lee, “Spectrally selective inorganic-based multilayer emitter for daytime radiative cooling,” *ACS applied materials & interfaces*, vol. 12, no. 7, pp. 8073–8081, 2020.
- [247] Y. Shi, W. Li, A. Raman, and S. Fan, “Optimization of multilayer optical films with a memetic algorithm and mixed integer programming,” *ACS Photonics*, vol. 5, no. 3, pp. 684–691, 2017.
- [248] R. E. Stephens and I. H. Malitson, “Index of refraction of magnesium oxide,” *Journal of Research of the National Bureau of Standards*, vol. 49, no. 4, pp. 249–252, 1952.

- [249] S. Guo, H. Arwin, S. Jacobsen, K. Järrendahl, and U. Helmersson, “A spectroscopic ellipsometry study of cerium dioxide thin films grown on sapphire by rf magnetron sputtering,” *Journal of Applied physics*, vol. 77, no. 10, pp. 5369–5376, 1995.
- [250] P. W. Anderson, “Absence of diffusion in certain random lattices,” *Physical review*, vol. 109, no. 5, p. 1492, 1958.
- [251] A. McGurn, K. Christensen, F. Mueller, and A. Maradudin, “Anderson localization in one-dimensional randomly disordered optical systems that are periodic on average,” *Physical Review B*, vol. 47, no. 20, p. 13 120, 1993.
- [252] M. Sigalas and C. Soukoulis, “Elastic-wave propagation through disordered and/or absorptive layered systems,” *Physical Review B*, vol. 51, no. 5, p. 2780, 1995.
- [253] B. Van Tiggelen, A. Lagendijk, and D. Wiersma, “Reflection and transmission of waves near the localization threshold,” *Physical review letters*, vol. 84, no. 19, p. 4333, 2000.

## VITA

Prabudhya Roy Chowdhury (he/him) was born in Kolkata, West Bengal in India. He received the Bachelor of Technology and Master of Technology degrees from the Indian Institute of Technology, Kharagpur, India in 2016. He joined the Nanoscale Energy Transport and Conversion Laboratory directed by Prof. Xiulin Ruan at the School of Mechanical Engineering and the Birck Nanotechnology Center at Purdue University in 2016. His research involves atomistic simulations and machine learning-enabled prediction of thermal transport. He received the Ross Fellowship in 2016 and the Bilsland Dissertation Fellowship in 2020. He was also recognized with the Outstanding Research Award from the Graduate School and the Kohr Graduate Student Fellowship in memory of Prof. Robert H. Kohr from the School of Mechanical Engineering at Purdue University in 2021. Prabudhya is a Ph.D. candidate expecting to receive his doctoral degree in Mechanical Engineering in August, 2021.